January 2015

A microstructure based fatigue life prediction framework and its validation

Saikumar Reddy Yeratapally
Purdue University

Graduate School Form 30
Updated 1/15/2015

PURDUE UNIVERSITY
GRADUATE SCHOOL
Thesis/Dissertation Acceptance

This is to certify that the thesis/dissertation prepared

By SAIKUMAR REDDY YERATAPALLY

Entitled

A MICROSTRUCTURE BASED LIFE PREDICTION FRAMEWORK AND ITS VALIDATION

For the degree of Doctor of Philosophy

Is approved by the final examining committee:

Michael D. Sangid
Chair

Weinong W. Chen

Michael G. Glavicic

David F. Bahr

To the best of my knowledge and as understood by the student in the Thesis/Dissertation Agreement, Publication Delay, and Certification Disclaimer (Graduate School Form 32), this thesis/dissertation adheres to the provisions of Purdue University's "Policy of Integrity in Research" and the use of copyright material.

Approved by Major Professor(s): Michael D. Sangid

Approved by: Weinong Chen 12/7/2015

Head of the Departmental Graduate Program Date

A MICROSTRUCTURE BASED FATIGUE LIFE PREDICTION FRAMEWORK AND ITS VALIDATION

A Dissertation

Submitted to the Faculty

of

Purdue University

by

Saikumar Reddy Yeratapally

In Partial Fulfillment of the

Requirements for the Degree

of

Doctor of Philosophy

December 2015

Purdue University

West Lafayette, Indiana

To my parents, Usha Reddy Yeratapally and Ramachandra Reddy Yeratapally, whose love and affection made this possible.

ACKNOWLEDGEMENTS

First and foremost, I would like to express my sincere gratitude to my advisor, Dr. Michael D. Sangid. I am ever grateful to him for providing me the opportunity of pursuing a Ph.D. when I was at a very critical juncture in my career. During my Ph.D. he gave me the freedom to explore and work on multiple projects, which challenged me step out of the comfort zone and helped me broaden my research interests. Throughout my Ph.D., he created numerous opportunities for me to directly communicate with several industry experts and well renowned researchers, which helped me in not only learning from them, but also in developing a strong professional network which was very important for me as a young researcher. From the very beginning of my Ph.D., he took keen interest in knowing what my post-Ph.D. ambitions were. He took my career goals seriously and laid out a path for me by creating incredible opportunities and letting me spend two semesters at NASA Langley research center (LaRC), which ultimately led to a post-doc opportunity at NASA LaRC. If not for him looking out for my best interests, all the great opportunities that I have taken advantage of, during the course of my Ph.D., would not have been possible.

I would like to thank Rolls-Royce Corporation (RRC) for the financial assistance provided over the past three and a half years in support of my research endeavor. On several occasions throughout my Ph.D., I have had incredible opportunities to present my

research to industry experts and researchers at RRC, including Dr. Michael G. Glavicic, Dr. Robert Goetz, Dr. Mark Hardy, Dr. Christos Argyrakis, Jeff Stillinger. I would like to thank these incredible people for sparing their valuable time in looking at my research progress and for providing constant feedback, which at times, not only steered me in the right direction, but also gave me a big-picture vision of the role played by my research work in the real world, which was quite motivating. I would like to convey my special regards to Dr. Michael Glavicic, first, for serving on my dissertation committee, and second, for patiently routing numerous documents (including abstracts/ journal manuscripts and conference presentations) through public release process.

Next, I would like to thank Dr. Wayne Chen and Dr. David Bahr for serving on my dissertation committee and for their guidance, support and advice, especially regarding how important it was for a computational research engineer (like myself) to also be able to know and understand experimental methods and techniques. Their advice led me to take a class on transmission electron microscopy, which was undoubtedly one of the best classes I have taken at Purdue.

Through the course of my Ph.D., I was fortunate to have interacted and worked with many successful people who are extremely smart, hardworking. In particular, I would like to acknowledge Dr. Jacob D. Hochhalter of NASA LaRC, who was instrumental in creating an opportunity for me to go work at NASA LaRC on a project which aligned with my interests. I would like to thank him for his hospitality during my stay at NASA, many insightful discussions on the topic of fatigue failure in polycrystalline alloys and for help with digital image correlation experiments. I would

also like to thank other researchers at NASA including Andy, Jim, Pat, Paul, Geoff, Tim with whom I interacted on a daily basis regarding several research and non-research related topics and for making me feel at home throughout my stay at NASA.

I would like to extend my regards to, Al Cerrone, whom I met while he was still a graduate student at Cornell. There are a few people who just want to help others and want others to succeed in life. Al comes under that category of exceptional people who is always willing to lend a helping hand. The numerous research, non-research and other fun, lighthearted skype conversations I had with him over the past three years helped me in my journey as a graduate student. I would like to specifically thank him for sharing his parallelized polycrystal mesher, which was very helpful in my own research work, where I had to convert surface meshes to volume meshes.

I would like to acknowledge Michael Jackson (of BlueQuartz), Michael Groeber (of AFRL), Joe Tucker (of Exponent) for their help with DREAM.3D. Further, I would also like to thank Dr. Anthony Rollett and Dr. Lisa Chan (of CMU) for sharing their twin insertion source code, which was extremely helpful in creating statistically equivalent microstructures in my research work.

I would like to express my gratitude to AAE department for supporting me with teaching assistantship when I was in need of financial assistance. Many thanks to the current and the past lab members of ACME, Javier Esquivel, Matthew Durbin, Andrea Rovinelli, Andrea Nicolas, Ajey, Prithivi, Ronald, Todd, Kartik, Diwakar, Imad, Alberto, Burak, Lena, John, for numerous helpful research discussions, for creating ever cheerful lab environment and lifelong memories. Further, I would like to thank fellow

boilermakers, Waterloo Tsutsui, Amit, Neeraj, Rohan for their great friendship throughout my stay at Purdue.

I would like to thank my little niece Tanvi, and cousin Kaushik for all the fun conversations over the years, which helped me take my mind off of work. I want to thank my parents, Usha and Ramachandra Reddy, for all their sacrifices and for constantly motivating me to aim high and achieve high in life. If not for them, I would not be where I am today.

TABLE OF CONTENTS

Page

Page

Page

Page

LIST OF TABLES

LIST OF FIGURES

Figure Page

Figure Page

Figure Page

Figure Page

ABBREVIATIONS

ALA	as-large-as
APBE	anti-phase boundary energy
CPFE	crystal plasticity finite element
CRSS	critical resolved shear stress
CSL	coincident site lattice
CSM	contribution to sample mean
CSV	contribution to sample variance
CTB	coherent twin boundary
CUSUNORO	cumulative sum of normalized reordered output
DC	degree of crystallinity
EBSD	electron back scatter diffraction
ESA	elastic stress anisotropy
GB	grain boundary
GBE	grain boundary energy
GSA	global sensitivity analysis
GBCD	grain boundary character distribution
HAGB	high angle grain boundary
HCF	high cycle fatigue
LAGB	low angle grain boundary
LCF	low cycle fatigue
LRB	Lee-Robertson-Birnbaum
MD	molecular dynamics

MH	Metropolis Hastings
MCMC	markov chain Monte Carlo
NS	normal stress
PPM	parallelized polycrystal mesher
PSA	plastic strain accumulation
PSB	persistent slip band
QoI	quantity of interest
RSS	resolved shear stress
RVE	representative volume element
SDV	state dependent variable
SEM	statistically equivalent microstructure
SFE	stacking fault energy
TB	twin boundary
VRH	Voigt-Reuss-Hill

SYMBOLS

Latin symbols:

a	lattice parameter
b	magnitude of Burgers vector
e	measurement error
B_p	variance of a parameter (p) between n chains
C_{ij}	cubic elastic constants
C_{ij}^{γ}	cubic elastic constants of γ phase
$C_{ij}^{\gamma'}$	cubic elastic constants of γ' phase
D	collection of observed fatigue life data
E	Young's modulus
$E_{slip-GB}^{\gamma-MD}$	energy required for a dislocation to transmit across a GB
E_{PSB}	energy of a PSB
$E[Y/X_i]$	expectation of the output Y obtained by randomly changing all other parameters expect X_i
f	volume fraction of γ' precipitates
F	deformation gradient
F^e	elastic part of the deformation gradient accounting for stretch and rotation
F^p	plastic part of the deformation gradient accounting for dislocation slip
g^{α}	critical resolved shear stress on slip system α
$\dot{g}^{\alpha}$	rate of increment in critical resolved shear stress on slip system α

h	width of a PSB
H	direct hardening coefficient
k	proportionality constant
L	length of the PSB
L_{avg}	average length of all the PSBs formed within the microstructure
L_p	plastic velocity gradient
m	rate sensitivity exponent
m^{α}	vector denoting normal to slip system α
n	number of markov chains running in parallel
N	number of fatigue cycles
n_{ext-GB}^{dis}	number of dislocations forming an extrusion at intersection of a PSB and GB
n^{layers}	number of slip planes within a PSB
n_{eff}^{layers}	number of effective layers contributing to SFE or APBE
N_{offset}	number of cycles after which extrusions start to form at PSB-GB intersection
p	effective accumulated plastic strain
$\dot{p}$	rate of change of effective accumulated plastic strain
$q^{\alpha\beta}$	hardening coefficient for interaction between slip systems α and β
r	ratio between the posterior densities between the candidate point ($\boldsymbol{\alpha}$*) and the current point ($\boldsymbol{\alpha}$)
R	dynamic recovery coefficient
R_p	markov chain convergence test statistic
s^{α}	Burgers vector of slip system α
S_i	first order Sobol's sensitivity index
S_{ij}	second order Sobol's sensitivity index

S_{ijk}	third order Sobol's sensitivity index
S_{Ti}	total sensitivity index
U_{yy}	displacement field around an edge dislocation
$V(E[Y/X_i])$	variance of the expectations obtained for several values of X_i
$V[Y/X_{\sim i}]$	variance of the data obtained by considering random variations in X_i and by keeping all other parameters fixed
W_p	variance of a parameter (p) within n markov chains
x_i	experimental conditions under which fatigue life data was obtained
$y(x_i)$	fatigue lives obtained from experiments

Greek symbols:

$\boldsymbol{\alpha}$	set of all influential model parameters
∂X_i	incremental slip with in a PSB
$\dot{\gamma}_o$	reference strain rate for all slip systems
$\dot{\gamma}^{\alpha}$	strain rate on slip system α
γ^{α}	accumulated plastic strain on slip system α
γ_{APBE}	anti-phase boundary energy
γ_{SFE}	stacking fault energy
δ	model bias
$\Delta\varepsilon$	applied strain amplitude
$\Delta\tau^{\alpha}_{CPFEM}$	applied cyclic stress on a PSB
$\boldsymbol{\theta}$	set of all model parameters
$\pi_0(\boldsymbol{\alpha})$	prior distributions of set of influential parameters $\boldsymbol{\alpha}$
$\pi(\boldsymbol{\alpha}^*\|\boldsymbol{\alpha})$	proposal (or jump) distribution
$\pi(\boldsymbol{\alpha}\|D)$	posterior distribution of set of influential parameters $\boldsymbol{\alpha}$
$\pi(D)$	marginal density

$\pi(D\|\boldsymbol{\alpha})$	likelihood of observing the data (D) given parameter set $\boldsymbol{\alpha}$
μ	rigidity modulus
Λ	lattice incompatibility tensor
Λ_{eq}	equivalent lattice incompatibility, a measure of elastic stress anisotropy
v	Poisson's ratio
ρ	dislocation density
σ	unknown hyper-parameter
$\sigma_{hardening}$	hardening within a PSB
$\sigma_{pile-up}$	pile-up stress at the PSB-GB intersection
σ_{stroh}	GB resistance in terms of stress
σ_N^α	normal stress acting on a slip system α
σ_{YY}	stress field around an edge dislocation
τ^α	resolved shear stress on a slip system α
χ^α	back stress on a slip system α
$\dot{\chi}^\alpha$	rate of increment in back stress on a slip system α

ABSTRACT

Yeratapally, Saikumar Reddy Ph.D., Purdue University, December 2015. A Micro-structure Based Fatigue Life Prediction Framework and its Validation. Major Professor: Michael D. Sangid.

Fatigue crack initiation in polycrystalline materials can be attributed to various mechanistic and microstructural features acting in concert like the elastic stress anisotropy, plastic strain accumulation, resolved shear stress, normal stress, slip-system length, and grain boundary character. In nickel-base superalloys, fatigue cracks tend to initiate near twin boundaries. The factors causing fatigue crack initiation depend on the material's microstructure, the variability of which results in the scatter observed in the fatigue life. In this work, a robust microstructure based fatigue framework is developed, which takes into account i) the statistical variability of the material's microstructure, ii) the continuum scale complex heterogeneous 3D stress and strain states within the microstructure, and iii) the atomistic mechanisms such as slip-grain boundary (GB) interactions, extrusion formations, and shearing of the matrix and precipitates due to slip. The quantitative information from crystal plasticity simulations and molecular dynamics is applied to define the energy of persistent slip bands (PSB). The energy of a critical PSB and its associated stability with respect to the dislocation motion is used as the failure criterion for crack initiation. This unified framework helps us gain insights on why fatigue cracks tend to initiate at twin boundaries. In addition to that, the computational

framework links variability in material's microstructure to the scatter observed in fatigue life.

The microstructure based fatigue model is used to study the role played by various microstructural attributes (like grain size, γ' volume fraction, GB character) in limiting fatigue life. Additionally, the role played by local microstructural response (plastic strain accumulation, elastic stress anisotropy developed at the GBs, extrusion height at intersection of persistent slip bands and GBs) in triggering crack initiation is also studied. We show that the aforementioned attributes have varying degree of influence over fatigue life, which in turn gives rise to a wide spectrum of opportunities (in the bulk of the material) with varying degree of severity where fatigue cracks can potentially initiate, thereby contributing to the scatter observed in fatigue life.

The fatigue model is validated using an uncertainty quantification and propagation framework. First, global sensitivity analysis (GSA) is used to identify the set of the most influential parameters in the life prediction model. Following GSA, the posterior distributions of all influential model parameters are calculated using a Bayesian inference framework, which is built based on a Markov chain Monte Carlo algorithm. The quantified uncertainties thus obtained, are propagated through the model using Monte Carlo sampling technique to make robust predictions of fatigue life. The model is validated by comparing the predictions to experimental fatigue life data.

1. INTRODUCTION

1.1 Fatigue Failure

Components subjected to cyclic loading undergo failure after a certain number of cycles, irrespective of whether the applied loads are above or below the yield stress of the material. This mode of failure is called fatigue. More than 50% of mechanical failures in aircraft components are due to fatigue [1]. Failure of a critical component on an aircraft in service leads to irrevocable loss of life and property [2,3]. Characterization of scatter in fatigue life at various applied loads, along with rigorous investigation of crack initiation sites is necessary, as the knowledge gained from such studies will help plan replacement of critical components in a timely manner, and improve the design of components and material processing routes, which in turn help reduce occurrence of unexpected catastrophic accidents.

Fatigue failure of a component occurs in three stages : i) fatigue crack initiation ii) propagation of microstructurally small fatigue cracks, iii) coalescence of small cracks to form a big crack which leads to final fracture of component. Major factors that influence fatigue life of a component include i) applied stress/ strain amplitude, ii) mean stress, iii) temperature, iv) residual stresses, v) material process pedigree, vi) microstructure of the material, vii) presence of manufacturing defects, etc. For a given load and temperature, considerable amount of fatigue life is spent in initiation and propagation of

microstructurally small fatigue cracks, during which the material's microstructure has a great role to play. Due to this reason, fatigue scatter observed in components made of polycrystalline materials can be partially attributed to the variability of complex heterogeneities in the microstructure. These heterogeneities are responsible for the complex stress and strain fields developed under load, and govern where cracks could potentially nucleate.

1.2 Classical Ways of Determining Fatigue Life of a Component

One way to fully characterize the scatter in fatigue life of a material is to make many specimens and test them until failure. From both cost and time point of view, it is not feasible to conduct extensive experimental fatigue testing to characterize the fatigue life of a material at different loading conditions and temperatures. This is especially true when there is a need to meet a growing demand for supply of components that are to be deployed in service within a limited amount of time.

"Safe-life" fatigue design strategy assumes that the structure is free from any defects or cracks. It predicts the conservative fatigue life of a component by using the mean fatigue life and by applying a safety factor (typically 4) [3,4]. In materials that exhibit excessive scatter, application of this methodology is not effective as it leads to replacement of parts even if it can still take considerable number of load cycles, thereby proving to be uneconomical. Additionally, nowhere in this methodology, concern is laid over presence of pre-cracks or unexpected damage caused due to material or manufacturing flaws [2], let alone the consideration of complexities of material's microstructure.

Empirically based stress and strain life methods [5-7] have been used for over the past five decades to obtain the number of cycles required for the formation of cracks in high cycles fatigue (HCF) and low cycle fatigue (LCF) regimes. But, they overlook the complex heterogeneities present in the microstructure and any initial flaws that might be present in the material (or component). In addition to that, these empirical models are independent of the deformation mechanism that might be active at a specific load and temperature regime, thus limiting their use. In the recent past, catastrophic component failures (as shown in Fig. 1.1) occurred due to undetected microstructural flaws and intergranular fatigue cracks that grew during the service of the component thereby resulting in the formation of large cracks [8,9]. Hence, it is important to consider the microstructure and (deformation mechanism based) micro-mechanical damage while developing tools and methods to predict scatter in fatigue life.

(a)

(b) (c)

Figure 1.1. Uncontained high pressure turbine disc failure (a) in Boeing 767-223 on June 2, 2006 [8], (b, c) in Boeing 767-219ER on December 8, 2002 [9].

Although there has been substantial work done in using advanced computational tools and experimental techniques to understand the driving forces for fatigue crack initiation, there is still a considerable amount of work that is to be done in calculating fatigue scatter by explicitly taking into consideration, the heterogeneities of a given material's microstructure and the complicated 3D stress and strain states that develop within the bulk of the material. A well calibrated and rigorously validated microstructure and deformation mechanism dependent life prediction model, which can relate the variability of microstructure to scatter in fatigue life, is worthwhile as it helps predict fatigue scatter in a time and cost efficient way.

The current work discusses a computational fatigue life prediction framework which addresses the issue of linking variability in microstructure to scatter in fatigue life. The microstructure based life prediction framework consists of three sub modules: i) a module to create statistically equivalent microstructures (or SEMs) using statistics of microstructural attributes obtained from electron backscatter diffraction (EBSD) scans (obtained for the polycrystalline material of interest), ii) a crystal plasticity finite element

(CPFE) framework which solves for the heterogeneous 3D stress/strain state within the microstructure (along with slip system based stresses and strains) over a one-cycle loading at a strain amplitude, R-ratio and temperature of interest and, iii) a deformation mechanism based life prediction model which not only takes into consideration the physics of an active deformation mechanism (at a certain temperature of interest where the mechanism is active) but also differentiates between various types of grain boundaries (GBs) based on the energetics of their interaction with dislocations, calculated by molecular dynamics (MD) simulations. Additionally, it takes the heterogeneous slip system based stresses and strains (from CPFE simulations) as input.

1.3 Problem Statement

The material of interest in the current study is a polycrystalline nickel-base superalloy, RR1000, developed by Rolls-Royce plc. It is used in making turbine discs for jet engines. Formation of persistent slip bands (PSBs) was observed to be an active deformation mechanism in this material when subjected to fatigue loading at an intermediate elevated temperature. Fractography studies on failed specimens (made of RR1000) revealed crystallographic faceted crack initiation sites (as shown in Fig. 1.2) in the subsurface regions of test specimens [10]. Additionally, it was also observed that crystallographic faceted cracks initiated in close proximity to twin boundaries (TBs) within favorably oriented large grains [11]. Such crystallographic cracks were also observed in various other nickel-base superalloys when subjected to fatigue at elevated temperatures [12-15]. Further, excessive fatigue life scatter was observed in RR1000, when the aforementioned crack initiation mechanism was active. There is still a gap in the fundamental understanding of the competing role played by various microstructural

attributes (especially twins) and local defect level deformation mechanisms in i) initiating fatigue cracks and ii) influencing fatigue scatter. In order to address the aforementioned issues, rigorously validated microstructure and deformation mechanism based computational failure predictive models need to developed, which, not only provide valuable insights on various factors contributing to fatigue crack initiation, but also link the variability in microstructure to the scatter in fatigue life. It must also be kept in mind that none of the computational models represent a 100% reality of what exactly is happening within the material, due to the presence of uncertainties. So the failure predictive models should be verified, validated and well calibrated before they can be used in a production environment. Hence, the research problem at hand is twofold:

i) Address the combined role played by various microstructural attributes and local microstructural response in driving fatigue crack initiation at twin boundaries.

ii) Deterministically link the variability of the microstructure with the scatter in fatigue life, using a rigorously validated microstructure based fatigue framework, which takes into consideration the complex 3D stress states developed within the microstructure and the energetics of slip-GB interaction.

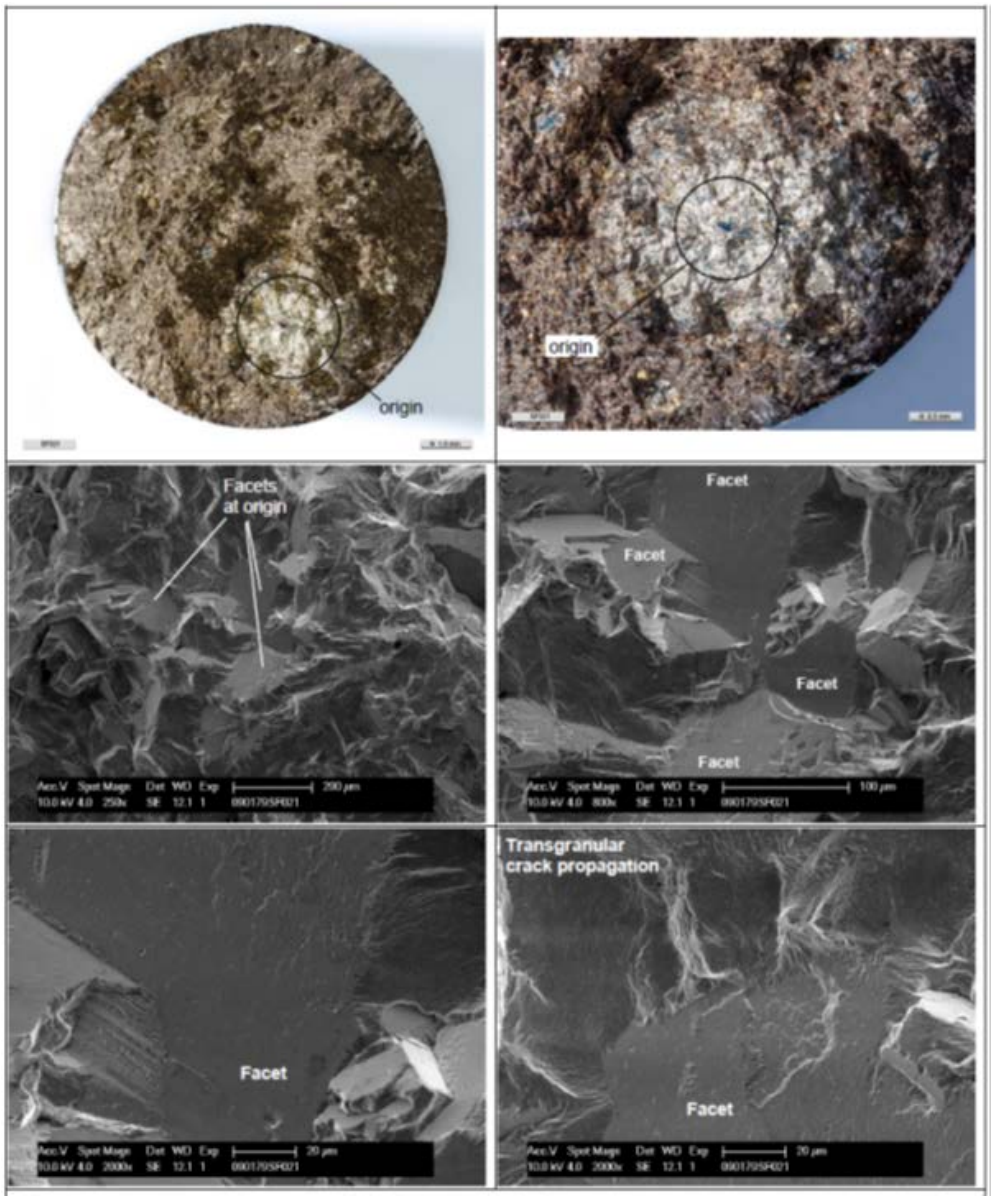

Figure 1.2. Fatigue crack initiation from crystallographic facets, in two different specimens subjected to fatigue at elevated temperatures. Image courtesy of Rolls-Royce plc [10].

1.4 Framework of the Microstructure Based Fatigue Life Prediction Model

The fatigue life prediction framework has three main modules. First, the generation of SEMs, which are representative of the material's microstructure. Is it not

always possible to obtain a high resolution 3D microstructure data of a material due to limited availability of non-destructive high energy X-Ray diffraction resources [16] (and automated serial sectioning based methods [17]). With the availability of advanced microstructure analysis and characterization tools like DREAM.3D [18,19], and with the use of stereology concepts, it is possible to build synthetic 3D microstructures which closely represent the real microstructure of the material. The statistics of morphological and crystallographic heterogeneities are obtained from the 2D EBSD scans. Stereological methods are then applied to get an estimated 3D distribution of grain sizes from the 2D grain size distributions (obtained from EBSD). Surface meshes of grains (in .stl format) in the SEMs are obtained using marching cube technique [20] in DREAM.3D, following which Laplacian smoothing is applied in order to smoothen the GBs. Following this, the SEMs are volume meshed using a parallelized polycrystal mesher (PPM) [21] which outputs an ABAQUS input (.inp) file.

Second, the SEMs generated are subjected to a one-cycle loading in a rate dependent CPFE framework to solve for the heterogeneous 3D stress and strain states throughout the microstructure. The internal state dependent variables (SDVs) (like the resolved shear stress, normal stress, back stress and accumulated strain on slip system etc.,) are used to find the most dominant slip systems in all the grains.

The third component of the framework is a life prediction model. It defines crack initiation based on the stability of a PSB, which is evaluated by calculating the cyclic evolution of PSB energy. PSB energy is calculated by using i) the SDV information obtained from CPFE simulations, ii) GB energetics obtained from MD simulations and

iii) microstructural attributes obtained from the SEMs generated using DREAM.3D. An important feature of the life prediction model is its ability to incorporate the energy contributions of some of the cyclic slip irreversibilities (like the formation of extrusions at the intersection of PSB-GB and evolution of the extrusion height, shearing of the γ' precipitates etc.) that occur during the fatigue process. A high level overview connecting all the three modules of the microstructure and deformation mechanism based life prediction framework is shown in Fig. 1.3. It can be clearly visualized that the framework is clearly able to link the variability in microstructure (simulated by generating many SEMs) to scatter in fatigue life.

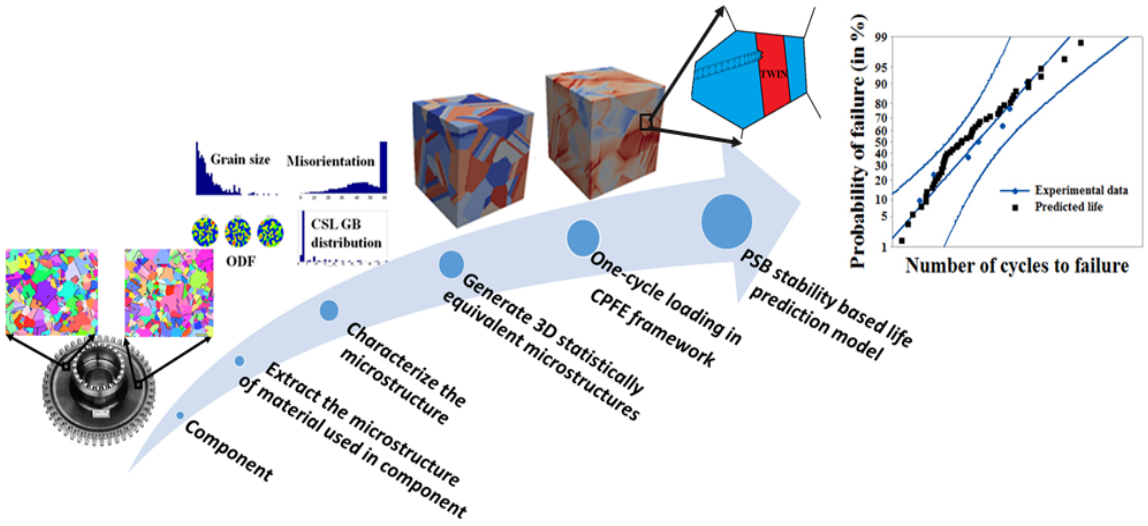

Figure 1.3. A high level overview of the microstructure based fatigue life prediction framework, which is developed to link the variability in microstructure with scatter in fatigue life.

1.5 Uncertainty Quantification and Uncertainty Propagation

Fatigue crack initiation in polycrystalline materials can be attributed to the heterogeneous microstructure forming complex stress states resulting in strain heterogeneities and localization. Additionally, cyclic loading manifests in deformation mechanisms leading to cyclic slip irreversibilities which ultimately increase stress concentration and thereby lead to the formation of cracks. Many empirical [7-9] and physics-based models [22-25] have been proposed to predict fatigue life in polycrystalline materials. Uncertainties exist in all the models, and before such computational models are employed (to predict the life of components), careful attention must be given to understand the degree in which these uncertainties influence the predicted quantity of interest (QoI), the fatigue life. Rigorous uncertainty quantification for validation purposes is a pre-requisite for such predictive models to be used in a production environment. Part of the current research work focuses on identifying, quantifying and propagating the uncertainties in the microstructure based life prediction model used in the current study for the purpose of validating it. In this study, model validation is performed based on:

i) global sensitivity analysis (GSA) to select the set of the most influential parameters in the model which will help reduce the dimensionality and hence the computational cost of the uncertainty quantification problem [26,27].

ii) Bayesian inference to quantify the identified uncertainties in the model [27-29].

iii) Monte-Carlo sampling to propagate the quantified uncertainties to obtain distribution of predicted life, which will be used in validating the model's predictions [27,29].

Figure 1.4 shows a high level overview of the sensitivity and uncertainty analysis conducted to validate the fatigue life prediction model used in this research.

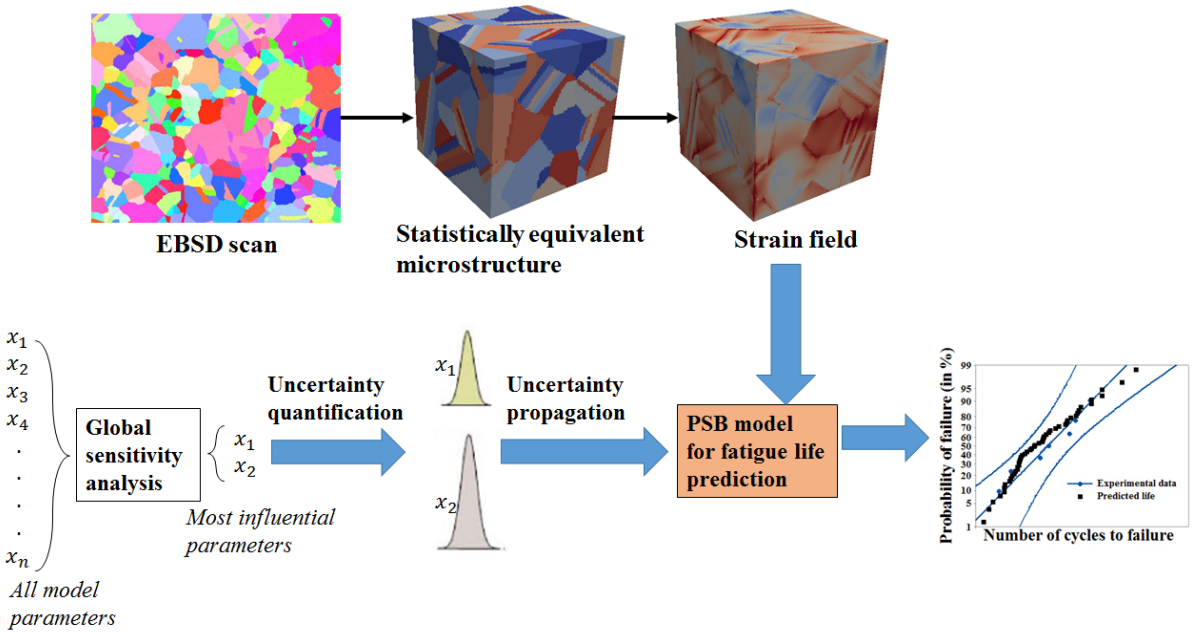

Figure 1.4. A high level overview of the sensitivity and uncertainty analysis if the fatigue model.

1.6 Research Contributions

There are two main contributions of the current research. First, emphasis is laid on understanding why fatigue cracks tend to initiate at twin boundaries, by taking into consideration, the energetics of slip-GB interactions (calculated using MD), and the quantitative information from the complicated stress/strain states developed within the twin (obtained from crystal plasticity simulations). We show that various factors (like elastic anisotropy, accumulated plastic strain, and resolved shear stress) act in concert at a

favorably oriented twin (impinged upon by a PSB) to increase the propensity of crack initiation. In addition to the aforementioned factors, we show that the normal stress acting on a twin plays a significant role in *unzipping* a PSB at the intersection of the TB, thereby acting as a driving force for crack initiation in mode I. We further show that favorably oriented twins embedded in large grains are more prone to crack initiation.

Second, using a well validated microstructure based fatigue life prediction framework we show that the variability of a material's microstructure (simulated by generating multiple SEMs) leads to scatter observed in fatigue life.

1.7 Thesis Outline

This thesis is organized into the following six chapters. A quick road map of the thesis is furnished below.

Chapter 1 highlights the importance of microstructure based fatigue lifing. It gives a high level overview of the life prediction framework used in the current study along with the uncertainty and sensitivity analysis that were done to validate the model.

Chapter 2 presents a review of literature related to i) fatigue crack initiation, ii) the role played by various microstructural attributes and cyclic slip irreversibilites in fatigue crack initiation, iii) state-of-the-art microstructure based life prediction models and iv) uncertainty quantification.

Chapter 3 discusses in detail, the three modules that comprise the microstructure based life prediction model, namely i) an automated framework which takes the statistics of microstructural heterogeneities and builds SEMs which are used to simulate the variability in microstructure of the material, ii) a rate dependent crystal plasticity model

which is used to solve for the heterogeneous stress and strain states within the SEM generated (when subjected to cyclic loading), and iii) a fatigue life prediction model which takes in the data from CPFE simulations, energetics of GB-dislocation interactions from MD simulations and grain sizes within the SEMs (generated by DREAM.3D) to define a criterion for crack initiation based on the stability of a PSB (based on its energy) and calculate number of cycles for crack initiation.

Chapter 4 presents a detailed discussion on i) GSA that was used to identify the set of most influential parameters in the model which also helped to reduce the dimensionality of the uncertainty quantification problem, ii) Bayesian inference based technique implemented to quantify the uncertainties of a set of most influential parameters (identified by GSA), iii) Monte Carlo technique used to propagate the uncertainties through the model to quantify uncertainty in the output.

Chapter 5 discusses how fatigue scatter observed in polycrystalline nickel-base superalloys can be attributed to complex interaction between heterogeneous microstructure of the material and fatigue specific defect level mechanisms. The influential role played by microstructure in fatigue crack initiation is evident from experimental observations. For instance, large grains (or inclusions) are detrimental to fatigue life. Similarly, accumulation of cyclic slip irreversibilities was observed to correlate inversely with fatigue life. A robust microstructure based life prediction model should agree with such common trends observed in nature (or experiments). Various case studies are done to analyze how the current fatigue model agrees with the trends observed in experiments, thereby serving as a sanity check for the model.

Chapter 6 summarizes the current research work and reflects on the significance of the research. Following the conclusions, recommendations for future work are also listed.

2. LITERATURE SURVEY

This chapter presents a literature survey on both experimental and computational work done in gaining fundamental insights on fatigue crack initiation in polycrystalline materials. An overview is provided on the important role played by local microstructural response and various microstructural attributes in driving fatigue crack initiation, thereby reflecting on the importance of explicitly considering active deformation mechanisms and microstructural attributes while developing failure predictive models. A review of the state-of-the-art microstructure based fatigue life prediction models is provided. Emphasis is laid on the need for uncertainty quantification and propagation in order to validate life prediction models.

2.1 Cyclic Strain Localization and Slip Irreversibilities in Fatigue

Over the past century, following Ewing and Humfrey's [30] discovery of the cyclic slip localization (which gradually resulted in formation of cracks) on the flat surface of polycrystalline Swedish iron specimens, a great amount of research effort has been dedicated towards understanding microstructural mechanisms that drive fatigue crack initiation. The advent of advanced electron microscopy techniques has helped in obtaining excellent details pertaining to the dislocation networks and sub-structures, which are considered as prerequisite for fatigue crack initiation in FCC metals and alloys.

2.1.1 Formation of Persistent Slip Bands

During fatigue loading, dislocations multiply and accumulate within the material resulting in an increased value of the dislocation density. These dislocations arrange themselves in the low energy configurations by forming clusters of dipoles called veins [31-33]. Veins primarily comprise of edge dislocation dipoles due to annihilation of screw dislocations by cross slip. With repetitive cyclic loading the (dipolar and/or multipolar) vein structure disintegrates and rearranges itself by adjusting the distance between the edge dislocation dipoles, until the least possible distance between dipoles is achieved [33]. At this stage, the vein structure can no longer accommodate any additional dislocations generated (due to additional plastic strain), and hence transforms into dislocation walls. Several lamellae of dislocation walls in a local domain combine to form a ladder-like structure (PSB). Neumann [33], using numerical techniques showed that the dislocation dipole wall structures are far more stable than the equiaxed vein structures. The ladder-like structure of PSBs (as shown in Fig. 2.1a, b, c) was evident in various single, polycrystalline metals [34-37] and alloys [38] as well. In precipitation hardened materials, like nickel-base superalloys, PSBs form as dislocations cut through the γ matrix and γ' precipitates in a planar slip manner (as shown in Fig. 2.1b) [39-44]. Further, PSBs in superalloys are thinner with strain localization at least an order higher compared to those in metals [45]. The topic of PSB formation in polycrystalline metals and alloys has been discussed extensively in some excellent literature surveys [46-48].

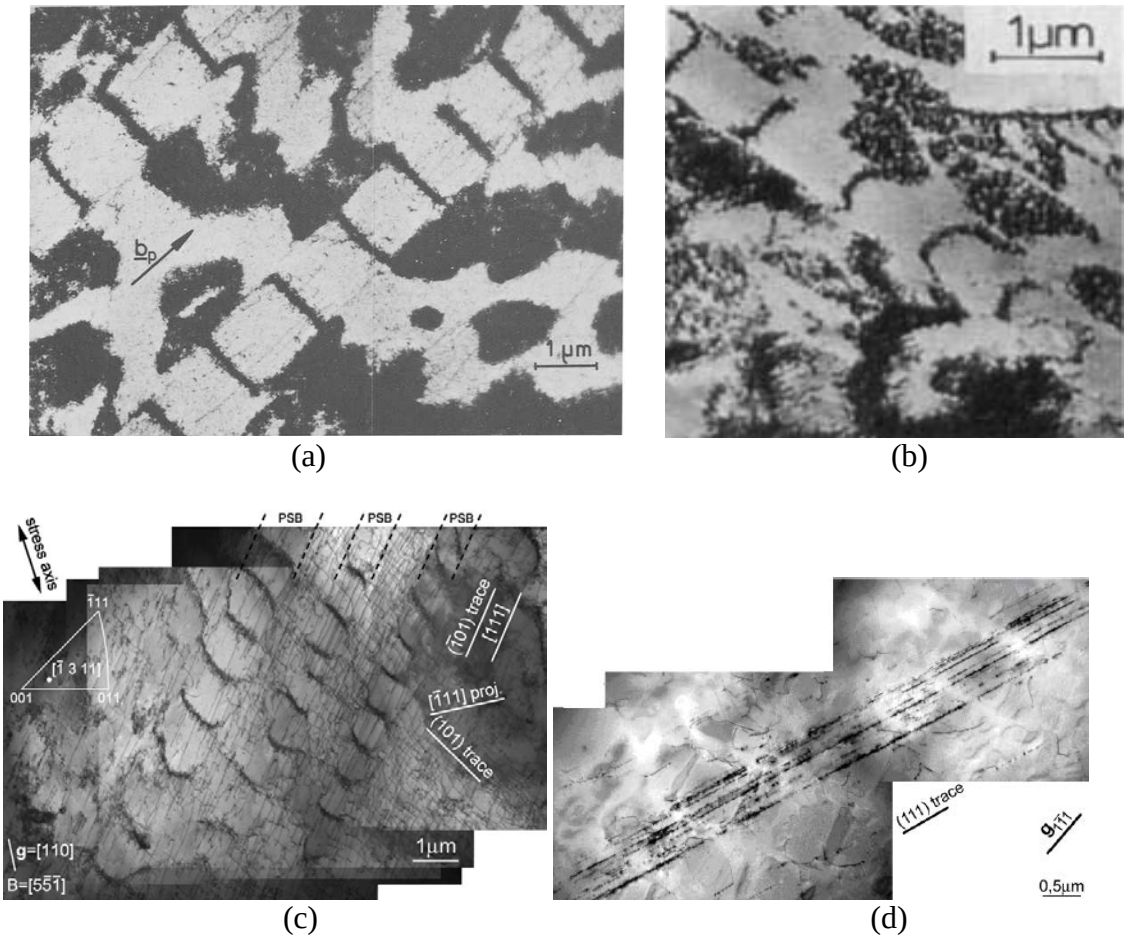

Figure 2.1. PSB formed in a) copper single crystal [34], (b) polycrystalline copper [37], (c) polycrystalline ferritic steel [38], (d) polycrystalline nickel-base superalloy, IN 792-5A [44].

2.1.2 Cyclic Slip Irreversibilities and their Correlation with Fatigue Life

Damage precursors to fatigue failure are governed by forward and reverse loading that is not fully recoverable, leading to permanent deformation, known as cyclic slip irreversibilities. For instance, cross slip of screw dislocations, mutual annihilation of (screw/edge) dislocations, dislocation climb, formation of locks, kinks, shearing of precipitates, etc., result in an unequal effective dislocation glide during forward and reverse cyclic loading. Further, extrusions and intrusions, are type of cyclic slip

irreversibilities that are formed when PSBs intersect with surface [49,50] or high angle grain boundaries (HAGBs) [51,52] (as shown in Fig. 2.2). The PSB-HAGB interaction results in an increased stress concentration at the PSB-GB interface due to the formation of dislocation pile-ups, and extrusions at the GBs, which ultimately leading to the formation of microcracks [53,54], as shown in Fig. 2.3. Experimental studies [50,55] quantified the dependence of the extrusion heights (and heights of slip steps formed on the surface) on the applied macroscopic strain and it was observed that extrusion height scales with the applied strain amplitude.

Accumulation of cyclic slip irreversibilities within the bulk of the material and/or on the surface result in initiation of microcracks and hence affect fatigue life. Mughrabi [56,57] showed that fatigue life correlated inversely with the amount of accumulated cyclic slip irreversibilities. Mughrabi [57,58] related cyclic slip irreversibilities to fatigue lives empirically, by replacing the plastic strain amplitude in the Coffin-Mason's law, with quantifiable cyclic slip irreversibility. Risbet et al. [40,59] observed that in a nickel-base superalloy, Waspaloy, cracks formed when the local irreversible plastic strain (accumulated in slip bands) reached a critical value. Additionally, local cyclic slip irreversibilities were in turn influenced by the microstructural attributes, like grain size and precipitate size [40]. In polycrystalline 316L steel, the mean extrusion height at the surface was observed to be proportional to the size of the grain below the surface, which contained the slip band [60].

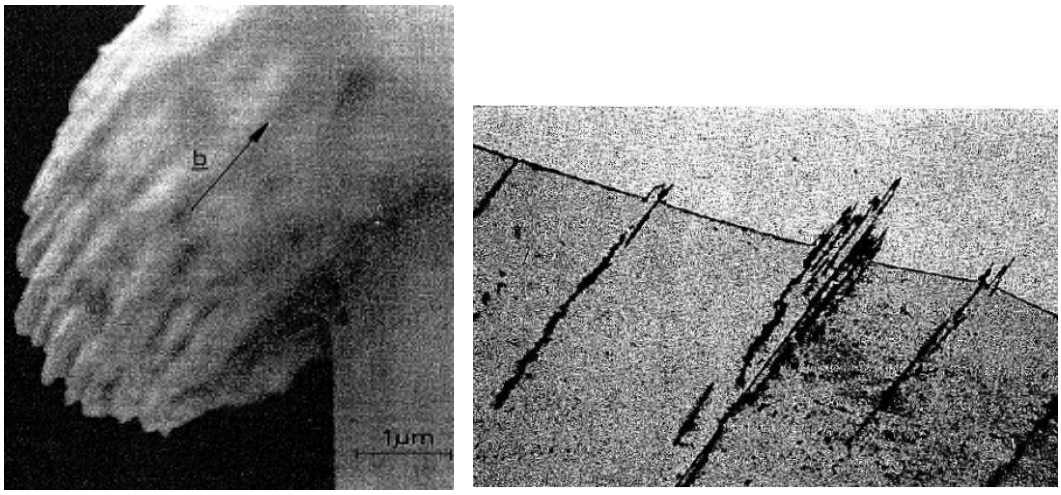

(a) (b)

Figure 2.2. (a) Formation of extrusions in copper due to the impingement of PSB on surface [35,36], (b) Formation of static extrusions in the vicinity of a TB [51].

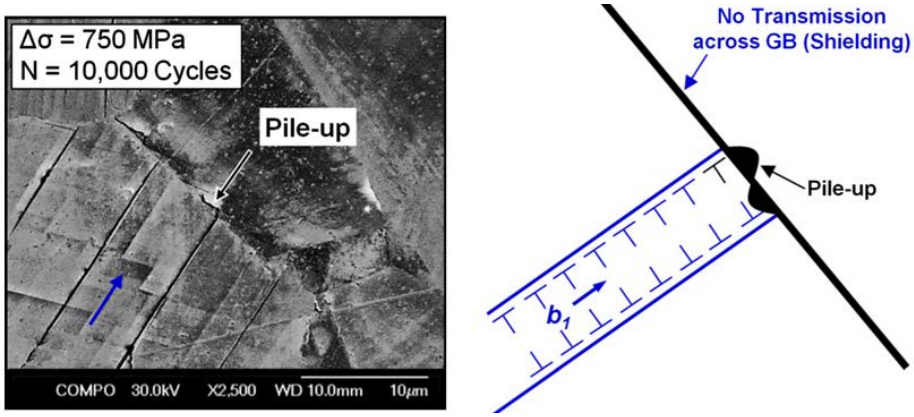

Figure 2.3. Dislocation pile-up at a GB resulting in the formation of a microcrack in Hastealloy X [54].

The experimental observations pertaining to the structure of the PSB and its interaction with GBs, coupled with the dependence of cyclic slip irreversibilities on microstructural attributes (for instance the dependence of extrusion height on grain size) are taken into consideration while formulating the energy of a PSB, whose stability will be used to define crack initiation in the fatigue framework discussed in the current study.

2.2 Role of Microstructural Attributes in Fatigue Crack Initiation

Microstructure of polycrystalline materials plays a significant role in fatigue crack initiation and can be partially attributed to the fatigue scatter observed in the components. The propensity for the formation of fatigue cracks was observed to correlate well with certain microstructural attributes, over a wide range of materials. Fatigue life was observed to correlate inversely with grain size, for various polycrystalline metals [61] and alloys [62-66], with a uniform grain size. Further, it has been shown that fatigue life is limited to the size of ALA (as-large-as) grains [67] or supergrains (grain clusters with large grains connected by low angle grain boundaries or LAGBs) [68-70]. Thompson et al. [61] compared the fatigue lives of materials with different stacking fault energies (which quantifies the ease of cross slip to occur) and concluded that strong inverse correlation exists between fatigue life and grain size in materials with low stacking fault energies where cross slip is difficult to occur. Further, it was observed that PSBs, which are precursors to fatigue crack initiation, were more prone to form in favorably oriented large grains [66,70-78]. In addition to grain size, the GB character was also observed to influence the ease with which fatigue cracks initiate.

Microcracks were observed to nucleate at TBs in certain FCC polycrystalline metals [51,54,79,80] and alloys, specifically in nickel-base superalloys (as shown in Fig. 2.4) [11,69,74,75,79-82,105]. In nickel-base superalloys, the propensity of fatigue cracks to initiate at a TB correlated with the length of the TB [69,82], and the resolved shear stress acting on the slip plane parallel to the TB [82]. Over the past three decades, substantial amount of research work was done to gain insights on why fatigue cracks tent to initiate at TBs. Wang et al. used a finite element model on a bi-crystal with a TB and

found that stress and slip enhancement is greatest in a small volume of material near the surface and close to the TB [83]. Peralta et al. calculated the compatibility stresses at TBs and varied the orientation of the loading axis to the TB [84]. They observed that the stress concentration at the TB is a maximum when tensile load is applied along a <111> direction. Neumann derived an analytical expression for the tractions at the intersection of a TB and a surface, and further emphasized that the observed slip activity and the crack initiation on planes parallel to the TB plane is not due to the compatibility stresses, but due to the logarithmic singular surface tractions that occur at the intersection of the surface with the TB [85]. In addition to simple bicrystal based models, which teach us about activity in the local neighborhood of a TB, high fidelity models that take into account heterogeneous deformation of twins and energetics of twin-slip interactions have also been developed.

(a) (b)

Figure 2.4. EBSD scans showing fatigue crack initiation in the vicinity of TBs (indicated by arrows), in nickel-base superalloys (a) RENE 88DT [74], and (b) LSHR [104].

Sangid et al. using MD simulations, showed that coherent TB offers the lowest interface energy and highest barrier to dislocation nucleation and transmission, thus providing a significant strengthening contribution [86]. Further, Sangid et al. developed a

microstructure-based model to predict fatigue crack nucleation in a nickel-base superalloy, U720, consisting of a high density of coherent TBs [23,24,69]. Their model, which takes into account GB energetics and the interaction of PSBs with GBs, predicted that most often cracks nucleated at TBs in U720, which was also observed in experiments [69]. By calculating a fatigue indicator parameter in a crystal plasticity framework, Castelluccio and McDowell showed that large annealing twins are more detrimental than thinner deformation twins and stressed their importance [87]. Further, Cerrone et al. used gradient crystal plasticity in a finite element model of an experimentally measured 3D microstructure wherein a microcrack nucleated along a coherent TB in a nickel-base superalloy, LSHR [88]. From the crystal plasticity simulations, they hypothesized that high elastic anisotropy and coplanarity of the boundary plane with a {111} slip plane were responsible for the accumulation of slip and subsequently for the microcrack nucleation event at the TB. Each of the aforementioned analytical and computational models provide valuable insights into the role played by TBs on fatigue crack initiation in polycrystalline materials. But understanding why fatigue cracks initiate at twins from a lengthscale point of view is still lacking. The fatigue framework presented in the current study takes into account, the energetics of slip-twin interaction (calculated using MD simulations), and the quantitative information from the complicated stress/strain states developed within the twin (obtained from crystal plasticity simulations) and uses this information in a PSB energy based failure prediction framework. One of the main focuses of the current study (which explicitly considers TBs in the microstructure) is to understand the effect of elastic anisotropy, plastic strain accumulation and normal stress on crack initiation at twins.

Fatigue crack initiation is a microstructure and deformation mechanism based phenomenon and a robust fatigue prediction model should consider contributions from various length scales. Although there has been substantial and important work done using crystal plasticity based models and MD simulations, the present work develops a framework, which unifies length scales (by considering both atomistic and continuum level contributions) with explicit consideration of microstructures, which are statistically equivalent to the real microstructure of the material. Such a high fidelity model helps us gain more insight into the most critical factors that contribute to crack nucleation and also link microstructure variability to scatter observed in fatigue life. This framework takes quantitative information of the heterogeneous deformation from crystal plasticity simulations pertaining to microstructure descriptions of 3D stresses and strains, energetics of slip-GB interaction, stacking fault and anti-phase boundary energies from atomistic calculations, to predict where cracks could potentially nucleate. Further, this framework explicitly includes twins in statistically equivalent microstructures (SEMs) that are built on the morphological and crystallographic statistics obtained from the real material's microstructure data. The present work also delivers insights on the evolution of elastic anisotropy and plastic strain accumulation at the GBs.

2.3 State-of-the-Art Microstructure Based Life Prediction Models

Experimental observations of deformation mechanisms leading to fatigue crack initiation coupled with correlations established between various microstructural attributes, cyclic slip irreversibilities and fatigue life, have assisted in the development of failure predictive models. Over the past three decades, various micro-mechanical fatigue

crack initiation models have been developed that consider the energy of dislocation structure within the PSB [22,23,24,69,89-92]. Tanaka, Mura et al. [22] in their model define crack initiation at a point when the total energy of the PSB equals the specific fracture energy of the material. Later in the 1990s their model was revisited [90,91] to calculate the evolution of Gibbs free energy with fatigue cycles and the revised model defines crack initiation at a point where the Gibbs energy hits a maximum value and starts to fall rapidly due to instabilities within the dislocation structure of the PSB. Sangid et al. [23,24,69] defined the energy of a PSB within a polycrystalline nickel-base superalloy using energy contributions from atomistic and continuum length scales, and defined crack initiation criteria at a point when the PSB reaches a minimum energy configuration where it would rather allow a crack to nucleate than becoming unstable. The aforementioned models do not account for a 3D complex stress state evolving within each grain within the polycrystal, e.g. the previous models use Schmid factors to calculate resolved shear stress on a slip system, and hence ignore the elastic anisotropy, normal stress acting on the PSB, hardening, and the affect due to the incompatible stresses that are introduced by the neighboring grains. This is not a way forward, at least for LCF crack initiation models. The fatigue model presented in the current study uses a modified version of the PSB energy expression developed by Sangid et al. [23,24,69] for a nickel-base superalloy, U720. It must be noted that some degree of uncertainties exist in all models, and in order to build trustworthiness in these models it is important to quantify the uncertainties that exist in them, using well established uncertainty analysis techniques.

2.4 Uncertainty Quantification and Propagation Techniques

Researchers in various sub-disciplines of computational material science and engineering including computational solid (and particle) mechanics [29,92], computational fluid dynamics [93], MD [94,95], etc., have integrated uncertainty analysis into their modeling framework. Over the past decade, uncertainty quantification has been successfully applied to fatigue crack growth models pertaining to both metals [96-99] and composites [100,101]. Zhang and Mahadevan [96] used Bayesian inference technique to quantify uncertainties via statistical distribution parameters in two competing crack growth models for metals. Cross et al. [98] used a hierarchical Bayesian inference framework to quantify uncertainties in equivalent initial flaw size and crack growth rate parameters, and hence improved the predictive capabilities of their fatigue crack growth model. Chiachio et al. [101] used a full Bayesian approach to quantify uncertainties of a set of five damage mechanics models for composites and the best of the models was chosen based on an information-theoretic approach by calculating the relative probability amongst all other candidate models. The metal fatigue crack growth models discussed above are empirical in nature and are independent of the microstructure of the material, which has a great influence in crack initiation [22-24,69,90,91] and microstructurally small fatigue crack growth [102]. The fatigue life prediction framework which is used in the current study [25], differs from the above mentioned crack growth models in the following three ways. First, it is a microstructure based framework, where the morphological and crystallographic heterogeneities in the microstructure are considered and an attempt is made to link the variability of the microstructure with the fatigue life calculated. Second, it is not fully empirical in nature, as the model takes into

consideration the physics of underpinning deformation mechanisms, which lead to cyclic slip irreversibilities during fatigue. Finally, the model predicts number of cycles for crack initiation rather than calculating crack growth with number of cycles. While dealing with models that predict fatigue crack initiation, a phenomenon, which is dependent on both the local microstructure and deformation mechanisms, the number of epistemic uncertainties increases due to the complexities involving lengthscale dependent deformation mechanisms. These uncertainties need to be quantified, in order to validate the model and identify an appropriate applicability regime. There is a great amount of work that needs to be done in quantifying uncertainties in complex physics based models and hence improving the predictive capabilities of such models.

As discussed earlier, several micro-mechanical fatigue crack initiation models have been developed which take into consideration the heterogeneities within the microstructure and various parameters that quantify lengthscale dependent deformation mechanisms [22-25,69,89-91]. The energy based model of Tanaka and Mura [22] takes into consideration parameters like the frictional stress, cyclic slip irreversibility and the specific fracture energy of the material. The fatigue crack initiation framework developed by Sangid et al. [23,24,69] takes into consideration, width of a PSB, dislocation density, γ' volume fraction, grain boundary (GB) energies, extrusion height at intersection of PSB-GB, stacking fault and anti-phase boundary energies. There are uncertainties associated with all the parameters mentioned above, some of which are difficult to measure using experiments. Although these models provide great insights into understanding how certain microstructural features and competing deformation mechanisms lead to initiation of fatigue cracks, systematic uncertainty analysis, in an

attempt to rigorously validate such physics-based models, is still lacking [103]. The current work fills this gap by using an uncertainty quantification and propagation framework, in order to validate a microstructure and deformation mechanism based life prediction model [25].

This study presents a full Bayesian inference, which uses Markov chain Monte Carlo (MCMC) algorithms to sample from the posterior distributions for the uncertain parameters, given prior beliefs on the parameters and experimental fatigue life data. Uncertainties can also arise from variable loading, but in this work, we consider constant strain amplitude loading. Following Bayesian inference, the quantified uncertainties of the parameters are forward propagated through the model, in order to make predictions of fatigue life, using Monte Carlo sampling. This helps to quantitatively relate the input uncertainties to the output. A brief overview of how the uncertainty quantification and propagation framework fits in with the fatigue model is shown in Fig. 1.4.

3. MICROSTRUCTURE BASED FATIGUE LIFE PREDICTION FRAMEWORK

3.1 Material Characterization

A nickel-base superalloy, RR1000, developed by Rolls-Royce plc is used in this study. The material produced using powder metallurgy process underwent forging and was heat-treated above the γ' solvus (at 1170°C) for 5 hours [11]. RR1000 is a precipitation hardened material and the ordered γ' precipitates present in the material provide a strengthening mechanism and stability at elevated temperatures. The heterogeneities present in the microstructure are quantified based on EBSD data. These complex heterogeneities govern strain localization within the material and affect fatigue life. Quantitative characterization of the microstructure provides information on orientation distribution (to understand texture of the material), grain size distribution, grain boundary character distribution (GBCD) of special type of GBs called coincident site lattice (CSL) GBs and misorientation distribution (to spatially understand the neighbor orientations). Such a characterization not only helps in linking microstructure to properties but also provides benchmark statistics based on which SEMs can be generated. The statistics of aforementioned microstructural heterogeneities for RR1000 (obtained using DREAM.3D) are shown in Fig. 3.1. It is evident from the pole figures (shown in Fig. 3.1a) that RR1000 does not have any texture, and from Fig. 3.1c that a majority of CSL GBs in RR1000 are TBs. The misorientation distribution (shown in Fig. 3.1d) shows

a peak at 60°, implying a large number of twins present in the material, compared to a Mackenzie distribution, which corresponds to a material with a random texture and has either none or relatively low number of twins.

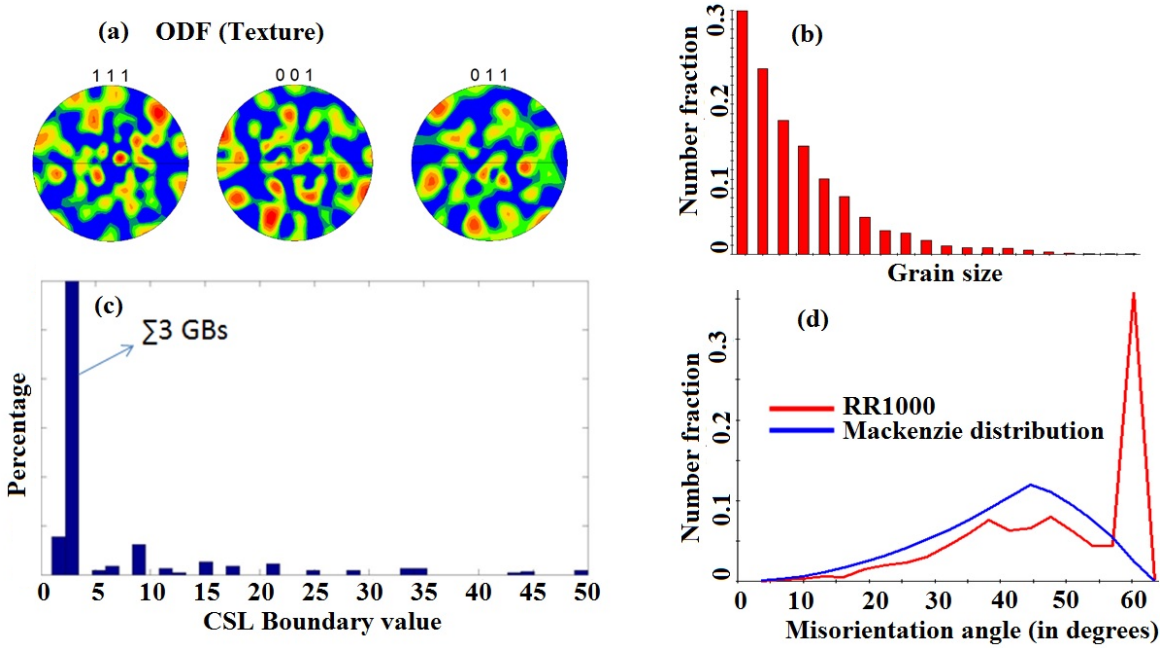

Figure. 3.1. Microstructure characterization of RR1000.

3.2 Statistically Equivalent Microstructures (SEMs)

SEMs are virtual microstructures, built to statistically represent the (morphological and crystallographic) heterogeneities of the microstructure of the material, as closely as possible. In order to enhance the predictive capabilities of the microstructure based failure prediction model, the representation of the microstructure must capture the variability observed in the material. For this purpose, the statistics of the different morphological and crystallographic characteristics mentioned above are accounted for, while creating the SEMs that are representative of RR1000. For instance, a random texture was assigned to the SEMs generated, as the texture of RR1000 was observed to be random (Fig. 3.1a).

The data at hand is the 2D microstructure of the material that is derived from an EBSD scan of the material. To fully characterize grain structure, direct 3D data is a necessity, but due to the lack of availability of the 3D material data, certain (stereological and other modeling) assumptions have to be made while transitioning from 2D to 3D. Two main assumptions are made in obtaining the 3D grain size distribution from the 2D grain size distribution. First, it is assumed that the grain size in the 3D SEM would follow a log-normal distribution. This appears to be a valid assumption as a wide variety of metals and alloys have a log-normal grain size distribution [105]. The second assumption is to scale the 2D grain sizes obtained from 2D EBSD data, with a stereological scaling factor $\frac{4}{\Pi}$. Groeber [106] showed that this scaling is reasonable and the error is within 5% by comparing the scaled data obtained from 2D microstructure data of a nickel-base superalloy, IN100, with its real 3D microstructure data.

Grain shape distributions are not as straight forward as the grain size distributions. The irregular geometries that are typical features of grains in a polycrystalline material make it difficult to unambiguously describe the shapes of grains. Due to the lack of availability of the 3D data of RR1000, the grain shape distribution parameter (in the form of moment invariants) information was extracted from the experimental 3D data set of a sub-solvus heat treated nickel-base superalloy, IN100 [18]. This information was input into DREAM.3D [18, 19] to define the shapes of the grains in the equivalent microstructure.

A characteristic feature of the microstructure of RR1000 is the considerably high number of annealing twins. Hence the GBCD of the SEMs generated should show a high frequency of annealing twins to mimic the real microstructure as closely as possible.

Annealing twins were inserted into the microstructure using a twin-insertion code [107]. The code chooses one of the four variants (and their conjugates) of the <111> planes at random and the corresponding grain orientation for the twin is calculated by rotating the orientation of the parent grain 60° about the same <111> variant that was chosen. The percentage of annealing TBs (with respect to all CSL GBs in the SEM) in the SEMs closely matched the values observed in real microstructure data. All the twins inserted into the microstructure are continuous within their respective parent grain and do not have discontinuities like steps, ledges/twin tips.

The statistics obtained from the 2D characterization of the material followed by stereological assumptions is input into the 'StatGenerator' toolbox in DREAM.3D, which creates SEMs, following which surface meshes of these microstructures can be generated. These surface meshes were converted into a volume mesh using PPM [21]. Figure 3.2 gives a brief overview of the process involved in the generation of SEMs, which are then volume meshed to be used in a CPFE framework.

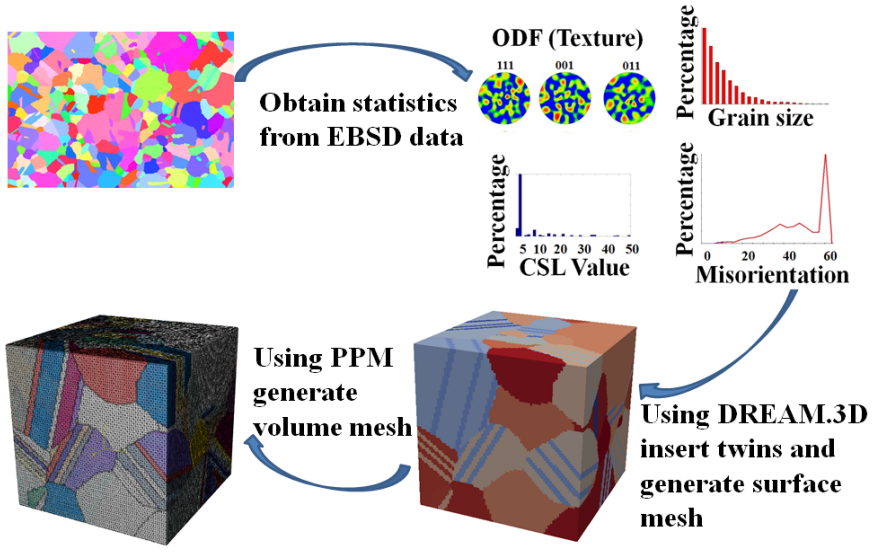

Figure 3.2. Workflow for generating statistically equivalent microstructures.

An important step in the generation of SEMs is the comparison of the statistics of the microstructural attributes of SEMs and EBSD scans. Hence a verification step in embedded into the SEM generation module to check if microstructural attributes in microstructures generated are in good agreement with that observed in EBSD data. First, a student t-test is used to test the hypothesis if the lower order moments (mean and variance) of grain size distribution in the microstructures generated are equal those obtained from stereologically scaled grain sizes extracted from EBSD scans. Since we are interested in calculating the scatter in fatigue life and not the absolute minimum fatigue life, we are not using the higher order moments (skewness and kurtosis) of grain size distribution as verification metrics. These higher order moments, when used, will help select microstructures that capture extreme values of grain sizes which help in estimating minimum fatigue life. The microstructures generated using the lower order moments as verification metrics (for grain size) also capture some ALA grains whose sizes are in the same range as those estimated from EBSD scans (as evident from Fig. 3.4a). Second, the percentage of TBs (with respect to all CSL GBs) in the microstructure generated is used as an additional verification metric to check the statistical equivalence of the microstructures generated. A synthetic microstructure generated is considered as an SEM, only after verifying that there is a close match between the statistics of the aforementioned microstructural attributes (lower order moments of grain size distribution and percentage of TBs with respect to all CSL GBs) of SEMs and EBSD scans. The flowchart for the module that automates generation of SEMs is shown in Fig 3.3, which also gives a clear picture of the verification steps. A comparison of the grain size and CSL GB distributions from EBSD scans and SEMs generated in shown in Fig. 3.4.

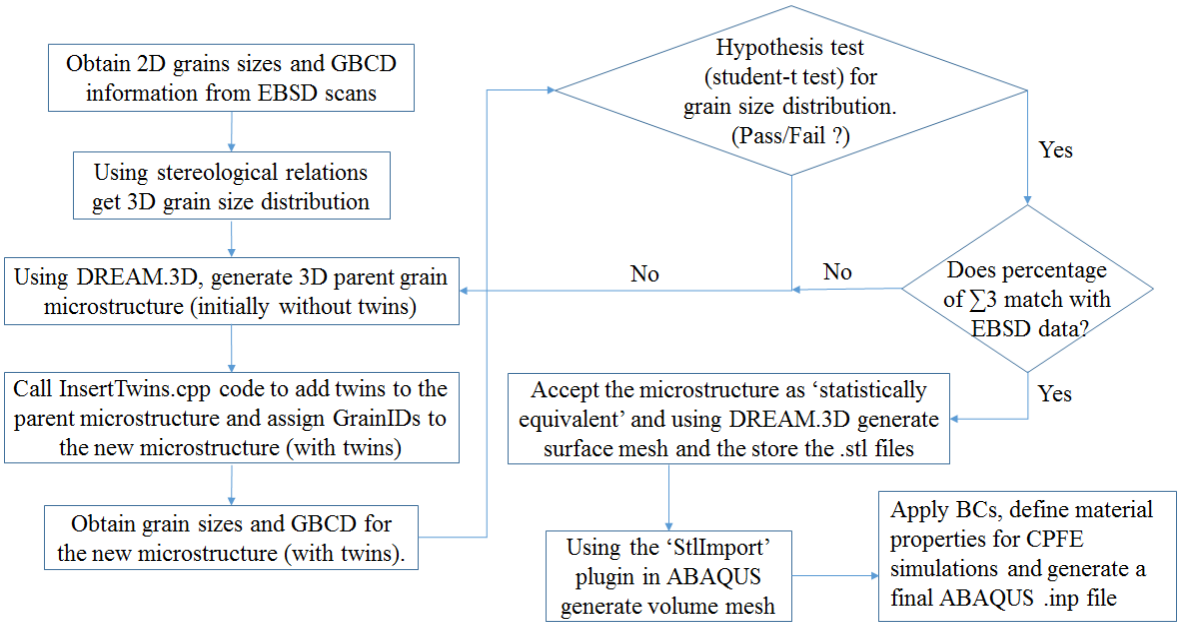

Figure 3.3. Flowchart of the SEM generation and verification module.

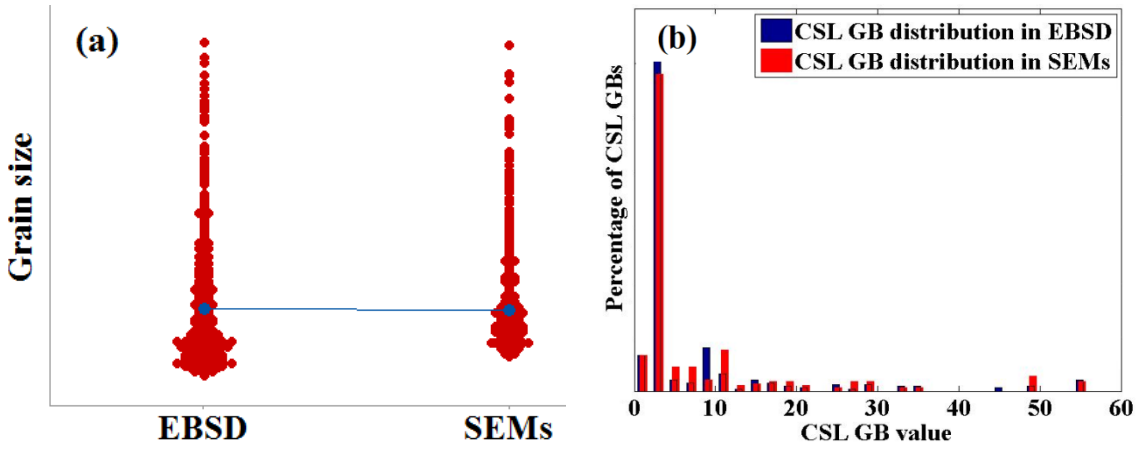

Figure 3.4. (a) Comparison of stereologically scaled grain size values obtained from EBSD scans with the sizes of grains in SEMs generated, using an individual value plot in MINITAB [108]. The location of the two blue circles corresponds to the mean grain size value in EBSD data and SEM data, (b) comparison of GBCD in EBSD with that of the SEMs generated.

3.3 PSB Energy Based Fatigue Model

The fatigue model presented in the current study uses the stability of a PSB to define crack initiation. The model uses a modified version of the PSB energy expression developed by Sangid et al. [23,24,69]. The definition of the energy of a PSB is enriched, by taking the outputs of CPFE based calculations, including the normal stress, back stress, resolved shear stress and accumulated strain in a slip system. This information along with the GB energetics is fed into the PSB energy based failure prediction model (or PSB model) to predict the potential location of crack nucleation. Figure 3.5 displays a schematic of a PSB formed in a nickel-base superalloy, based on shearing of γ' precipitates. In the schematic shown, a PSB traverses a LAGB and is impeded by a HAGB (for example an annealing TB), where the dislocations pile-up, form extrusions at the boundary plane, and thereby concentrates stress at the boundary. With this established view of a PSB (based on experimental observations), we define the energy of a PSB as follows:

$$E_{PSB} = E_{\text{atomistic scale contributions}} + E_{\text{continuum scale contributions}} \tag{3.1}$$

$$E_{\text{atomistic scale contributions}} = E_{\gamma \text{ and } \gamma' \text{shearing}} + E_{\text{extrusion formation at GBs}} \tag{3.2}$$

$$E_{\gamma \text{ and } \gamma' \text{ shearing}} = \sum_i \partial X_i \left(f \int_0^L \gamma_{APB} dL + (1-f) \int_0^L \gamma_{SFE} dL \right) n_{eff}^{layers} \tag{3.3}$$

$$E_{\text{extrusion formation at GBs}} = \sum_i \partial X_i \left(E_{slip-GB}^{\gamma-MD} n_{ext-GB}^{dis} bh \right) \tag{3.4}$$

$$E_{\text{continuum scale contributions}} = -E_{\text{applied work}} - E_{\text{hardening}} + E_{pile-up} \tag{3.5}$$

$$E_{\text{applied work}} = \sum_i \partial X_i \left(bLn^{layers} \Delta\tau^{\alpha}_{CPFEM} \right) \tag{3.6}$$

$$E_{\text{hardening}} = \sum_i \partial X_i \left(bLn^{layers} \sigma_{\text{hardening}} \right) \tag{3.7}$$

$$E_{\text{pile-up}} = \sum_i \partial X_i \left(bLn^{layers} \sigma_{\text{pile-up}} \right) \tag{3.8}$$

Putting all the above energy expressions together, the total energy of a PSB is mathematically expressed as follows:

$$E_{PSB} = \sum_i \partial X_i \left(f \int_0^L \gamma_{APB} dL + (1-f) \int_0^L \gamma_{SFE} dL \right) n_{eff}^{layers} + \sum_i \partial X_i \left(E_{slip-GB}^{\gamma-MD} n_{ext-GB}^{dis} bh \right) + \sum_i \partial X_i \left(\sigma_{\text{pile-up}} - \Delta\tau^{\alpha}_{CPFEM} - \sigma_{\text{hardening}} \right) bLn^{layers}, \tag{3.9}$$

where ∂X_i is the incremental slip within PSB, f is the volume fraction of the γ' precipitate phase, γ_{SFE} is the stacking fault energy of the γ phase, γ_{APBE} is the anti-phase boundary energy of the γ' precipitate, n_{eff}^{layers} is the number of effective layers contributing to SFE or APBE, L is the length of the PSB, $E_{slip-GB}^{\gamma-MD}$ is the energy required for a dislocation to transmit across a GB, n_{ext-GB}^{dis} represents the number of dislocations forming an extrusion at the GB, b is the magnitude of the Burgers vector, h is the width of the PSB, $\Delta\tau^{\alpha}_{CPFEM}$ is applied cyclic stress on the PSB, $\sigma_{\text{hardening}}$ accounts for the hardening within the PSB, $\sigma_{\text{pile-up}}$ is the pile-up stress at the intersection of the PSB and the GB, and n^{layers} is the number of slip planes within the PSB, which is related to the PSB width, h as $n^{layers} = \frac{h}{b}$.

Failure (e.g. fatigue crack initiation) would occur when the energy of the PSB would attain its minimum value. Mathematically speaking, cracks would initiate when the following conditions are satisfied:

$$\frac{\partial E_{PSB}}{\partial X_i} = 0 \text{ and } \frac{\partial^2 E_{PSB}}{\partial {X_i}^2} > 0 \quad (3.10)$$

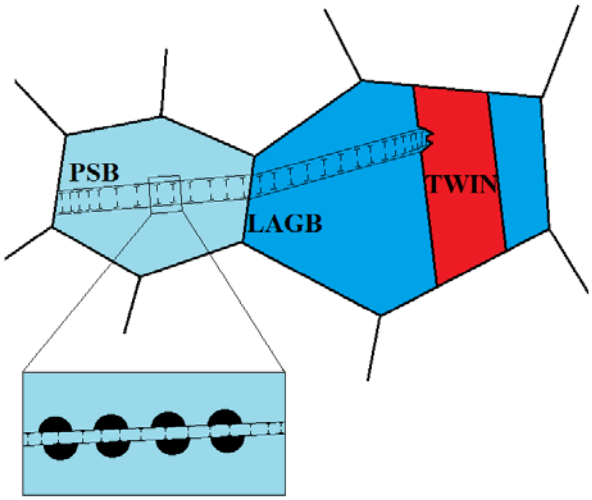

Figure 3.5. Schematic of a PSB.

3.3.1 Atomistic Level Contributions

Atomistic level deformation mechanisms which contribute to fatigue failure are taken into consideration in the current fatigue model. Dislocations exist within a PSB by shearing the matrix and the γ' precipitates and pile-up at the GBs to form extrusions. The energy that goes into aforementioned deformation mechanisms was calculated using MD simulations in LAMMPS [109].

3.3.1.1 Shearing of Matrix and Precipitates

At intermediate temperatures, dislocations were observed to shear γ' precipitates in RR1000 [110]. For a dislocation within a PSB to shear through the γ matrix (Ni) and γ' precipitate (Ni_3Al), it has to overcome the energies associated with destroying the stacking sequence of an FCC structured Ni and an ordered $L1_2$ structured Ni_3Al, which are defined as the stacking fault energy (SFE) and the anti-phase boundary energy

(APBE), respectively. Embedded atom potentials from Foiles-Hoyt [111] and Mishin [112] were used to calculate the SFE and APBE curves for γ and γ' phases, respectively. Based on these energies, the total energy required by a PSB of length L, to shear through a matrix and precipitate phase is given by:

$$E_{\gamma \text{ and } \gamma' \text{shearing}} = \sum_i \partial X_i \left(f \int_0^L \gamma_{APB} dL + (1-f) \int_0^L \gamma_{SFE} dL \right) n_{eff}^{layers}. \qquad (3.11)$$

In multi-axial fatigue, the critical plane is a combination of having the maximum normal stress and shear strain according to the description of Fatemi-Socie [113]. The concept of normal stress acting as a driving force for crack initiation [113] and growth has been extended to microstructural sensitive fatigue models [87], which is adopted in this analysis. It is established that SFE and APBE are affected by an application of normal stress (or strain) on the slip system [114,115]. As depicted in Fig. 3.6, the application of tensile normal stress moves the atom layers apart which makes it easy for slip to occur on the slip planes, thereby reducing the SFE (or APBE) and vice versa. SFE and APBE curves (for Ni and Ni_3Al phases respectively) have been plotted for various normal strains (Fig. 3.7a and b). The normal strains were applied along the <111> direction perpendicular to the slip planes. It is evident from the plots that the respective energies increased with an application of compressive normal strain and decreased with an application of tensile normal strain consistent with previous studies [114,115].

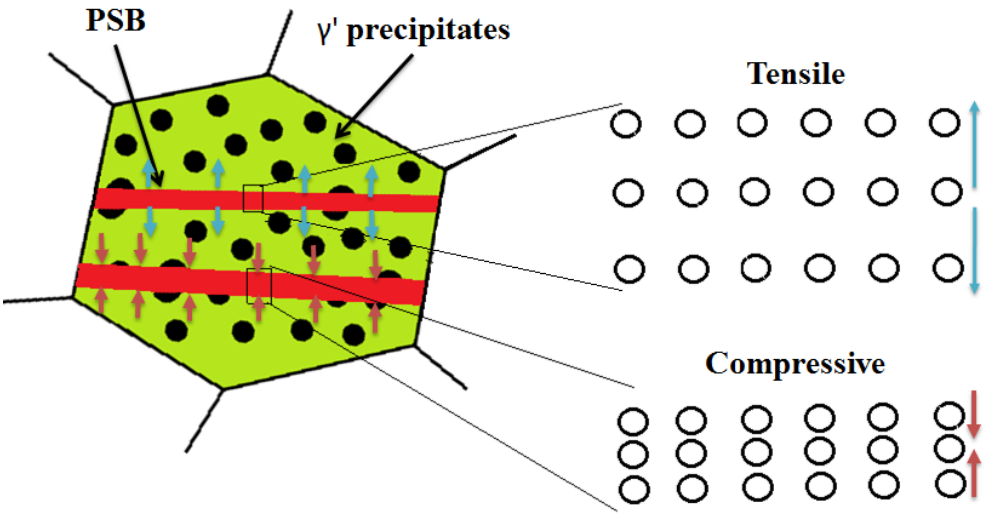

Figure 3.6. Schematic of normal stresses acting on PSB, stretching (or compressing) the lattice, shown in the inlet figures.

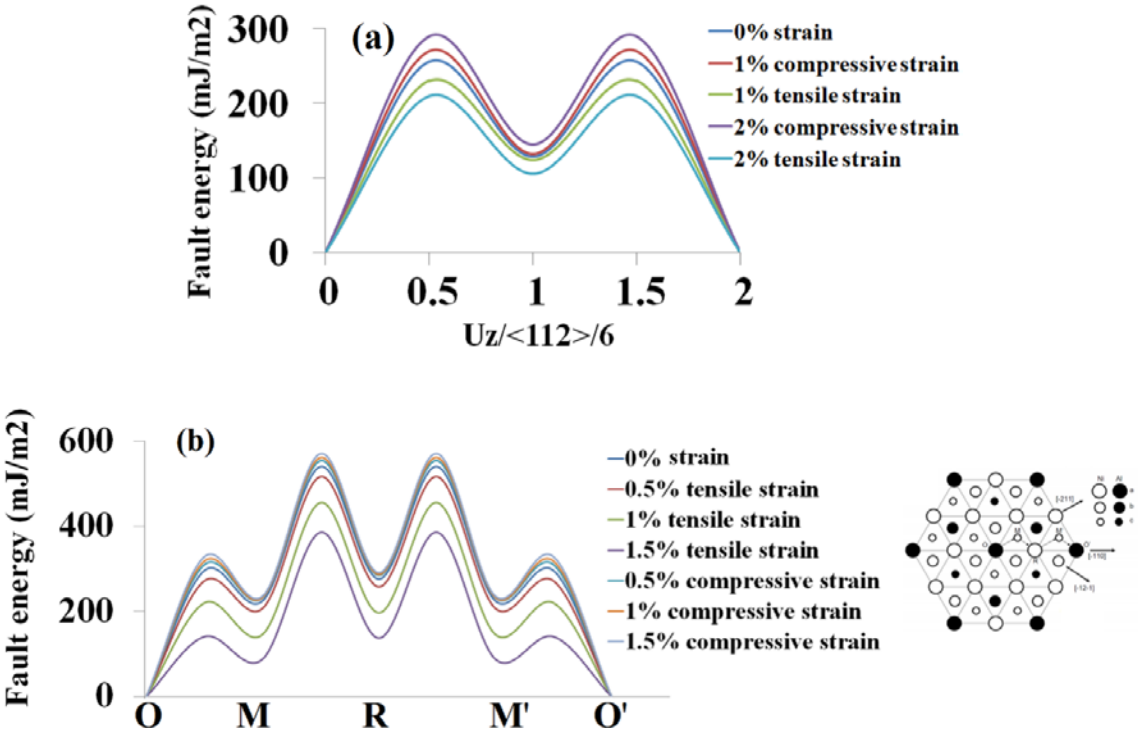

Figure 3.7. (a) SFE curve for various applied normal strains. (b) APBE curve for various applied normal strains, (inlet schematic was redrawn based on schematic from Rice et al. [116]).

3.3.1.2. Extrusion Formation

As discussed earlier, a PSB is impeded by a HAGB, and due to this, the dislocations within the PSB pile-up at the GB. Stress concentration at the GB increases and leads to activation of slip systems in the neighboring grains. As a result, dislocations could be partially transmitted across the GB leaving behind a residual dislocation at the GB [117]. Strain incompatibility and discontinuous nature of slip at GBs leads to accumulation of residual dislocations at the GBs and hence extrusion formation, with repeated cyclic loading [47]. This in turn raises the stress concentrations at the PSB-GB interface due to extrusion formation. The energy needed for a dislocation to form an extrusion depends on the type of the GB. From the plot in Fig. 3.8 (reproduced from Sangid et al. [23]), TB offers the highest barrier to dislocation transmission. Depending upon the type of the GB and the number of dislocations forming an extrusion at the GB, the energy required by a PSB to form an extrusion, $E_{\text{extrusion formation at GBs}}$, is given as follows:

$$E_{\text{extrusion formation at GBs}} = \sum_i \partial X_i \left(E_{\text{slip}-\text{GB}}^{\gamma-\text{MD}} n_{\text{ext}-\text{GB}}^{\text{dis}} bh \right). \tag{3.12}$$

The calculation of number of dislocations penetrating a GB, $n_{\text{ext}-\text{GB}}^{\text{dis}}$, is not straight forward and it was calculated based on empirical relations. In order to consider the evolution of cyclic slip irreversibilities due to formation of extrusions, empirical formulation of extrusion growth with an increasing number of cycles is incorporated into the model, as rigorous experimental data are not available for the evolution of extrusion at GBs. There is a vast amount of work done in understanding how PSBs evolve at the surface. Risbet et al. [40,59] measured extrusion heights at the surface of a nickel-base

superalloy using AFM techniques. It was observed that extrusions appeared after a threshold number of loading cycles, N_{offset}. The number of dislocations within the extrusions is assumed to follow a square root dependency on the number of fatigue cycles, based on the model of Essmann, Gösele, Mughrabi [35]:

$$n_{ext-GB}^{dis} \propto \sqrt{N - N_{offset}}, \tag{3.13}$$

where N_{offset} is calculated based on the condition that the applied stress $(\tau^{\alpha} + \sigma_{pile-up})$ on a dislocation within a PSB impinging upon the GB must be greater than the transmission resistance offered by the GB. This GB resistance to PSBs is calculated using Stroh's formulation [118] assuming that the PSB is favorably aligned to the GB to form extrusions and hence initiate a crack. Christ [119] used this relation of GB cracking due to pile-ups to study PSB-GB interaction. Their expression calculates the stress required by a pile-up to nucleate a crack, which was formulated to be dependent on the surface energy (γ) of the material. We replace this term with the GB energy calculated from MD simulations to quantify various GBs resistance to dislocation transmission and extrusion formation. Hence the model calculates n_{offset} based on the condition that extrusions would cross a GB when the applied stress $(\tau^{\alpha} + \sigma_{pile-up})$ is greater than the GB resistance (σ_{stroh}). Also the number of dislocations that penetrate the GB increases with an increase in the applied stress:

$$n_{ext-GB}^{dis} \propto \frac{\tau^{\alpha} + \sigma_{pile-up} - \sigma_{stroh}}{\sigma_{stroh}}, \tag{3.14}$$

where the resolved shear stress τ^{α} is taken from CPFE calculations, $\sigma_{pile-up}$ is calculated based on the relation between long range pile-up stresses in terms of slip system strain, formulated by Schouwenaars et al. [120] as follows:

$$\sigma_{pile-up} = \frac{1.8\mu\gamma^{\alpha}}{\pi(1-v)}. \tag{3.15}$$

Here μ is rigidity modulus, v is the Poisson's ratio and γ^{α} is accumulated strain in the slip-system which is calculated from the CPFE simulations. As mentioned earlier, σ_{stroh} is calculated based on the Stroh's formulation [118], expressed as follows:

$$\sigma_{stroh} = \left\{\frac{\pi E_{GB}^{trans}\mu}{2(1-v)L}\right\}^{\frac{1}{2}}, \tag{3.16}$$

where E_{GB}^{trans} is the dislocation transmission energy [86] of a GB and its value for various types of CSL GBs is shown in Fig. 3.8, L is the length of the PSB. It is noted that n_{ext-GB}^{dis} depends on the pile-up length itself; more dislocations form extrusions from PSBs with large pile-up lengths and hence a length dependence is added to the model

$$n_{ext-GB}^{dis} \propto \frac{L}{L_{avg}}, \tag{3.17}$$

where L is the pile-up length and L_{avg} is the average pile-up length of all the PSBs formed.

Finally, a strain rate dependence is also established as to differentiate between slip systems with higher strain rate (which accumulate more slip and hence dislocations) and lower strain rates.

$$n_{ext-GB}^{dis} \propto \frac{\dot{\gamma}^{\alpha}}{\dot{\gamma}_o}, \tag{3.18}$$

where $\dot{\gamma}^{\alpha}$ is the slip system strain rate and $\dot{\gamma}_o$ is the reference strain rate for all slip systems. It is added in the denominator for the expression to be dimensionally consistent. From the flow rule used in the crystal plasticity formulation used in this framework (described in Section 3.4), we have $\dot{\gamma}^{\alpha} = \dot{\gamma}_o \left|\frac{\tau^{\alpha}-\chi^{\alpha}}{g^{\alpha}}\right|^{m}$, where m is the rate sensitivity parameter, τ^{α} is resolved slip-system stress, χ^{α} is back stress on a slip system and g^{α} is the critical resolved shear stress. Combining the individual empirical formulations we define the number of dislocations penetrating the GB to form an extrusion, n_{ext-GB}^{dis}, as follows (by assuming proportionality constant k):

$$n_{ext-GB}^{dis} = k\left|\frac{\tau^{\alpha}-\chi^{\alpha}}{g^{\alpha}}\right|^{m} \frac{L}{L_{avg}}\left(\frac{\tau^{\alpha}+\sigma_{pile-up}-\sigma_{stroh}}{\sigma_{stroh}}\right)\sqrt{N-N_{offset}}. \tag{3.19}$$

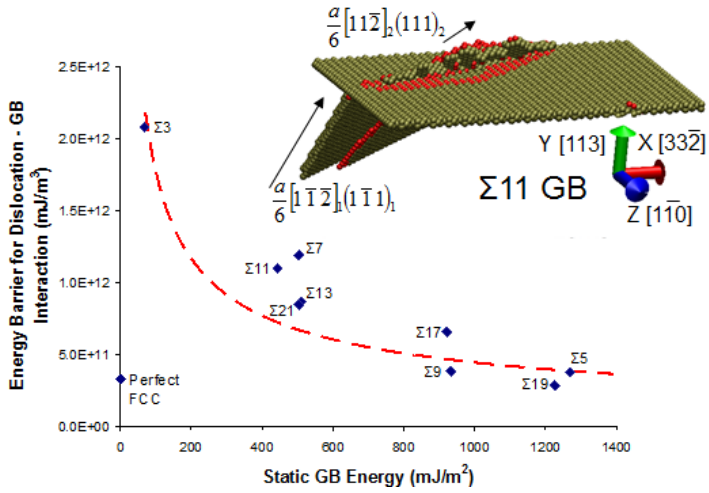

Figure 3.8. Energy barrier for dislocation transmission across various types of CSL GBs (figure taken from Sangid et al. [23]).

The PSB model uses energy barriers calculated from atomistic simulations. These values for the static GB energies (for distinct CSL GBs in Ni [23,121]), dislocation transmission energy barriers and dislocation nucleation energies for CSL GBs [23], stacking fault energy and anti-phase boundary energy values (shown in Fig. 4) are stored within a database and called within the PSB energy balance when needed. Using the energy values from a database makes the PSB model computationally very efficient, as MD simulations do not have to be run on a repetitive or hierarchical basis. These material models (relying on values, a priori, calculated and stored in databases) are easier to implement in practice due to their computational efficiency, as demonstrated by a spreadsheet based model developed by Parthasarathy et al. [122] to calculate the yield strength of superalloys.

3.3.2. Continuum Level Contributions

In the continuum scale, the PSB is subjected to an i) external stress field created due to the applied load, constrained deformation of neighboring grains and ii) internal stress fields due to long range pile-up stresses and hardening that occurs within the PSB. The continuum level description of dislocations contribution to the energy of a PSB is as follows:

$$\mathrm{E}_{\text{continuum scale contributions}} = \sum_{\mathrm{i}} \partial \mathrm{X}_{\mathrm{i}} \left(\sigma_{\text{pile-up}} - \Delta\tau^{\alpha}_{\text{CPFEM}} - \sigma_{\text{hardening}}\right) \mathrm{bLn}^{\text{layers}} \tag{3.20}$$

3.3.2.1. Applied Stress

PSBs have been observed to form along one of the slip systems. Hence due to an applied load, these PSBs will be subjected to a resolved shear stress (RSS) acting on the slip system. In order to consider the role of the grain interaction and the complex 3D stress states that form within each grain, the RSS is directly taken from the CPFEM simulations. Within the CPFEM constitutive models [123], the RSSs are calculated by the expression $F^{eT}F^{e}S^{*}:(s^{\alpha} \otimes m^{\alpha})$, where F^{e} is the elastic part of the deformation gradient ($F=F^{e}F^{p}$ [124]), S^{*} is the 2nd Piola Kirchoff stress, $(s^{\alpha} \otimes m^{\alpha})$ is the Schmid tensor. It is assumed in this model that PSB forms on the slip system with maximum RSS. Hence $\Delta\tau^{\alpha}_{\mathrm{CPFEM}}$ is calculated for that slip system which showed a maximum range of resolved shear stress over a cycle.

It is also observed that for the most active slip system within a grain (composed of thousands of material points in the finite element mesh) the percentage of standard deviation of RSS with respect to the average value of RSS calculated over all material points is less than 5% showing that if it is an active slip system then all the material points have similar values of resolved shear stress with an error of +/- 5%. On the contrary, if the slip system is inactive (with the resolved shear stress less than the critical resolved shear stress) then the percentage of standard deviation of RSS with respect to the average value of RSS calculated over all material points is greater than 40%, inferring the large variance of RSS values over the domain of the material points that belong to that particular grain. Following this argument based on statistical observation, we compute the average resolved shear stress of all the slip systems, and only consider the maximum value (pertaining to the most active slip system) from the twelve obtained values. The

maximum RSS value is used in the energy expression of the PSB. Therefore, the applied cyclic stress $\Delta\tau^{\alpha}_{\mathrm{CPFEM}}$ is calculated for the most active slip system, in an average sense over all material points that belong to a grain. The $\Delta\tau^{\alpha}_{\mathrm{CPFEM}}$ is calculated from peak to minimum applied load, thus accounting for the cyclic nature of fatigue.

3.3.2.2. Dislocation pile-up

As discussed earlier, long-range pile-up stresses develop within the PSB due to the pile-up of dislocations at the intersection of PSB-GB. Schouwenaars et al. calculated the average of the stress fields of pile-ups with randomly distributed numbers of dislocations [120]. For such a stress field which has a non-zero average stress, they derived an expression for the maximum value of the pile-up stress and showed that it would increase linearly with accumulated slip system strain during incipient deformation, and in addition showed, that it is independent of the grain size. We adapt their formulation of pile-up stress into our continuum definition of pile-up stress and calculate it by obtaining the accumulated slip system strain, γ^{α}, for the most active slip system already determined (as described in Section 3.3.2.1)

$$\sigma_{\mathrm{pile-up}} = \frac{1.8\mu\gamma^{\alpha}}{\pi(1-\nu)}. \tag{3.21}$$

High stress and displacement fields developed due to the pile-up of dislocations at the PSB-GB intersection trigger cracks to nucleate. Hence it is worthwhile to study the stress-fields due to a pile-up of dislocations and the associated displacement fields, which present an opening length-scale to promote a crack to nucleate. For this purpose, a dislocation pile-up was considered with twenty edge-dislocations, with their Burgers vector pointing in X-direction, while the dislocation line direction pointed in the Z-

direction, as shown in Fig. 3.9a. Hence from the elastic description of edge-dislocations, the strain and the displacement fields in the Z-direction are zero. This makes it a plane strain problem in the XY plane. For the plot in Fig. 3.9, the material is assumed isotropic and image forces at the GB are not considered in calculating the equilibrium positions of dislocations. For this setup we calculated the equilibrium positions of dislocations in a pile-up subjected to a resolved shear stress of 100 MPa. The stress field σ_{YY} and the displacement-field U_{yy} were plotted to understand the driving forces for crack opening along the YY direction. The stress-field, σ_{YY}, around an edge dislocation is given by [125]:

$$\sigma_{YY} = \frac{-\mu b}{2\pi(1-v)} \frac{y(x^2-y^2)}{(x^2+y^2)^2}. \tag{3.22}$$

The displacement-field, U_{yy}, around an edge dislocation is given by [126]:

$$U_{yy} = \frac{b}{2\pi}\left(\frac{1-2v}{2(1-v)} \ln \frac{1}{\sqrt{x^2+y^2}} + \frac{1}{2(1-v)} \frac{y^2}{x^2+y^2}\right). \tag{3.23}$$

The stress and displacement fields due to the dislocation pile-up are shown in Fig. 3.9 b and c. It can be observed that the stress field at the intersection of the pile-up and the GB is at its peak, whereas the peak of the displacement field is slightly offset from the pile-up and GB intersection, possibly leading us to insights on why cracks initiate at a slightly offset distance from the TBs, rather than at the TBs [11,74,75].

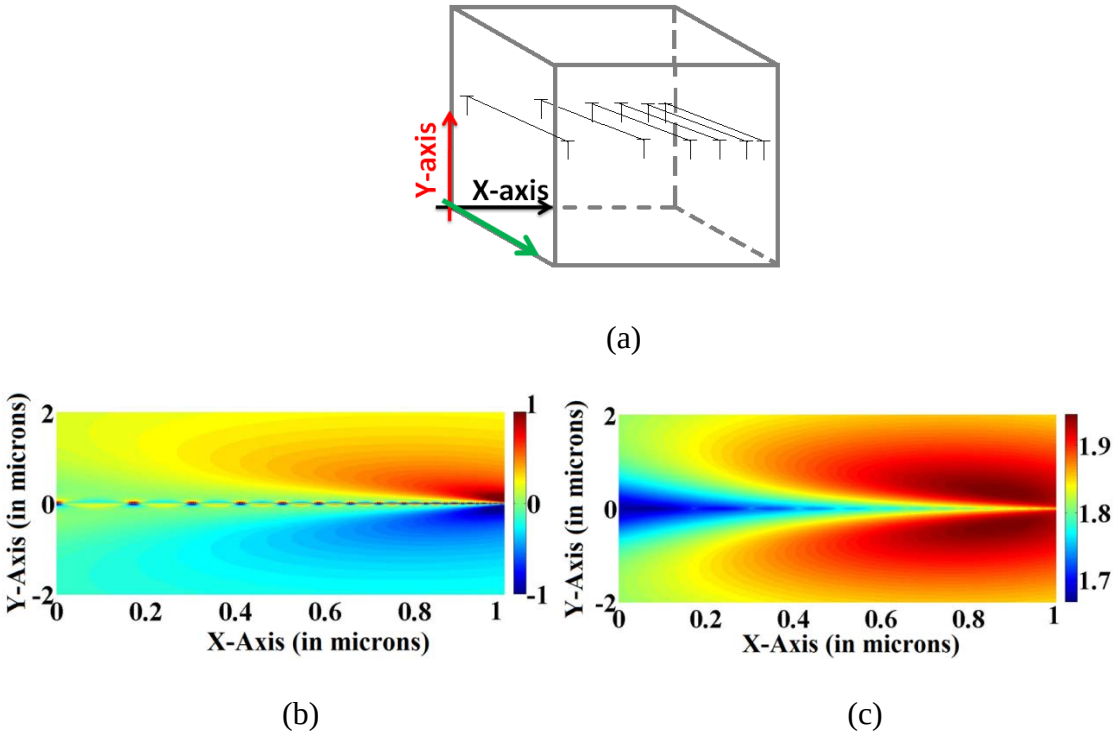

(a)

(b) (c)

Figure 3.9. (a) Coordinate system of the pile-up, (b) σ_{yy} field due to the pile-up (units of the stress are in GPa), and (c) U_{yy} displacement field due to the pile-up (units of displacement are in nm).

Significant work-hardening occurs within the PSB and evolves within the PSB according to the Taylor hardening relation [127] given by:

$$\sigma_{\text{hardening}} = 0.45\mu b\sqrt{\rho}, \tag{3.24}$$

where ρ is the dislocation density within the PSB.

3.4 Crystal Plasticity Finite Element (CPFE) Framework

Crystal plasticity forms a bridge between applied macroscopic load and micro-mechanical response at a slip-system level. The CPFE framework combines anisotropic elasticity with rate dependent crystal plasticity kinetics. It must be noted that inelastic

deformation is not only a result of crystallographic slip, it may also occur via twinning, diffusion, and GB sliding. In the current framework, plastic flow occurs primarily through dislocation glide, at the temperature of interest (e.g. an intermediate elevated temperature).

The values of independent cubic elastic constants, C_{ij}, are used to solve for anisotropic elastic response of the polycrystalline nickel-base superalloy, RR1000. As the γ' phase is not being explicitly modeled, the C_{ij} values are homogenized using the first order Voigt-Reuss-Hill (VRH) method [128] as follows:

$$C_{ij} = 0.5\left(fC_{ij}^{\gamma'} + (1-f)C_{ij}^{\gamma} + \frac{C_{ij}^{\gamma}C_{ij}^{\gamma'}}{fC_{ij}^{\gamma'} + (1-f)C_{ij}^{\gamma}}\right), \tag{3.25}$$

where f is the volume fraction of the γ' phase and C_{ij}^{γ} represent elastic constants of Ni and $C_{ij}^{\gamma'}$ represent the elastic constants of γ' phase**.** Kuhn et al. [128] showed that the difference between the simpler first-order rules (like the VRH rule) and higher-order structure-property rules (which take into account volume fraction, shape, orientation, and orientation distribution of a second phase) for a material containing globular γ' precipitates is less than 1% and hence justified the use of VRH rule to calculate homogenized elastic constants for nickel-base superalloys.

In RR1000, the volume fraction of γ' phase is 48% [129]. The C_{ij}^{γ} and $C_{ij}^{\gamma'}$ values of both the phases at the elevated temperature of interest, are taken from literature [130,131]. The elastic constants obtained from VRH method gave a very close value for the Young's modulus when a virtual microstructure was subjected to an elastic strain, however there was still 5% error, when compared to the experimental value. Hence the

values of C_{ij} were adjusted using a binary search method, during which the C_{ij} values were adjusted until the Young's modulus value matched accurately with the experimental value. The final C_{ij} values obtained are as follows:

$$C_{11} = 234.52 \text{ GPa}, C_{12} = 130 \text{ GPa}, C_{44} = 103 \text{ GPa}.$$

The flow rule describing incremental slip system strain is adapted in this framework:

$$\dot{\gamma}^{\alpha} = \dot{\gamma}_{o} \left| \frac{\tau^{\alpha} - \chi^{\alpha}}{g^{\alpha}} \right|^{m} \operatorname{sgn}(\tau^{\alpha} - \chi^{\alpha}), \tag{3.26}$$

where $\dot{\gamma}^{\alpha}$ is the shearing rate of slip-system α, $\dot{\gamma}_{o}$ is the reference shearing rate, τ^{α}, χ^{α}, g^{α} are the corresponding slip system shear stress, back stress (that accounts for Bauschinger effects) and critical resolved shear stress (or slip resistance which delays the onset of plastic deformation), respectively. The slip resistance and back stress evolve according to an Armstrong–Frederick hardening model [132]:

$$\dot{g}^{\alpha} = H \sum_{\beta=1}^{N} q^{\alpha\beta} \left| \dot{\gamma}^{\beta} \right| - R g^{\alpha} \sum_{\beta=1}^{N} \left| \dot{\gamma}^{\beta} \right| \tag{3.27}$$

$$\dot{\chi}^{\alpha} = c\dot{\gamma}^{\alpha} - d\chi^{\alpha} |\dot{\gamma}^{\alpha}|, \tag{3.28}$$

where H and R are the direct hardening and dynamic recovery coefficients, respectively, for the isotropic hardening relation (eq. 3.27) and c and d are the direct hardening and dynamic recovery coefficients, respectively, for the non-linear kinematic hardening relation (eq. 3.28), $q^{\alpha\beta}$ refers to hardening coefficient for interaction between slip systems, and is assigned a value of 1 (for self-hardening) and 1.2 (for latent-hardening).

There are a total of nine fitting parameters in the CPFE framework. The effect of each of the parameters on the macroscopic response was determined by doing sensitivity

analysis, after which the parameters were fit to match the stress-strain curve response to that of the experimental macroscopic response for the first fatigue cycle (along with the response pertaining to tenth cycle and half-life), as shown in Fig. 3.10.

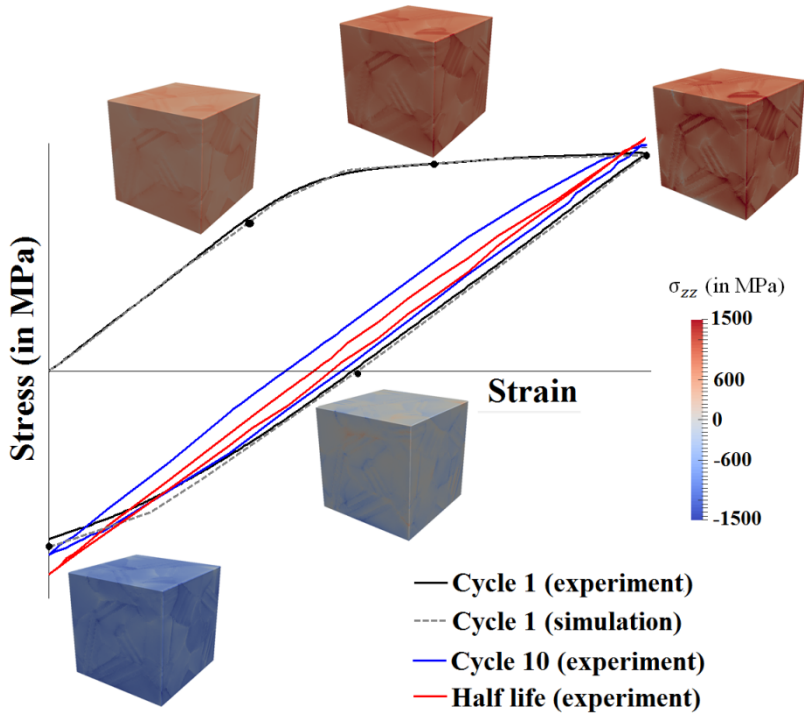

Figure 3.10. The macroscopic curve obtained by fitting the parameters to match the experimental macroscopic stress-strain curve. The inlets show contour plots of stress component in the loading direction.

It is not computationally feasible to run thousands of fatigue cycles using CPFE framework. Further, crystal plasticity cannot capture the formation of PSBs within the microstructure for the following two reasons. First, all the grains (within the SEM) are idealized by assigning a uniform orientation at every material point (or integration point) and homogenizing the response of the γ' precipitates, due to which, the orientation gradient and shearing of γ' precipitates required to capture the PSB is lost. Second, the

mesh size assigned to the volume mesh of the SEMs is on the order of a few microns, whereas the width of PSBs is on the order of tens to hundreds of nanometers. Reducing the mesh size to capture individual PSBs would increase the computational time by at least two orders of magnitude, thereby making it not amenable to carry out CPFE simulations. Hence we only simulate one fatigue cycle and leverage the resulting micromechanical data (RSS, normal stress, critical resolved shear stress, back stress, active slip systems, etc.) within the PSB model.

3.5 Integration of the Fatigue Model and CPFE Framework

From the previous discussion, it is clear that the PSB energy formulation needs slip-system level information like the resolved shear stress ($\Delta\tau^{\alpha}_{\mathrm{CPFEM}}$), normal stress ($\sigma^{\alpha}_{\mathrm{N}}$), critical resolved shear stress (g^{α}), back stress (χ^{α}), and accumulated plastic strain (γ^{α}) over the slip system on which the PSB forms. Apart from these quantities, the F^{e-1} tensor and effective accumulated plastic strain (p) at all the material points is also extracted to study the hot-spots (crack initiation sites predicted by the PSB energy based failure model) in detail. All the aforementioned parameters are called the state dependent variables (SDVs). In addition to the SDVs other geometrical information pertaining to the PSB (including its length, L, assuming that the PSB passes through the centroid of the grain along the slip system with maximum RSS) is also extracted from the surface mesh of the SEM. The SDV information ($\Delta\tau^{\alpha}_{\mathrm{CPFEM}}$, $\sigma^{\alpha}_{\mathrm{N}}$, χ^{α}, g^{α}, γ^{α}, p, F^{e-1}) from all the material points in every grain are extracted using an ABAQUS-Python interface. As it is assumed that the PSB forms on an active slip system with the highest resolved shear stress, in every grain the most active slip system is determined based on the maximum resolved shear stress criterion, as discussed in Section 3.3.2.1. For this slip system the normal

stress, critical resolved shear stress, back stress and the accumulated stain are also calculated.

For the sake of simplicity, it is also assumed that the PSB passes through the centroid of the grain. The length of the most active slip system passing through the centroid of the grain is calculated, by determining the two facets (in the surface mesh of the grain) on which the PSB would intersect and then finding the distance between the two intersection points. If the grain forms a cluster of grains joined by LAGBs (as shown in Fig. 3.5), the lengths of the PSBs in individual grains comprising the cluster are summed. Thus the geometric and the state variable information pertaining to the most active slip system on which the PSB formed (in grains or cluster of grains) is calculated and is fed into the PSB model. The flowchart in Appendix shows the framework of the fatigue model that begins from statistical characterization of real material's microstructure to the prediction of hot-spot within the SEM.

3.6 Results and Discussion

A representative volume element (RVE) encompasses a large enough volume that is representative of the material as a whole such that the predicted responses or properties do not change with a further increase of size [133,134]. Although by definition, an SEM is not related to the response of the material, with an increase in its volume, it can accurately capture a material response (or property) of interest, and hence, it can attain the essence of an RVE. In practice, the size of an RVE depends on the material response of interest. For instance, the size of an RVE to predict elastic modulus of a material is much smaller compared to the size of an RVE required to accurately predict fatigue life [134]. The scope of the current work is not to determine an RVE which captures all the

extreme value statistics of fatigue crack initiation, as such an RVE contains thousands of grains, making it a challenge to run computationally intensive CPFE simulations.

The fatigue framework simulates the microstructure variability by using many number of SEMs generated via Monte-Carlo algorithms in DREAM.3D, which takes into account, the statistical attributes of the real microstructure (as discussed in Section 3.2). Taking this as leverage, we generate many unique SEMs, which are randomly sampled populations of location specific microstructures within the component. We note that each of these samplings is independent. Although SEMs are small volume elements compared to an RVE, in this study, they are made sufficiently large to capture distributions of microstructural attributes (grain size, GB character, etc.) in addition to strength properties (elastic modulus, yield stress, hardening response and reverse plasticity upon unloading) of the material. Accordingly, a SEM in our work can be regarded as an RVE for the microstructural attributes and strength properties, but not for assessing the minimum fatigue life of the material. To capture the aforementioned properties, a SEM encompassing a minimum volume of 160x160x160 μm^3 and consisting of at least 150 grains serves as an RVE, which is in agreement with the estimation of Lin et al. [135], who defined the size of an RVE (for strength properties) for RR1000. These SEMs were created as per the schematic shown in Fig. 3.2, by first generating a parent microstructure having roughly around 50 grains (without twins), and then inserting 60 twins (making sure that no twins are inserted in parent grains which are already small, with grain sizes less than 10 μm) in such a way that the average grain size and the percentage of twins in SEMs match that of the real microstructure. For each individual SEM, the fatigue model deterministically calculates fatigue life on a grain-by-grain basis, assuming that a PSB

already exists on the most active slip system on every grain. By using multiple SEMs, thousands of grains can be probed by the fatigue model to obtain their respective fatigue lives. The resulting is pooled together to get a fatigue life distribution, in order to connect variability in microstructure to scatter in fatigue life.

In order to study the effect of the size of an SEM on the fatigue life distribution curve, three populations of SEMs were generated, with the first population consisting of 15 SEMs with 100 grains each, second population consisting of 10 SEMs with 150 grains each, and third population consisting of 7 SEMs with 200 grains each, in order to ensure a similar quantity of grains within each population. It is noteworthy to point out that as the size of an individual SEM increases (going from 100 grain to 200 grains), it attains the ability to capture the higher order moments of grain size distribution (skewness and kurtosis) in addition to capturing the lower order moments (mean and variance), which in turn enables a more appropriate analysis of those material responses that are specifically dependent on the extreme value attributes [136], for instance, the fatigue life [134]. Three fatigue life distribution curves were created (as shown on a log-log plot in Fig. 3.11), one for each population of SEMs, by pooling the fatigue lives obtained by probing the PSB model through all grains (or grain clusters) in a given population of SEMs. As the PSB model calculates fatigue life on a grain-by-grain basis (assuming a PSB exists in every grain), each data point shown in Fig. 3.11 corresponds to the fatigue life of a grain. The fatigue life distribution curve obtained from the third population of SEMs (with 200 grains in each SEM) captures the most conservative fatigue life due to the aforementioned reasons. The fatigue life distribution curve obtained from the second population of SEMs (with 150 grains in each SEM) for the most part overlays the third

population's fatigue life distribution curve, but is less conservative in nature. Finally, the fatigue life distribution obtained from the first population of SEMs (with 100 grains in each SEM) is farther away from the other two fatigue life distribution curves, and thereby reflecting on the fact that using SEMs with 100 grains is not appropriate to capture fatigue scatter. It is worthwhile to mention that the difference in the least fatigue life obtained by using the second and third population of SEMs is only a few cycles (approximately two orders of magnitude less than the scatter observed from experimental fatigue life data). We can capture the extreme minimum value for fatigue life data by using the population of SEMs with larger number of grains. But capturing the absolute minimum fatigue life data point is not the scope of the current research, as that would require us to define an RVE large enough to capture the least possible fatigue life. The current work focuses on capturing the scatter in fatigue life by simulating the variability in microstructure. Using SEMs with 200 grains in CPFE framework (to obtain the response for one fatigue cycle) takes more than twice the amount of time to simulate SEMs with 150 grains. Hence in order to reduce the computational time, while still being able to capture the scatter in fatigue lives to a reasonable level of accuracy, we use SEMs with at least 150 grains (which captures the microstructure attributes and strength properties), in order to obtain fatigue life distribution and link variability in microstructure to fatigue scatter.

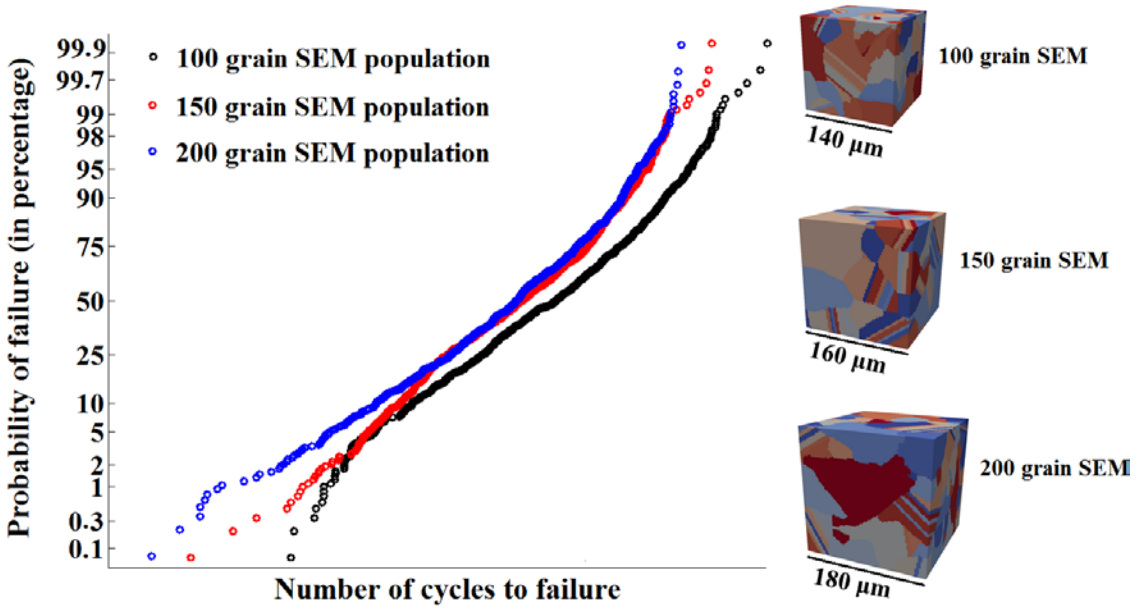

Fig. 3.11. Effect of the size of an SEM on the fatigue life distribution curve. Three SEMs, each taken from three different populations of SEMs, are shown in the inlets.

After determining that each SEM needs to have at least 150 grains, we probe the PSB model through 15 unique SEMs and obtain the fatigue life of the hot-spot grain (the one with the least number of cycles to crack initiation) from each SEM. Hence, we associate each unique SEM with one unique fatigue life data point and obtain 15 fatigue life predictions from 15 independent SEMs. The fatigue life predictions, thus obtained, are overlaid on a 95% confidence interval plot generated from experimental fatigue life data, shown using a log-log plot in Fig. 3.12. The scatter in the fatigue life predictions obtained (by varying the microstructure) is in good agreement with the scatter observed in experimental fatigue life data. The heterogeneous deformation state of the local microstructure of a hot-spot provides insights about what caused failure at those specific locations. As discussed earlier, the influence of elastic anisotropy and plastic strain

accumulation at the hot-spots provides an explanation into the underpinning mechanism of crack nucleation.

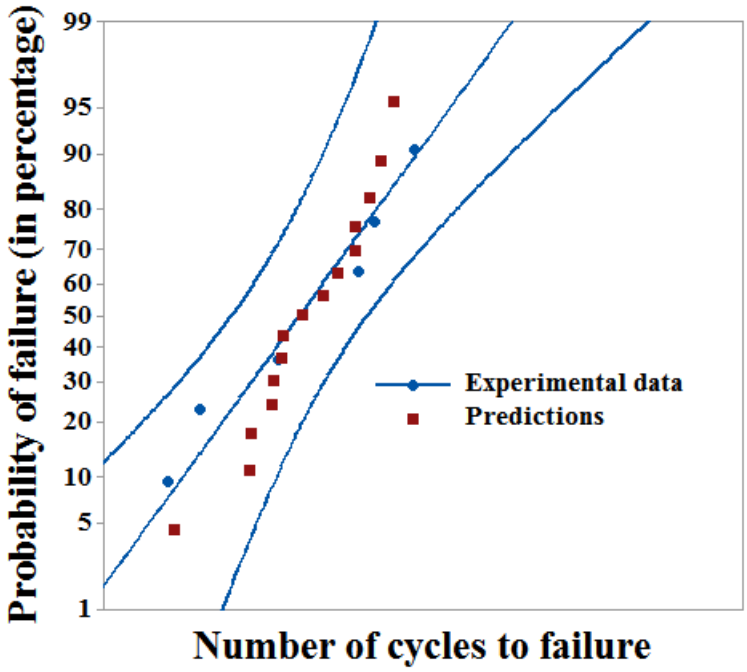

Fig. 3.12. Fatigue life predictions obtained by considering fatigue lives of the hot-spot grains (those with the least fatigue lives compared to all other grains) in 15 different SEMs. Predictions from the model are overlaid on the 95% confidence interval plot generated from experimental data.

Lattice incompatibility develops near GBs as a result of geometric differences in slip system alignment between two neighbors of distinctly different grain orientation. Stress concentrations develop at GBs with high lattice incompatibility. Hence the amount of incompatible stresses can be understood by quantifying lattice incompatibility. For this purpose, we note a tensorial parameter, which by itself cannot describe compatible deformation. The deformation gradient, $F=F^eF^p$ [124], can define compatible

deformation, which is not fulfilled by F^e or F^p alone. Acharya and Beaudoin [137] used F^{e-1} to measure incompatibility as follows:

$$\Lambda := \left(F^{e-1}_{ij,k} - F^{e-1}_{ik,j}\right) e_i \otimes e_j \otimes e_k, \tag{3.29}$$

where $\{e_i\}$ is the basis of a rectangular Cartesian coordinate system. As the lattice incompatibility developed at the GBs gives rise to incompatible stresses, we treat the incompatibility, Λ_{eq}, as an equivalent stress metric to study the high elastic stress anisotropy (ESA) at the GBs as follows:

$$\Lambda_{eq} = \left(\frac{3}{2}\Lambda : \Lambda\right)^{\frac{1}{2}}. \tag{3.30}$$

As previously discussed, crack initiation follows strain localization. Crystal plasticity framework enables us to quantitatively understand the microstructure dependent evolution of the plastic strain. Effective plastic strain accumulation (PSA), p, [138] at a material point has been used, in order to study the strain localization in the hot-spots predicted by the PSB model. It is calculated from the plastic velocity gradient (L_p) as follows:

$$L_p = \dot{\gamma}^{\alpha}(s^{\alpha} \otimes m^{\alpha}), \tag{3.31}$$

$$\dot{p} = \left(\frac{2}{3} L_p : L_p\right)^{\frac{1}{2}}, \tag{3.32}$$

$$p = \int_0^t \dot{p}\, dt\,, \tag{3.33}$$

where $\dot{\gamma}^{\alpha}$, s^{α} and m^{α} are the rate of slip, slip direction and the slip plane normal of the slip system α, respectively.

As a visual example, for the three hot-spots that display the lowest lives (in three different SEMs) based on the PSB model's predictions, the elastic anisotropy (Λ_{eq}) and

plastic strain accumulation (p) were plotted over all the material points within the respective SEMs (Fig. 3.13) at maximum applied macroscopic strain (or at the end of the one fatigue cycle simulated in CPFE). In addition to those two metrics, the absolute RSS values of that slip system containing the PSB is also plotted. For example, if the PSB formed on slip system 6 within the hot-spot grain (or grain cluster), then the absolute RSS values of slip system 6 at all material points in the SEM are plotted for mere comparison purposes. In order to visualize the PSB alignment, the local anisotropy, and strain accumulation, a plane section is cut through the hot-spot grain along the slip plane containing the PSB and is extended through the SEM. First row in Fig. 3.13, show the elastic anisotropy, plastic strain accumulation, and the RSS plotted over the cross- section of an SEM containing hot-spot 1, second row in Fig. 3.13, show the plots of the three aforementioned metrics over the cut section of an SEM containing hot-spot 2 and similarly third row in Fig. 3.13, show the plots of the same metrics over the cross-section of a SEM containing hot-spot 3. In all the figures, the PSB slip system is shown with a black line superimposed on the microstructure for clarity. It can be clearly seen that in all the three hot-spots, cracks are predicted to initiate where the PSB is interacting with the TB. Hot-spots 1 and 2 correspond to a PSB forming in a single grain, whereas hot-spot 3 corresponds to a cluster of two grains sharing an LAGB. Further, it can be clearly seen from all the three hot-spots that the PSB model predicts that cracks initiate at a TB embedded in a relatively large grain/ grain clusters compared to small grains, which is in agreement with experiments [11,74,75,104].

It can be seen from the ESA plots (shown in the first column of Fig. 3.13), that the value of the ESA is highest at the GBs, and the TBs, in particular, show high degree of

anisotropy. The orientations of all the material points within each grain of the SEM are assigned the same values, hence it is an idealization compared to real materials that display intergranular misorientations and residual stresses. Due to this reason, the elastic anisotropy results are observed to be high only at the GBs and have near zero values away from the GB in the core of the grain. But if we were to model grains with internal rotations with high resolution meshes, the ESA of the slip bands can also be observed at the expense of computational time. The PSA however seems to accumulate at the GBs and also varies across the grains.

In all the hot-spots displayed, ESA, PSA, and RSS have high values, which are partially attributed to a high probability for crack initiation at these material points. High elastic anisotropies can be clearly observed in the vicinity of twins. In addition to that, since TBs are the strongest barriers to slip transmission, dislocations pile-up at TBs [23,86]. In other words, high lattice incompatibility at TBs and the long-range stress field created by dislocation pile-ups at the TBs, can potentially increase the stress concentrations and lead to crack initiations. This can be a partial explanation for the high probability of crack initiation at TBs as predicted by the PSB model.

Such a detailed analysis of the 3D heterogeneities (in elastic anisotropy and plastic strain accumulation) is only possible by the use of crystal plasticity. The use of CPFE also helped i) reduce the number of experimental evolution functions and fitting parameters used in the earlier version of the PSB energy balance for U720 [23,24,69] and ii) eliminate the use weakest link theory, by providing more information on the location specific heterogeneous deformation.

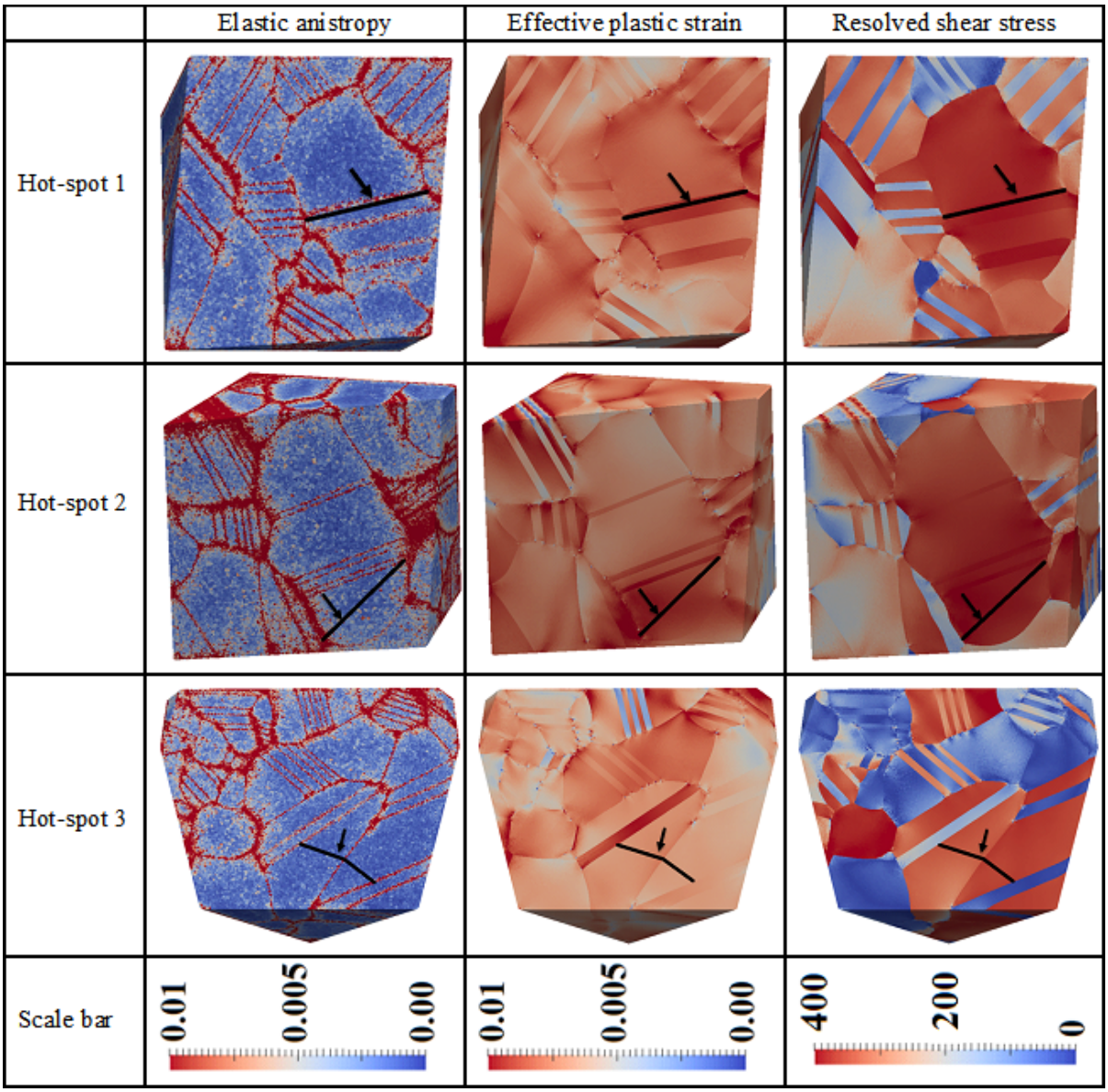

Figure 3.13. A cross-sectional plane through the hot-spots within a SEM to show ESA and PSA in the local neighborhood of the hot-spots. In all the plots, the plane passes through the centroid of the hot-spot (grain or cluster of grains) and its normal is parallel to the slip plane normal of the active slip system containing the PSB, shown with a black line and indicated by an arrow. It must also be noted that RSS plots are created on the same slip system (at all material points) based on the slip system on which the PSB

formed in the hot-spot grain. Elastic anisotropy (Λ_{eq}) (units $\frac{1}{\mu m^2}$), Plastic strain accumulation (p), RSS (units MPa) are shown at hot-spot 1 (first row), hot-spot 2 (second row) and hot-spot 3 (third row), with the respective scale bars shown in the last row.

As relatively high values of both metrics (Λ_{eq} and p) are observed to occur at the GBs, average values of both the metrics are calculated at the GBs for every grain within an SEM. This information is linked with the fatigue lives calculated for all the grains. Based on this accumulated data, a response surface (shown in Fig. 3.14) is constructed. It can be clearly visualized that lower values for fatigue lives are observed for grains that have extreme values of ESA and PSA at the GBs.

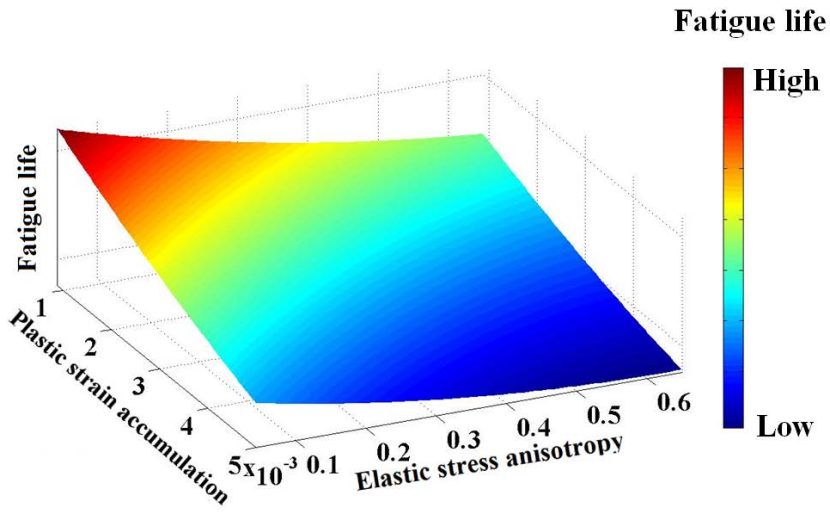

Fig. 3.14. Influence of ESA and PSA on fatigue life.

Critical life limiting parameters like ESA, PSA and maximum RSS are conditions that must be satisfied to identify certain microstructural features exhibiting a high probability of crack nucleation. Hence the evolution of these three parameters was calculated over 10 cycles of strain controlled loading (using a smaller SEM consisting of

100 grains, in order to save a significant amount of computational time in simulating 10 fatigue cycles, while still being able to study the evolution of life limiting parameters). Figure 3.15 shows the evolution of these parameters over cycles 1, 2, 5 and 10, with each plot taken at the maximum applied strain over the corresponding cycle. It can be observed that the lattice incompatibility remains consistent during the cyclic loading. The plastic strain accumulation on the other hand shows a clear positive trend in evolution, and it can be explained by the fact that LCF regime results in incremental plastic strain accumulation per cycle. At the microstructure level, this leads to more dislocation pile-ups at the GBs. From Fig. 3.15, annealing TBs accumulate high strains with an increase in cyclic loading. This observation provides insights as to why TBs are preferred locations for cracks to initiate. Maximum RSS calculated at every material point in the SEM also shows a similar incremental trend, which can be attributed to the increased hardening observed with cyclic loading. High values of maximum RSS observed at TBs are a result of high elastic anisotropy and strain accumulation.

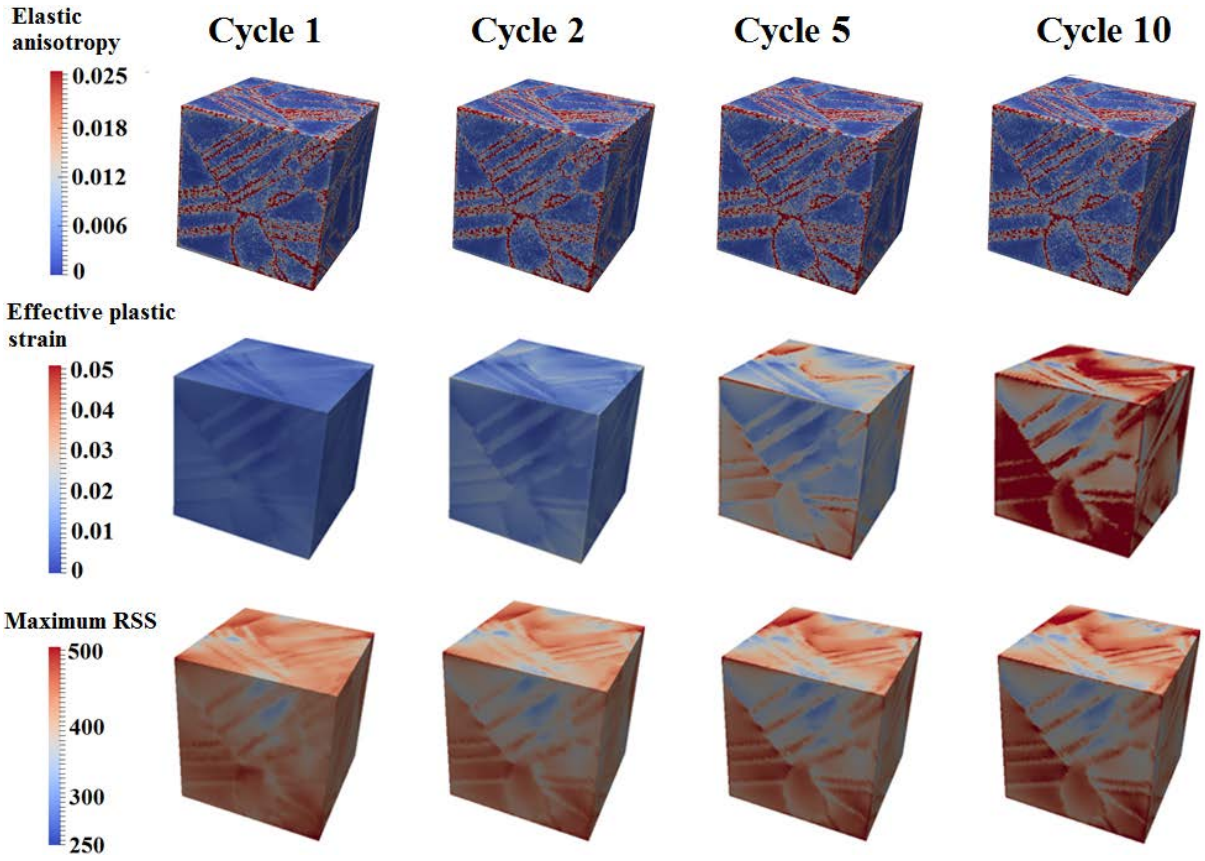

Figure 3.15. Evolution of elastic anisotropy (Λ_{eq}), plastic strain accumulation (p) and maximum resolved shear stress (calculated at every material point over 10 cycles).

While elastic stress anisotropy and plastic strain accumulation along with the RSS play an important role by acting in concert to initiate fatigue cracks, normal stress also has a significant role to play in the limiting fatigue life of the material. With this as a motivation, in classical fracture mechanics terms, the crack driving force can be promoted by either mode I initiation based on the normal tensile stress along the TB or mode II initiation based on the resolved shear stress along the TB. Due to the propensity of fatigue crack initiation in the vicinity of favorable oriented TBs with long slip traces, it is worthwhile to study the synergistic/competing role played by the RSS and the normal stress (acting on the TBs). For this purpose, we further analyze the stress state of hot-spot

1 (shown in the first row of Fig. 3.13), which is one of the twin lamellae (inside a large grain) encompassing a PSB. The values of the RSS (for the slip system corresponding to the PSB) and normal stress (acting perpendicular to the slip plane containing the PSB) are obtained at every integration point within the twin (at the peak applied macroscopic load), and their cumulative distributions are plotted (as shown in Fig. 3.16). Over a majority proportion of the volume within the twin, the normal stress was observed to dominate the RSS, which suggests a significant role played by the normal stress in *unzipping* a PSB at the intersection of the TB to act as a mode I crack.

Further, a cumulative distribution obtained by pooling together the absolute values of the RSS for all the 12 slip systems in the grain is compared to the RSS corresponding to PSB's slip system. A considerable amount of scatter is observed in the former, compared to the latter (which has a uniformly high RSS within the PSB). The same is not true in the case of normal stress, which has significantly higher values on certain locations of the grain, as shown in the inlets of Fig. 3.16. Thus, the highest value of normal stress is observed at the PSB-TB intersection, resulting in a normal tensile stress to open a crack along the TB.

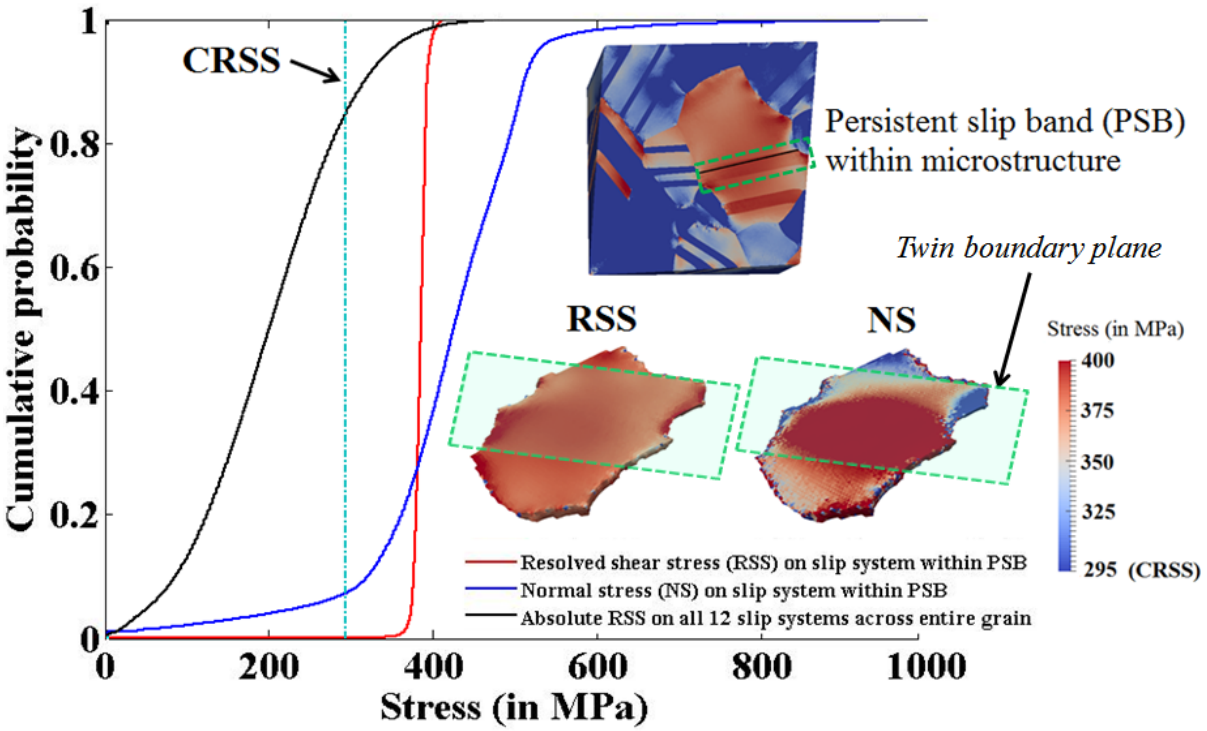

Figure 3.16. Cumulative probability distributions of the resolved shear stress (RSS) and normal stress (NS) at all integration points within the slip system of the critical PSB, along with the RSS values obtained for all slip systems across the entire grain. The critical resolved shear stress (CRSS) is shown as a reference value (with respect to slip system activation). The inlet figures show (top) an RSS plot on the cross-section view of the SEM and (bottom) contour plots of the RSS and NS values over the slip system corresponding to that of the PSB.

Due to strain controlled loading applied on the SEM with a constant strain range in every cycle (as shown in Fig. 3.17a), it was observed that the difference in strain accumulation between the fully loaded states of any two consecutive cycles remains almost the same (Fig. 3.17b). Although crystal plasticity accounts for cyclic hardening to an extent, it cannot capture the cyclic slip irreversibilities that arise from defect level

deformation mechanisms. Hence, crystal plasticity by itself is not sufficient to model fatigue and predict life. Due to a similar trend in the evolution of the stress/strain states with increasing number of cycles, we take the output from CPFE simulations over one fatigue cycle and leverage this data as input into the PSB model, which also considers slip irreversibilities.

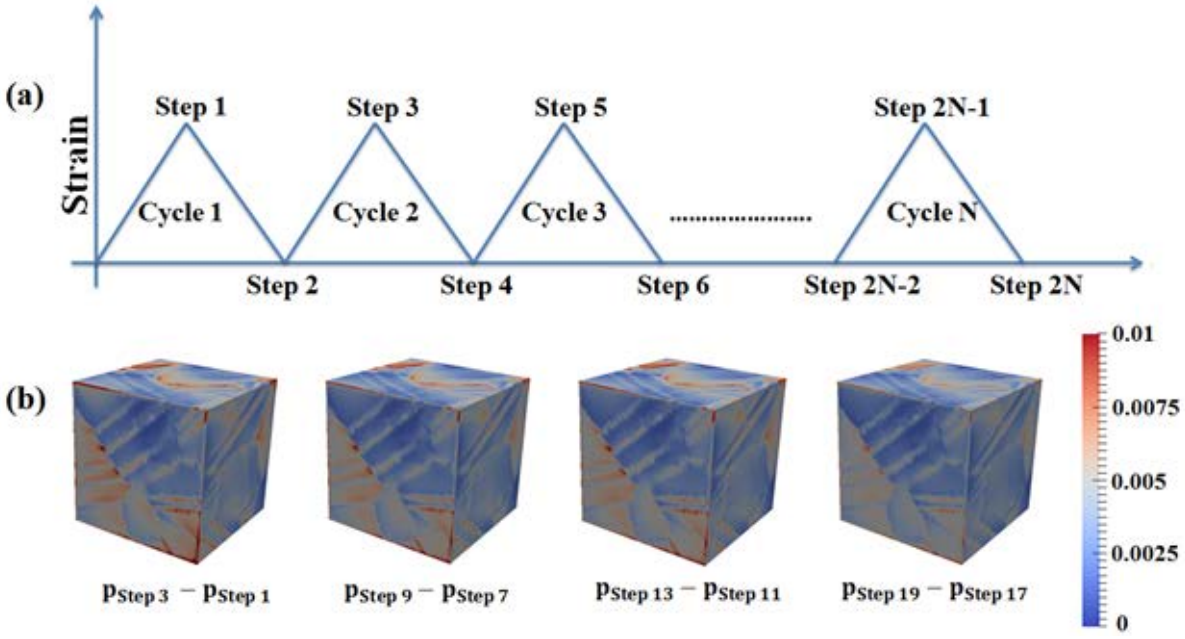

Figure 3.17. (a) A strain loading schematic showing the nomenclature of 'steps' and 'cycles' used in the discussion. (b) The difference of effective accumulated plastic strain (p) evaluated at the two consecutive loaded steps, $p_{step\ 2N-1}$ and $p_{step\ 2N-3}$ corresponding to cycles N and N-1 respectively.

Slip in cyclic loading is distinguished from that of monotonic loading. During forward and reverse loading, the material undergoes irreversible slip, which leads to distinct defect structures [31-33]. To date, the majority of the computational fatigue models attempt to use the same tools to model cyclic and monotonic loading, albeit these

models exhibit limited success since they cannot capture the complex and unique features of the fatigue phenomena. Various forms of cyclic slip irreversibilities manifests during cyclic loading in polycrystalline materials and their contributions to the fatigue damage evolution is inherent within the present fatigue model. Cyclic slip irreversibilities are the fraction of plastic shear strain that is microstructurally irreversible [45]. These irreversibilities can occur both on the surface and in the bulk of the material [34]. Irreversibilities on the surface cause roughness, due to accumulation of slip steps. In the bulk of the material irreversibilities occur due to i) dislocations becoming sessile due to the formation of locks that impede subsequent dislocation glide, ii) annihilation of positive and negative dislocations, iii) slip-GB interaction which leaves a residual Burgers vector within the GB causing extrusions to grow with repeated loading, iv) shearing of the precipitate, and v) dislocation climb at high temperatures [34,35,47]. These defect level mechanisms can be accounted for, by calculating the activation energy required for each process to occur. Since the current fatigue model is an energy-based model, the energies for pertinent dislocation mechanisms contributing towards irreversibilities are calculated, specifically shearing of precipitates, formation of unique dislocation arrangements within PSBs, and development of extrusions/intrusions at GBs.

In nickel-base superalloys, a prominent deformation mechanism at intermediate temperatures is through the shearing of the precipitates. Due to intense cyclic slip localization in the PSBs, dislocations are able to shear through the precipitates. The ease at which the precipitates can be sheared depends on the shear stress, normal stress, work-hardening, and temperature. For instance, as depicted in Fig. 3.6, a tensile normal strain acting on atomic slip planes will increase the distance between the slip planes which in

turn makes it easier for slip to occur thereby reducing the SFE (or APBE) and vice versa. The shearing through precipitate (and matrix), with its dependence on normal strain was taken into consideration using APBE (and SFE) energies obtained from MD simulations (as shown in Fig. 3.7a and 3.7b). The irreversible flow through precipitate (and matrix) shearing, with its dependence on normal stress was taken into consideration using APBE (and SFE) energies obtained from MD simulations. Moreover, the energy balance is built for a PSB, which develops unique dislocation arrangements, including dislocation dipoles, as a form of slip irreversibilities. Another contribution to irreversible plastic flow comes from the formation of extrusions from PSB impingement on a HAGB. These extrusions grow in length during cyclic loading due to an increased number of residual dislocations accumulating within the GB [116]. The model takes into consideration the development of extrusions and the associated energy required to form the extrusion [86]. Thus, the cyclic slip irreversibilities due to fatigue are considered into the model by considering the energies required for the fatigue related defect level mechanisms that introduce irreversible plastic flow in the material. The underpinning physics improves the fidelity of the model in investigating the microstructure's role in fatigue crack initiation and also helps link fatigue scatter to variability in the microstructure by sampling many statistical equivalent realizations of defect-microstructure interactions.

3.7 Summary

In the current research work, a microstructure based fatigue life prediction framework is developed, which takes into account i) the statistics of the material’s microstructure, ii) quantitative input from the complex 3D stress and strain heterogeneities output from crystal plasticity finite element (CPFE) simulations and iii)

grain boundary (GB) energies calculated from molecular dynamics (MD) simulations to differentiate the role of the GB character. The following conclusions can be made with regards to the current research effort.

- A microstructure and deformation mechanism based formulation is used to define the energy of a persistent slip band (PSB), using the quantitative information obtained from i) continuum scale CPFE simulations which solve for complex 3D stress and strain heterogeneities within the microstructures and ii) atomistic scale MD simulations which provide energies of various types of GBs and defect level mechanisms.
- The significant effect of the normal stress on fatigue life is incorporated into the model by calculating its relationship with the APBE and SFE energies, which contribute to the energy of a PSB.
- The fatigue framework predicts crack initiation to occur at a twin boundary (TB) embedded in a large grain, which is in agreement with experimental observations.
- A high concentration of elastic stress anisotropy and accumulated plastic strain is observed in the immediate vicinity of the TBs where cracks were predicted to initiate.
- Significant normal stress was observed to act on a favorably oriented twin (embedded in a large grain) where cracks were predicted to initiate, such high normal stresses act as crack driving forces.
- Scatter in fatigue life is linked to the microstructure variability, which is simulated by generating multiple statistically equivalent microstructures (with

explicitly inserted annealing twins), based on statistics obtained from the real microstructure of the material.

- Fatigue life predictions obtained are in good agreement with experimental data.

4. SENSITIVTY AND UNCERTAINITY ANALYSIS

4.1 Uncertainties in the Model

The presence of uncertainties in a computational model can be attributed to many factors including but not limited to: i) measurement errors, ii) numerical errors, iii) missing physics due to simplifying assumptions, etc. Input parameters present in the current model can be categorized into three classes based on the ease of measurability using experiments i) physical parameters that can be calculated using experiments, ii) physical parameters that cannot be measured using experiments, and iii) parameters that are empirical/semi-empirical in nature, and hence cannot be measured using experiments. In addition to the aforementioned uncertainties, model discrepancy (or model bias) exists due to epistemic uncertainties present in the model.

4.1.1 Physical Parameters that can be Calculated Using Experiments

These physical parameters correspond to a distribution of values due to variation in the experimentally measured values. Uncertainties observed in these parameters are possibly due to measurement errors, material variability, sampling volume, or usage of various data collection techniques. The set of model parameters (within the fatigue model discussed in Section 3.3) that fit into this category of uncertainties are Young's modulus (E), Poisson's ratio (ν), γ' volume fraction (f), dislocation density (ρ) within a PSB, and PSB width (h). Although the measurement of E and ν are straight forward using

mechanical testing equipment in a lab, the measurement of the rest of the parameters (f, ρ, h), which correspond to a lower length-scale, require advanced experimental setup, for instance the usage of neutron diffraction experiments for measuring dislocation density (ρ) or the usage transmission electron microscope to measure the width of a PSB (h). Due to this reason, a distribution was assigned to each of these input parameters based on literature review and expert opinion. While performing GSA (as discussed in Section 4.2), the influence of all parameters on the uncertainty of output is calculated, using sensitivity indices and global sensitivity plots. Table 4.1 summarizes the distribution assigned to each of the parameters, and also the source from where the data was obtained.

4.1.2 Physical Parameters that cannot be Easily Measured Using Experiments

Some of the physical parameters in the model, like the stacking fault energy (γ_{SFE}), anti-phase boundary energy (γ_{APBE}), energy required for a dislocation to transmit across a GB ($\mathrm{E}_{\mathrm{slip-GB}}^{\gamma-\mathrm{MD}}$) cannot be easily measured using experiments. Although, the intrinsic stacking fault energy can be calculated by measuring the distance between Shockley partials under a transmission electron microscope, unstable stacking fault energy strictly cannot be measured directly from experiments. Additionally, the fatigue model considered in the current study takes into account, the effect of normal stress ($\sigma_{\mathrm{N}}^{\alpha}$) on the energy of the PSB and hence it requires the quantitative dependence of γ_{SFE} and γ_{APBE} on the normal stress acting upon the PSB. These quantities can be obtained using MD simulations. The potentials used to measure γ_{SFE}, γ_{APBE} and $\mathrm{E}_{\mathrm{slip-GB}}^{\gamma-\mathrm{MD}}$ are still empirical in nature, hence there is some degree of uncertainty involved with the calculations obtained from these simulations [94,95]. A Gaussian distribution is assigned

to two parameters, γ_{SFE} and γ_{APBE}, with the mean as the calculated value and a standard deviation equal to 5% of the calculated value.

GBs have a definitive role in localizing and accumulating strain [139], which is a forerunner to crack initiation. The fatigue framework employs additional information about the interactions between dislocations and specific GB characters, with the value of $\mathrm{E}_{\mathrm{slip-GB}}^{\gamma-\mathrm{MD}}$. Slip-GB interactions are very complex and span an infinite parameter space, so certain simplifying assumptions are made within the model; specifically, conservative values of the energy barrier for slip-GB interaction is taken by not accounting for shear stress on the GB plane. In order to quantify the uncertainty in the values of $\mathrm{E}_{\mathrm{slip-GB}}^{\gamma-\mathrm{MD}}$, we consider an example of a slip-TB interaction for various twin orientations and dislocation types. Specifically, from the work of Ezaz et al. [140], MD simulations are used to quantify dislocation transmission and incorporation at a coherent twin boundary (CTB) in six different classes of slip-twin reactions. The energy barrier for dislocation transmission through CTB was observed to be proportional to the magnitude of the residual Burgers vector within the CTB after the transmission event [141]. Burgers vector increased from 0 (due to pure cross-slip of a screw dislocation) to 0.53a (with a being the lattice parameter), the energy barrier increased by approximately 24%, from 187 mJ/m^2 to 232 mJ/m^2. With the 24% deviation in $\mathrm{E}_{\mathrm{slip-GB}}^{\gamma-\mathrm{MD}}$ taken as the uncertainty for all types of slip-GB interactions, a log-normal distribution is used to quantify uncertainty in the values of the GB energy barriers to slip.

The values of these parameters (γ_{SFE}, γ_{APBE} and $\mathrm{E}_{\mathrm{slip-GB}}^{\gamma-\mathrm{MD}}$) are sampled from the assigned distributions to see the propagation of uncertainty through the model and its

effect on fatigue life predictions. This will help in assessing the sensitivity of these parameters in fatigue life predictions.

4.1.3 Parameters that are Empirical/Semi-Empirical in Nature

Some parameters in the model are empirical / semi-empirical in nature. For instance, the first parameter in this category is the degree of crystallinity (DC) within a PSB. The physical meaning for this parameter is associated with the construction of the PSB energy balance, which sums the contribution of individual dislocations within the PSB. As more dislocations are added, the entropy within the PSB increases and the degree of crystallinity decreases. Physically this parameter is associated with the latent heat of fusion for the material. This parameter decreases with increasing number of cycles as the dislocation density increases. The DC parameter can take values from 0 to 1, with 1 referring to a perfect crystal and values approaching 0 are analogous to the latent heat of fusion. Hence a uniform distribution is assigned to this parameter, with 0 and 1 as the lower and upper bounds of the distribution.

The second parameter is the proportionality constant, *k*, in Eq. (3.19), which is used to calculate the number of dislocations forming an extrusion at the PSB-GB intersection, n_{ext-GB}^{dis}. The PSB model shows an inverse correlation between extrusion height and fatigue life, the detailed aspect of which is discussed in Section 5.2. The value of n_{ext-GB}^{dis}, and hence the extrusion height at the PSB-GB intersection scales with the value of *k*. Measurement of extrusion height within the bulk of the material is not a trivial task, and this leads to uncertainty in the parameter, which can be accounted using *k*. Hence, *k* accounts for the uncertainties arising due to missing physics and the simplifying

assumptions that went into defining a stress based empirical expression for calculating n_{ext-GB}^{dis} (Eq. 3.19). Since n_{ext-GB}^{dis} is a strictly positive quantity, so is *k*. Therefore, a uniform distribution, $\tilde{U}(0,\infty)$ is assigned to *k*.

4.1.4 Model Discrepancy and Error in Experimental Data

In addition to the uncertainty caused by the aforementioned parameters, epistemic uncertainties occur in the model due to some simplifying assumptions. For instance, the PSB model assumes that PSBs exist on all active slip systems within grains (or grain clusters) within the microstructure, thereby not accounting for the number of cycles required to form PSBs. In order to address the bias created due to such assumptions, we introduce a model discrepancy (or model bias) term, δ. This can be viewed as a model error in predicting fatigue lives for a given microstructure at a given strain amplitude.

Most importantly, the scatter observed in the fatigue lives (at a particular strain amplitude) can be partly attributed to the variability in the microstructure of the material [22-25,69]. In addition to the inherent microstructure dependent variability, errors may occur while taking the values from experiments due to equipment alignment, data acquisition tolerances, variability in specimen machining, etc. For instance, the exact determination of when an internal fatigue crack has initiated is not possible. Due to this reason, an experimentalist relies on a percentage drop in load to define number of cycles to crack initiation within a strain controlled fatigue experiment [142]. In this context, the criteria adopted to decide crack initiation life is more phenomenological in nature and hence accounts for errors. Such measurement errors in experiments are accounted for, by introducing a measurement error term, e.

If $y(x_i)$ represents the fatigue lives obtained from experiments, and $f(x_i,\boldsymbol{\theta})$ represents the fatigue life predictions from the model, they can be related by the following simple equation:

$$y(x_i) = f(x_i, \boldsymbol{\theta}) + \delta(x_i) + e \tag{4.1}$$

where x_i are experimental conditions (or design parameters) that can be controlled by an experimentalist. For instance, x_i can be the applied strain amplitude ($\Delta\varepsilon$), temperature or R-ratio. The value of $\boldsymbol{\theta}$, represents the model parameters which cannot be directly controlled or sometimes cannot even be directly observed by the person conducting the experiment [143]. All ten parameters discussed in Section 4.1 comprise the $\boldsymbol{\theta}$ vector. In the current model, $\boldsymbol{\theta}$ depends on how the material responds to an applied fatigue load based on the local microstructure features. Due to fundamental difference between x_i and $\boldsymbol{\theta}$, and the fact that $\boldsymbol{\theta}$ cannot be controlled (and in some cases cannot be measured) during experiments, we take the model discrepancy to only depend on the experimental conditions (or design parameters), x_i [27,143]. Assuming that the model discrepancies, $\delta(x_i)$, are independently and identically distributed, a zero mean Gaussian random distribution with variance, σ_1, represented as $\widetilde{N}(0, \sigma_1^2)$, is assigned to $\delta(x_i)$. A similar argument is applied to experimental error term, e, which can also be assigned a Gaussian distribution $\widetilde{N}(0, \sigma_2^2)$. Since the summation of two Gaussian distributions is also a Gaussian distribution, we replace the two Gaussian distributions with just one Gaussian, $\widetilde{N}(0, \sigma^2)$. Hence, with the addition of σ into the parameter estimation problem, we now have a new augmented parameter set, $\boldsymbol{\varphi}$, given by $\{\boldsymbol{\theta}, \sigma\}$ or $\left\{E, \nu, f, \rho, h, \gamma_{SFE}, \gamma_{APBE}, E_{slip-GB}^{\gamma-MD}, DC, k, \sigma\right\}$. Since there is no information available about

the standard deviation, σ, it is an unknown hyper-parameter that needs to be inferred using the Bayesian framework. Due to lack of any information for this parameter and based on the fact that can only take positive values, a uniform prior distribution, $\widetilde{U}(0,\infty)$, is assigned to this parameter**.**

Table 4.1 List of model input parameters and distributions assigned to each of the parameter. Here $\widetilde{N}$ represents normal distribution, $\widetilde{LN}$ represents lognormal distribution, $\widetilde{U}$ represents uniform distribution and $\tilde{\beta}$ represents beta distribution.

Type	Parameter	Distribution	Units	References
Physical parameters	E	$\widetilde{N}(210,5)$	GPa	[144]
	ν	$\widetilde{N}(0.307,0.005)$	-	[144]
	f	$\widetilde{N}(0.4,0.03)$	-	[145,146]
	ρ	$\widetilde{LN}(\log(10^{15.8}),1)$	$\frac{1}{m^2}$	[147-149]
	h	$\widetilde{N}(200,50)$	nm	[40,45]
	γ_{SFE}	$\widetilde{N}(128,6.4)$	$\frac{mJ}{m^2}$	[23,24]
	γ_{APBE}	$\widetilde{N}(260,13)$	$\frac{mJ}{m^2}$	[145]
	$E_{slip-GB}^{\gamma-MD}$	$\widetilde{LN}(\log(2.0*10^{12}), 0.1)$	$\frac{mJ}{m^3}$	[139,141]
Empirical/ Semi-empirical parameters	DC	$\widetilde{U}(0,1)$	-	-
	k	$\widetilde{U}(0, \infty)$	-	-

Table 4.1 continued

Model discrepancy hyper-parameter	σ	$\tilde{U}(0, \infty)$		

4.2 Parameter Selection Using Global Sensitivity Analysis

Generally, in computational models, different input parameters will have varying degree of influence on the uncertainty of the model output. Moreover, a higher parameter dimension will increase the computational cost of uncertainty analysis. Hence, parameter selection technique is applied to isolate the most influential parameters in the model [26]. This is done using GSA, the objective of which is to ascertain how uncertainty in model outputs can be apportioned to uncertainties in model inputs, when considered over the entire range of input values [26,27]. The GSA focuses on the model parameters, $\boldsymbol{\theta}$. In other words, the hyper parameter, σ, is not considered, because given the extreme ranges in σ values; it can overshadow the sensitivities in the model parameters. This consideration is in agreement with the work of Chiachío et al. [101]. We consider σ in the uncertainty quantification problem along with other influential model parameters (determined using GSA). In other words, while doing sensitivity analysis, we ignore the combination of discrepancy and error terms (δ and e), in order to rank, just the model parameters with respect to their influence on the uncertainty of the output.

In this current work, we use variance based Sobol's sensitivity indices [27] to isolate the most influential model parameters. Additionally, graphical tools [150-152] are

also used to qualitatively understand the influence of various input parameters on the predicted fatigue life. Before using any of the graphical or numerical tools for GSA, Monte Carlo simulations are run, in which all input parameters are varied simultaneously, over their entire range (defined in Table 4.1) and the model output is generated.

4.2.1 Variance Based Sobol's Sensitivity Indices

The first-order effect of a parameter X_i, on the output (Y) is given by

$$S_i = \frac{V(E[Y/X_i])}{V(Y)} \tag{4.2}$$

where $E[Y/X_i]$ is the expectation of the output Y obtained by randomly changing all other parameters expect X_i. $V(E[Y/X_i])$ is the variance of the expectations obtained for several values of X_i.

For non-linear and non-additive models (like the model used in current work), the sum of all the first order sensitivity indices does not add to 1. This is due to the higher order effects in the model arising due to interaction amongst multiple parameters in the model. The second and third order sensitivity indices are given as follows:

$$S_{ij} = \frac{V\left(E\left[Y/X_i, X_j\right]\right)}{V(Y)} \tag{4.3}$$

$$S_{ijk} = \frac{V\left(E\left[Y/X_i, X_j, X_k\right]\right)}{V(Y)} \tag{4.4}$$

In a non-linear and non-additive model with *n* input parameters, there is a total of 2^n-1 sensitivity indices that need to be analyzed [27]. In the current model, there are 10 model parameters, resulting in a total of 1023 sensitivity indices. Analyzing such a high

number of indices is cumbersome. Hence, we use a different sensitivity measure called the total sensitivity index (S_{Ti}), given by:

$$S_{Ti} = \frac{E(V[Y/X_{\sim i}])}{V(Y)} \tag{4.5}$$

where $V[Y/X_{\sim i}]$ is the variance of the data obtained by considering random variations in X_i and by keeping all other parameters fixed. $E(V[Y/X_{\sim i}])$ is the mean of such variances obtained. The algorithm uses a double loop, in which the inner loop varies the parameter X_i randomly and obtains the variance for the output obtained, while the outer loop changes all other parameters except X_i and augments the variance obtained by the completion of the inner loop.

It is argued that a good, non-exhaustive characterization of sensitivity of a model with *n* input parameters is given by the total set of first order sensitivity indices, plus the total sensitivity indices, thereby needing 2n sensitivity indices rather than analyzing all 2^n-1 higher order sensitivity indices [27]. Hence, in this study we calculate only the first order (S_i) and total sensitivity indices (S_{Ti}) of all input parameters. From Table 4.2, it can be seen that four parameters {h, ρ, $E_{slip-GB}^{\gamma-MD}$, k} form the set of most influential parameters, as their total sensitivity indices are at least an order of magnitude higher compared to the sensitivity indices of other parameters $\{E, \nu, f, \gamma_{SFE}, \gamma_{APBE}, DC\}$.

Table 4.2 First order and total sensitivity indices of all input parameters in the model.

Input parameter	First order sensitivity index (S_i)	Total sensitivity index (S_{Ti})
Elastic modulus (E)	0.0046	0.0087
Poisson's ratio (ν)	0.0013	0.0024
γ' volume fraction (f)	0.0027	0.0046
Dislocation density (ρ)	0.1470	0.2413
PSB width (h)	0.1233	0.3057
SFE (γ_{SFE})	0.0017	0.0027
APBE (γ_{APBE})	0.0018	0.0026
Dislocation transmission energy at a GB ($E_{slip-GB}^{\gamma-MD}$)	0.1021	0.1334
Degree of crystallinity (DC)	0.0018	0.0046
Proportionality constant (k)	0.2761	0.3752

4.2.2 Graphical Tools for Global Sensitivity Analysis

Although scatter plots give us a rough idea of how an input parameter affects the output, they cannot be used to easily assess the importance of one parameter over the other. If the number of parameters that we are trying to analyze increase, scatter plots become cumbersome to analyze. Sensitivity indices (discussed in Section 4.2.1) are very efficient in inferring how the variance of the output Y can be quantitatively apportioned

to the uncertainty in different model inputs. However, by using those quantitative methods, no information is obtained regarding the reduction in the range of uncertainty of an influential input parameter (if possible), to obtain a target reduction in output variance [151]. Graphical tools maintain a rich set of information in addition to the sensitivity indices, as they estimate the contribution of a particular range of input parameter values on the sample mean [150] or sample variance [151] of the output quantity of interest.

In the current work, we use three such graphical plots [150-152]. Two among those plots are the contribution to sample mean (CSM) [150] and contribution to sample variance (CSV) [151], which are used to assess the influence of an input parameter on the sample mean or sample variance of the output, respectively. Based on the deviation of the CSM (or CSV) curve of a parameter X_j from the diagonal (e.g. straight line with slope of 1), its influence on the sample mean (or sample variance) of the output can be determined. The CSM and CSV plots for all variables in model parameters in the fatigue model are shown in Fig. 4.1a and 4.1b respectively. The third sensitivity plot used in this work is the cumulative sums of normalized reordered output (CUSUNORO) plot [152]. The further a parameter's CUSUNORO curve deviates from the X-axis, the greater is the influence of that parameter on the output. The CUSUNORO plot for the fatigue model is shown in Fig. 4.1c. It should be noted that all three graphical tools (CSM, CSV and CUSUNORO), are independent of the type of model (additive/non-additive/linear/non-linear) being used and just need the data generated using thousands of Monte Carlo simulations.

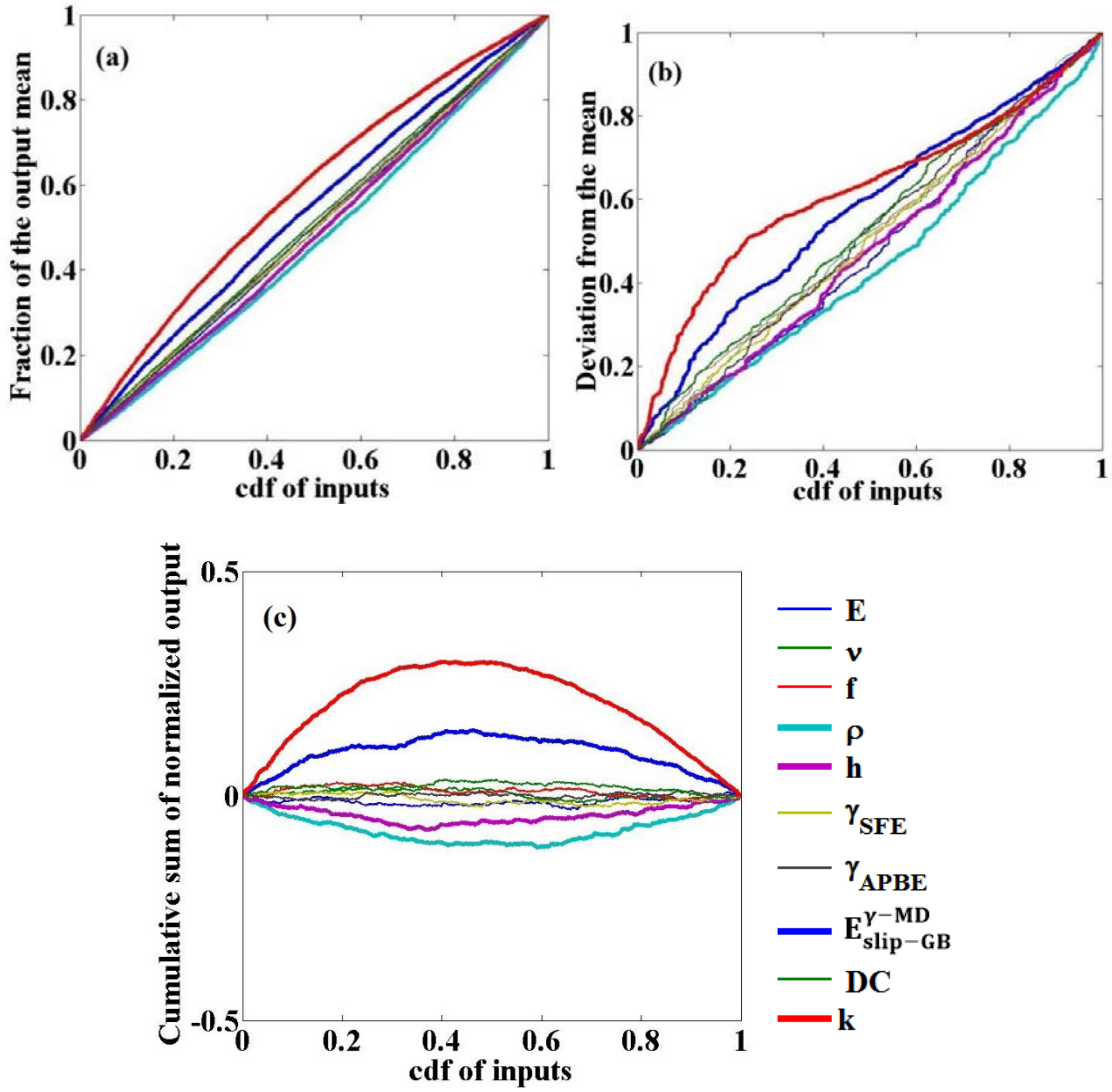

Figure 4.1. Graphical tools to qualitatively understand the influence of various parameters on the mean and variance of output. (a) CSM plot, (b) CSV plot, (c) CUSUNORO plot.

It can be inferred from the global sensitivity plots shown in Fig. 4.1, that the parameters $E_{slip-GB}^{\gamma-MD}$, k, ρ and h, significantly influence the output (fatigue life prediction), as these curves deviate from the diagonal (for CSM and CSV plots in Figs. 4.1a and 4.1b, respectively) and from the x-axis (for CUSUNORO plot in Fig. 4.1c). The curves of non-

influential parameters coincide (or are in close proximity) with the diagonal (for CSM and CSV plots) and the x-axis (for CUSUNORO plot), thus demonstrating little impact on the overall model output. The same trend is observed in the sensitivity indices (S_i and S_{Ti} as shown in Table 4.2), which show that the parameters $E_{slip-GB}^{\gamma-MD}$, k, ρ and h, have high sensitivity indices compared to the rest of the parameters. The efforts of the Bayesian inference will be directed towards quantifying the uncertainties in the set of influential parameters.

4.3 Uncertainty Quantification Using Bayesian Inference

We represent the most influential model parameters (along with the hyper-parameter σ) using a vector, $\boldsymbol{\alpha} = \{E_{slip-GB}^{\gamma-MD}, k, \rho, h, \sigma\}$ for use within the uncertainty quantification framework. The parameters that are considered relatively non-influential are still needed as the input to the model, and are assigned to their mean values of their respective prior distributions (shown in Table 4.1).

4.3.1 Bayesian Method

Bayesian inference technique is used in updating probabilities, and more generally, our current state of knowledge of parameters, $\boldsymbol{\alpha}$, using observed (or experimental) data, D. Updated probability distribution (posterior distribution), $\pi(\boldsymbol{\alpha}|D)$, can be obtained by applying Bayes theorem as follows:

$$\pi(\boldsymbol{\alpha}|D) = \frac{\pi(D|\boldsymbol{\alpha})\pi_0(\boldsymbol{\alpha})}{\pi(D)} \tag{4.6}$$

where $\pi_0(\boldsymbol{\alpha})$ represent our current state of knowledge or prior beliefs on parameter set $\boldsymbol{\alpha}$, $\pi(D|\boldsymbol{\alpha})$ represents the likelihood of observing the data D, given parameter realizations $\boldsymbol{\alpha}$ and $\pi(D)$ is the marginal density obtained by integrating the joint density $\pi(\boldsymbol{\alpha}, D)$ over all possible values of $\boldsymbol{\alpha}$. It can be treated as a normalization factor and this allows us to proportionally relate the prior, posterior and likelihood distributions as follows:

$$\pi(\boldsymbol{\alpha}|D) \propto \pi(D|\boldsymbol{\alpha})\pi_0(\boldsymbol{\alpha}) \tag{4.7}$$

The prior distributions of all parameters, $\pi_0(\boldsymbol{\alpha})$, are listed in Table 4.1. Using a statistical model shown in Eqn. (4.1), in which the model errors are assumed independently and identically distributed, the likelihood $\pi(D|\boldsymbol{\alpha})$ of observing the data follows a normal distribution [27,29]:

$$\pi(D|\boldsymbol{\alpha}) = \frac{1}{(2\pi\sigma^2)^{\frac{n}{2}}} e^{\sum_{i=1}^{n}\left(\frac{-(y_i - g(\alpha))^2}{2\sigma^2}\right)} \tag{4.8}$$

where σ is a hyper parameter in the likelihood distribution, which can be inferred using the fatigue life data $\{y_1, y_2, \ldots, y_n\}$ collected independently from testing n different specimens, and $g(\boldsymbol{\alpha})$ represents the prediction made by the model. Although the non-influential parameters are also used in the model, for brevity we just show the set $\boldsymbol{\alpha}$ (set of influential parameters) as it is those parameters that we are trying to estimate. The parameter estimation (or inverse Bayesian uncertainty quantification) problem in this study is to infer distributions of all parameters (in the set parameter $\boldsymbol{\alpha}$)**,** which makes predicted fatigue lives to be close to experimental fatigue life data, by using MCMC algorithm [153].

4.3.2 Markov Chain Monte Carlo Algorithm

MCMC simulation is a numerical technique, which uses Markov chains to explore the state space of model parameters and construct stationary posterior densities for model parameters based on observed data. MCMC uses the attributes of posterior densities (which are in turn dependent on the likelihood and prior) to specify parameter values that adequately explore the geometry of the distribution [27]. It is based on a simple idea of comparing the posterior densities of a candidate point (or a newly proposed point), $\boldsymbol{\alpha}^*$, with a current location in the state space $\boldsymbol{\alpha}$. If the candidate point yields a posterior density greater than the posterior density at the current location, then the proposed point is accepted with a probability of one, otherwise the candidate point is accepted with a probability of *r*, less than one. This can be explained by the fact that a higher posterior density implies less squared error between observed data and the evaluated QoI at the candidate point, and since such a point is always favored, we accept it with a probability of 1.

Mathematically, the ratio (*r*) between the posterior densities between the candidate point ($\boldsymbol{\alpha}$*) and the current point ($\boldsymbol{\alpha}$) can be represented as:

$$r = \frac{\pi(\boldsymbol{\alpha}^*|D)}{\pi(\boldsymbol{\alpha}|D)} = \frac{\pi(D|\boldsymbol{\alpha}^*)\pi_0(\boldsymbol{\alpha}^*)\pi(\boldsymbol{\alpha}|\boldsymbol{\alpha}^*)}{\pi(D|\boldsymbol{\alpha})\pi_0(\boldsymbol{\alpha})\pi(\boldsymbol{\alpha}^*|\boldsymbol{\alpha})} \tag{4.9}$$

The proposal (or jump) distribution, $\pi(\boldsymbol{\alpha}^*|\boldsymbol{\alpha})$ (used to propose a new candidate point, $\boldsymbol{\alpha}^*$), can be of symmetrical (Gaussian or uniform distribution) or non-symmetrical nature (log-normal or beta distribution). Symmetrical forms of proposal distributions are preferred to construct posterior densities, which most likely will have a symmetrical

geometry. But in general, posterior densities of some model parameters can have highly asymmetrical shapes, in which case using a symmetrical proposal distribution could lead to long convergence times. Therefore, in this work we use non-symmetrical proposal distributions which are a more generic case of sampling from any type of posterior densities and is the basis of the Metropolis-Hastings (M-H) algorithm [154].

The M-H algorithm can be implemented either by proposing a new state for all the parameters ($\boldsymbol{\alpha}$) at once in a 'block-wise' way (by choosing a proposal distribution which has number of dimensions equal to the number of parameters ($\boldsymbol{\alpha}$) we are trying to estimate) or by proposing each parameter α_i individually in a 'component-wise' way (by using a corresponding univariate proposal distribution assigned for each parameter). For block-wise sampling, depending on the number of dimensions and the type of parameters, an ideal n-dimensional proposal distribution, which takes care of all parameters at once, is difficult to identify. If the proposal distribution is not appropriate, a large number of the proposed sample will be rejected and hence takes a long time for convergence to be achieved. Due to the aforementioned reasons, we use component-wise sampling in the current work. A high level overview of the component-wise sampling using M-H algorithm is given below.

i) Set loop counter i = 0,

ii) Assign initial values to all the individual parameter in $\boldsymbol{\alpha} = \{\alpha_1, \alpha_2, \ldots \alpha_n\}$ by randomly sampling from their respective prior distributions, and

iii) Repeat the following steps until i = M (desired number of iterations).

Increment i by 1,

Repeat the following for each parameter, α_j, in parameter set $\boldsymbol{\alpha}$ =

$\{\alpha_1, \alpha_2, \ldots \alpha_n\}$, Generate a new candidate α_j^* from $\pi\left(\alpha_j^* | \alpha_j^{(t-1)}\right)$,

Calculate probability p= $\min\left(1, \frac{\pi\left(D|\alpha_j^*\right)\pi_0\left(\alpha_j^*\right)\pi(\alpha_j^{(t-1)}|\alpha_j^*)}{\pi\left(D|\alpha_j^{(t-1)}\right)\pi_0\left(\alpha_j^{(t-1)}\right)\pi\left(\alpha_j^*|\alpha_j^{(t-1)}\right)}\right)$,

Sample a random number u from $\widetilde{U}(0,1)$,

if u≤p, accept proposed state α_j^* and set $\alpha_j^t = \alpha_j^*$,

else, set $\alpha_j^t = \alpha_j^{(t-1)}$.

The convergence of the chain is monitored to ensure a stationary posterior distribution of parameters is obtained. We use a convergence test for which multiple Markov chains were run in parallel with different initial values of the parameters [98,155]. If the variances of a parameter (p) between n chains and within chains are represented as B_p and W_p, respectively, then an estimate of variance of p, V_p, can be represented as:

$$V_p = \frac{n-1}{n} W_p + \frac{1}{n} B_p \tag{4.10}$$

A convergence test statistic, R_p, can be calculated as:

$$R_p = \sqrt{\frac{V_p}{W_p}} \tag{4.11}$$

The value of R_p when calculated for each parameter should be close to unity to quantitatively ensure convergence. For the full form expressions of B_p and W_p, please refer to Cross et al. [98].

4.3.3 Marginal Posterior Densities of the Parameters

Multiple Markov chains are run with different initial guesses of the parameters, and posterior distributions are extracted after checking for convergence in each of the chains. The mean, variance, and the convergence test statistic (R_p) for the posterior distributions of all parameters are shown in Table 4.3. The posterior densities for the set of influential parameters (along with parameter σ) are shown in Fig. 4.2.

Table 4.3 Mean, variance, and convergence statistic of the posterior distributions of parameters.

Parameter (units)	Mean	Standard deviation	Convergence test statistic (R_p)
$E_{slip-GB}^{\gamma-MD}$ $(\frac{mJ}{m^3})$	2.2e12	0.13e12	1.003
k	1.673	0.185	1.021
ρ $(\frac{1}{m^2})$	8.68e15	1.48e15	1.010
h (nm)	191.03	24.05	1.040
σ	6534.46	2056.4	1.006

All the posterior distributions of the physical and semi-empirical parameters (like the transmission energy barrier, PSB width, dislocation density) are showing physically reasonable values as indicated in the literature. For instance, the PSB width (h) is close to the prior estimate and the typically observed widths of the PSBs are on the order of hundreds of nanometers [40,45]. Recall, a non-informative flat prior (which has minimal influence on the posterior distribution of parameters) was assigned to the parameters *k* and σ. The MCMC algorithm quantified the uncertainties pertaining to those parameters, which is evident from the unimodal distribution shown in Fig. 4.2d and 4.2e, respectively.

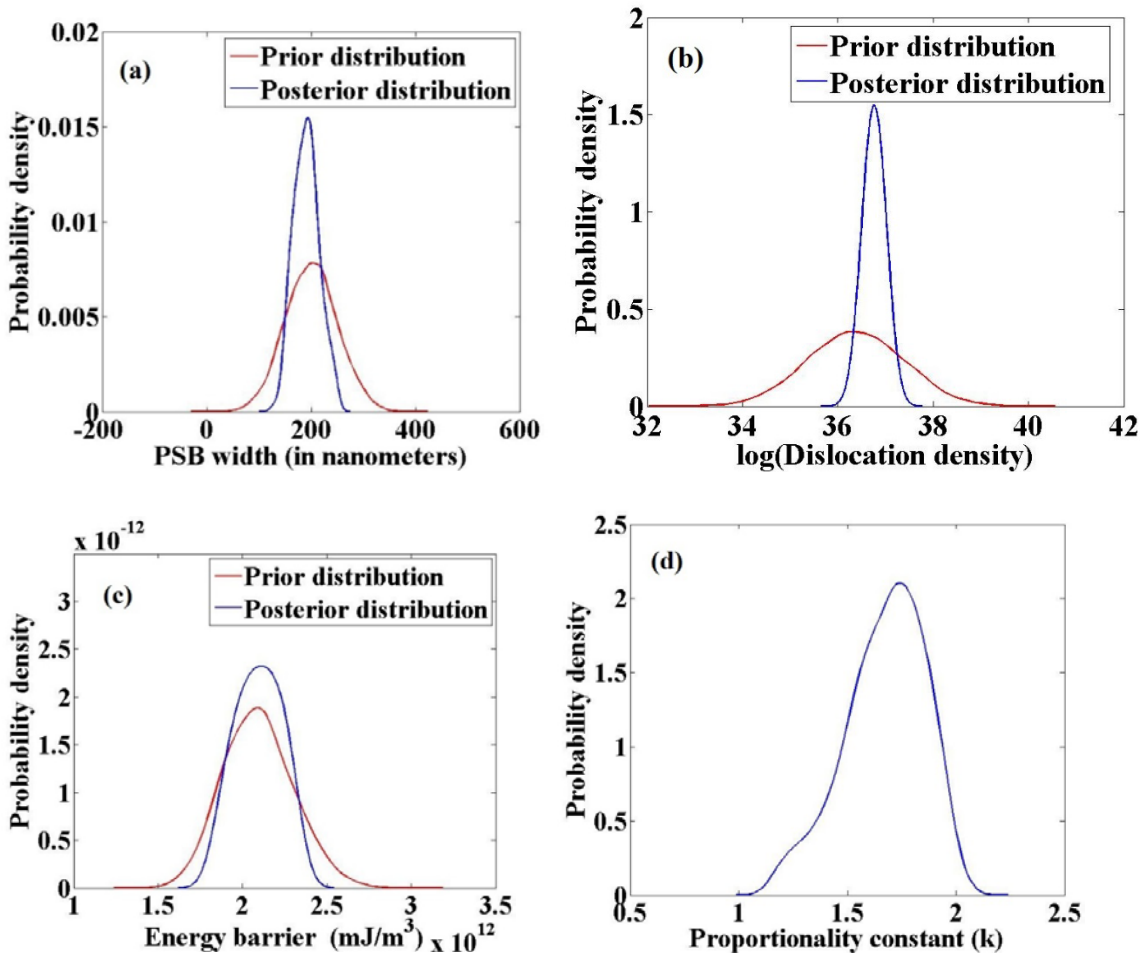

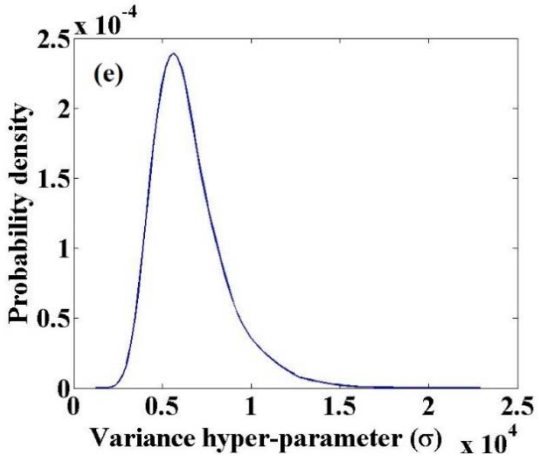

Figure 4.2. Prior and posterior densities of all parameters. It must be noted that the prior density for k and σ is, $\tilde{U}(0,\infty)$, and hence is coincident with the X-axis.

4.3.4 Constructing Full Posterior Distributions for All Parameters

Instead of using a single large RVE, which makes it computationally prohibitive to conduct CPFE simulations, we consider several SEMs, each of which encompasses a small volume compared to the RVE, but still are sufficiently large to capture the statistics of the microstructural attributes and the strength properties (elastic modulus, yield strength, strain hardening behavior and reverse plasticity upon unloading). In accordance with Niezgoda et al. [156], we treat an RVE as an ensemble of several SEMs, and construct the fatigue life distribution by pooling the distributions obtained by probing the fatigue model through individual SEMs. Similarly, we construct the full posterior distributions (representing the ensemble of all SEMs) for parameters, by pooling together the corresponding posterior densities obtained from the individual SEMs. Full posterior distribution for each parameter is constructed by combining multiple posterior distributions, as discussed by Miroshnikov et al. [157] and Neiswanger et al. [158].

Figure 4.3 shows five different posteriors (for each parameter, obtained by using five different SEMs) and also a full posterior distribution for each parameter.

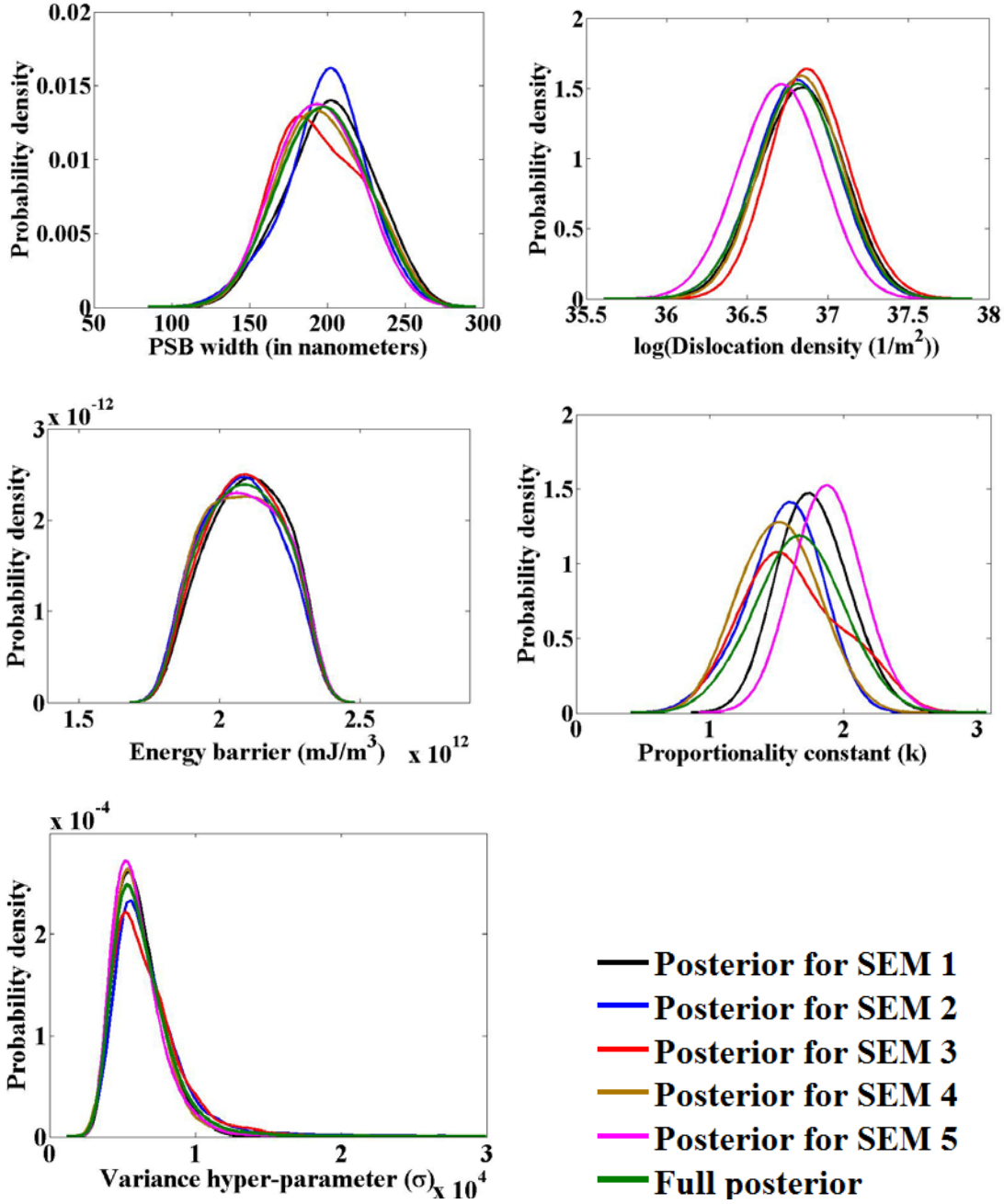

Figure 4.3. Plots showing the overlay of sub-posterior distributions of all the parameters obtained using five different SEMs, and also the full posterior distribution obtained from the sub-posterior distributions.

4.4 Uncertainty Propagation

The posterior distributions of uncertainties calculated using Bayesian inference are propagated through the model, in order to make robust fatigue life predictions. There are many techniques available to propagate uncertainties through a model, such as, i) sampling techniques, ii) perturbation methods, iii) spectral methods, etc., [27]. In this work we use Monte Carlo based sampling techniques due to their simplicity in implementation and the fact that the efficiency of these sampling techniques is independent of the number of parameters within the model. The model parameters are sampled from their respective full posterior distributions (shown in Section 4.3.4) and are fed into the PSB model to obtain fatigue life distributions for a population of multiple SEMs. For each Monte Carlo simulation, a value is assigned to each of the five parameters in $\boldsymbol{\alpha} = \{E_{slip-GB}^{\gamma-MD}, k, \rho, h, \sigma\}$ (generated using corresponding posterior distributions), and using this set of values for the parameters, the PSB model finds the hot-spot grain and its corresponding fatigue life (for each individual SEM). In summary, each Monte Carlo simulation for each SEM generates one data point. It must be noted that, while propagating uncertainties through the model for each SEM, the stress and strain attributes derived from CPFE simulations (that go into the PSB model) are kept the same. For validation purposes, the data generated from multiple Monte Carlo simulations was compared to the 95% confidence interval plots generated using experimental fatigue life data. The schematic of the methodology is shown in Fig. 4.4.

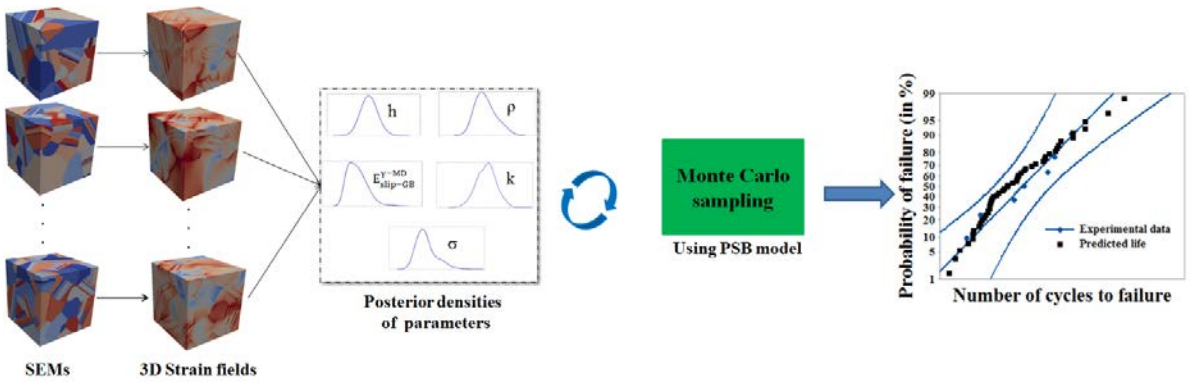

Figure 4.4. Schematic of uncertainty propagation using Monte Carlo sampling.

For the purpose of this study, five different SEMs were chosen and life predictions obtained for each of the five SEMs are shown in Fig. 4.5. Based on the convergence of mean and variance for the output QoI (fatigue life), it was determined that fifty Monte Carlo iterations were sufficient to obtain life predictions with equivalent mean and variance of a much larger sample of fatigue life predictions. Hence fifty Monte Carlo iterations were run for each of the five SEMs and fatigue life distributions were obtained for each SEM, individually. It can be seen from the log-log plot shown in Fig. 4.5 that the fatigue life predictions obtained using various SEMs lie within the 95% confidence interval bounds of the experimental fatigue life data. Given the quantified uncertainties, SEMs representing the microstructure of the material, along with the heterogeneous stress and strain data obtained from CPFE as inputs, the model is able to predict the life quite well. The calculated fatigue life predictions obtained by propagating the quantified uncertainties through the life prediction code shown in Fig. 4.5 is for a specific fatigue condition, e.g. a single applied strain range, an intermediate temperature, R-ratio, frequency, etc.

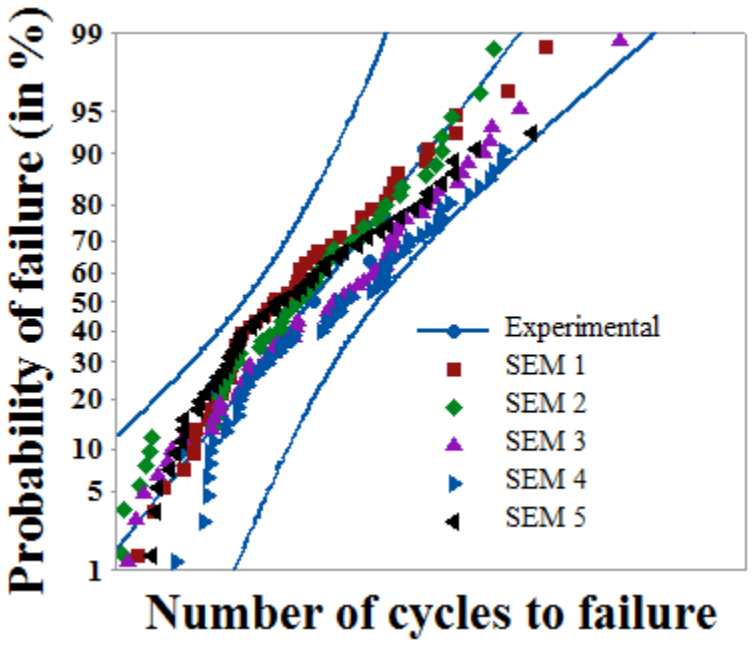

Figure 4.5. Comparisons of life predictions obtained for five different SEMs.

4.5 Dependency of Model Parameters on Applied Strain

Certain parameters involved in the life prediction model are not just material dependent, but also depend on the applied strain. Specifically, the model takes into consideration cyclic slip irreversibilities (please refer to Section 5.2 for more details), which are dependent on applied strain [56,159]. Cyclic slip irreversibilities manifest as extrusions when PSBs intersect with the surface or GBs. Experimental studies [36,50] quantified the dependence of the extrusion heights (and heights of slip steps formed on the surface) with the applied macroscopic strain. Mughrabi [56] provided a systematic review of studies done to quantify the cyclic slip irreversibilities (in both single crystals and polycrystals) and concluded that an inverse correlation exists between accumulated cyclic slip irreversibilities and fatigue lives. In the current model, the factor which scales the height of extrusion formed at PSB-GB intersection is *k*, which is also an influential

parameter in the model (as shown in Section 4.2). Hence, the dependence of the parameter *k*, on the applied strain is characterized, thus linking the extrusion height to the applied macroscopic strain.

For this purpose, the uncertainty in *k* is quantified at three different strain amplitudes of interest. Uncertainty quantification was done using the same procedure described in Section 4.3.2, by utilizing the experimental fatigue life data at the three strains. Only a single SEM is subjected to three different strain amplitudes, solely for the purpose of establishing the dependence of *k* on the applied strain. Figure 4.6a shows the posterior densities of *k* at three different strain amplitudes. It is evident from Fig. 4.6a that as the applied strain amplitude increases, the mean value of the posterior distribution of the scaling factor, *k*, also increases, indicating that the extrusions grow in size when the strain amplitude increases. This makes the model consistent with experimental observations [36,50].

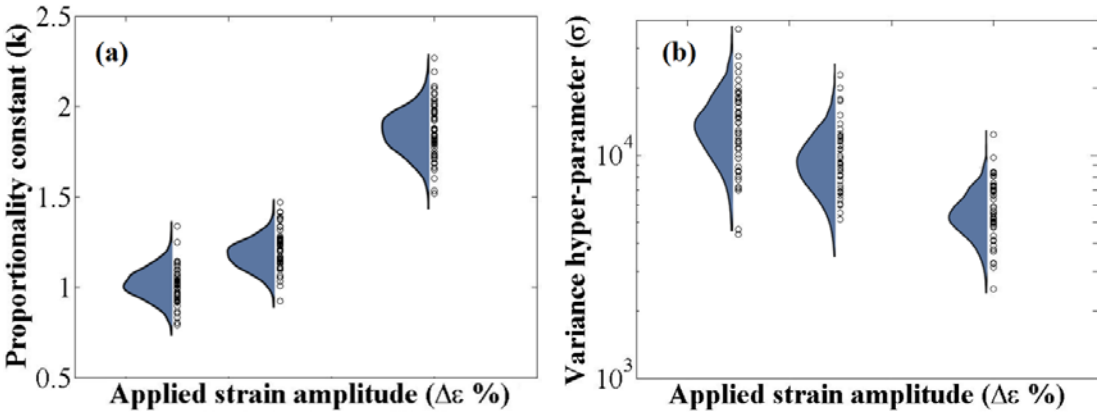

Figure 4.6. (a) The variation of proportionality constant term (k) and (b) hyper-parameter (σ) with applied strain.

In experiments conducted to characterize fatigue life at an applied strain amplitude, a distinct percentage of load drop is used as a measure to define number of cycles for crack initiation [142]. This manifests as experimental error, e, due to a fundamental difference between the predictions from the PSB model (number of cycles to fatigue crack initiation) and the experimental fatigue life data at hand (which is essentially a combination of number of cycles to crack initiation and additional cycles required for an initiated crack to incubate corresponding to a specific percentage of load drop). Since the crack driving forces increase with applied strain amplitude, we postulate that, e (and hence σ), is inherently dependent on the applied strain amplitude ($\Delta\varepsilon$). Hence, in order to establish a relation between the hyper parameter, σ, and applied strain amplitude ($\Delta\varepsilon$), we obtain posterior densities for σ at three different strain amplitudes of interest (as shown in Fig. 4.6b). The posterior density (of σ) corresponding to the highest applied strain amplitude has the lowest mean value, which can be attributed to the fact that the load drop percentage is achieved at a faster rate within the experiments conducted, due to the presence of larger crack driving forces. Similarly, it takes relatively more cycles to observe a distinct load drop in experiments conducted at lower applied strain amplitudes, and hence the posterior densities of σ, at lower strain amplitudes, have higher mean values.

Further, the quantified uncertainties in k and σ are propagated through the PSB model (using the uncertainty propagation methodology described in Section 4.4) at three different strain amplitudes ($\Delta\varepsilon_1, \Delta\varepsilon_2$ and $\Delta\varepsilon_3$), and fatigue life distributions are obtained. For the purpose of comparing fatigue life distributions at the three different strain

amplitudes, we only choose a single SEM and implement uncertainty propagation at the each of the three strain amplitudes of interest. Fatigue life predictions obtained at the three strain amplitudes are shown in Fig. 4.7. The life predictions obtained (by the PSB model) at the three strain amplitudes are in agreement with the limited experimental fatigue life data available at the three strain amplitudes, overlaid on the fatigue predictions shown in Fig. 4.7. For the strain amplitudes ($\Delta\varepsilon_2$ and $\Delta\varepsilon_3$), since only one experimental data point is available, a 50% probability of failure was assigned to that data point.

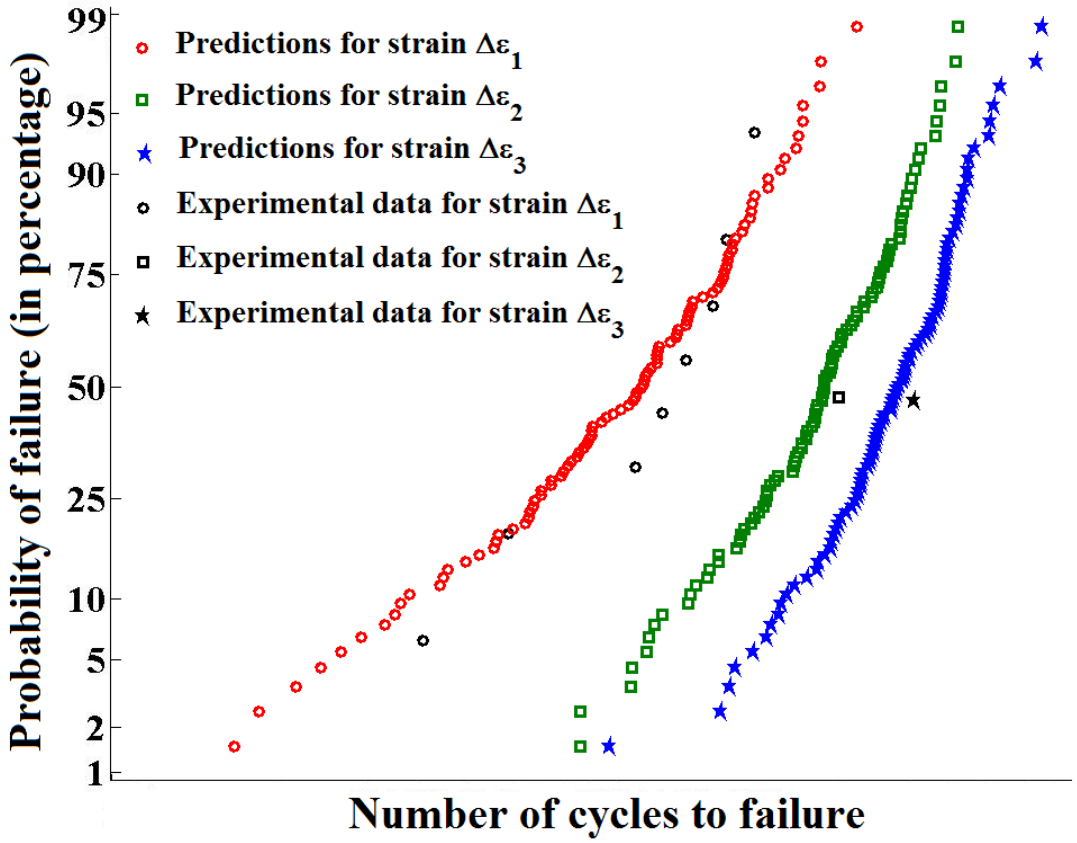

Figure 4.7. Strain-life plots at three different strain amplitudes ($\Delta\varepsilon_1 > \Delta\varepsilon_2 > \Delta\varepsilon_3$).

4.6 Summary

A microstructure based life prediction model, which uses the stability of a persistent slip band (PSB) as a criterion for fatigue crack initiation, is validated by using rigorous sensitivity and uncertainty analysis. Various types of uncertainties were identified in the model parameters based on the ease of their measurability using experiments i) physical parameters that can be calculated using experiments, ii) physical parameters that cannot be easily measured using experiments, iii) parameters that are empirical/semi-empirical in nature, and hence cannot be measured using experiments. Following parameter identification, GSA was used to identify the set of most influential parameters in the model, thereby reducing the dimensionality of the Bayesian uncertainty quantification framework. By using a component wise MCMC algorithm, which takes into consideration the experimental fatigue life data and the prior beliefs of the parameters, posterior densities of the uncertain parameters were obtained. Full posterior distributions were obtained for all parameters, by combining the posterior densities obtained using multiple SEMs. Uncertainty propagation was applied using a Monte Carlo framework, in which the uncertainties of the parameters from the full posterior distributions were propagated through the model, thereby calculating the life prediction in the presence of uncertainties. Life predictions obtained by using five different SEMs were overlaid on the 95% confidence interval plots of the experimental fatigue data and a good qualitative agreement was observed.

5. INFLUENCE OF MICROSTRUCTURAL ATTRIBUTES AND LOCAL MICROSTRUTURAL RESPONSE ON FATIGE LIFE

5.1 Role of Microstructural Attributes in Limiting Fatigue Life

With the advent of advanced electron microscopy techniques, the important role played by various microstructural attributes in causing fatigue failure has become quite evident. In order to improve the fatigue performance of materials, it is important to not only investigate the mechanisms that cause fatigue failure, but also the competing role played by various attributes in triggering a particular failure mechanism. It is tedious, expensive, and in some cases not possible to make such correlations or weigh the influence of various microstructural attributes using experiments. Rigorously validated predictive models can be used for this purpose. The life prediction model used in the current work takes into account various microstructural attributes (like grain size, γ' volume fraction and GB energy) and hence, it can be used to quantitatively assess the combined role played by various microstructural attributes in influencing fatigue scatter.

Using the energy based failure criterion (Eq. 3.10), the fatigue model helps determine which grains (or grain clusters) are more prone to the formation PSBs, and hence fatigue crack initiation. The fatigue model probes ten different SEMs containing a total of 1500 grains. The grain-by-grain fatigue life data thus obtained is pooled together along with the size attributes of corresponding grains. From this data a contour plot

(shown in Fig. 5.1) is generated between grain size and fatigue life, with the contours encompassing various number of data points. It can be inferred from Fig. 5.1 that fatigue model shows an inverse correlation between fatigue life and grain size, which is in agreement with experimental observations [61-68].

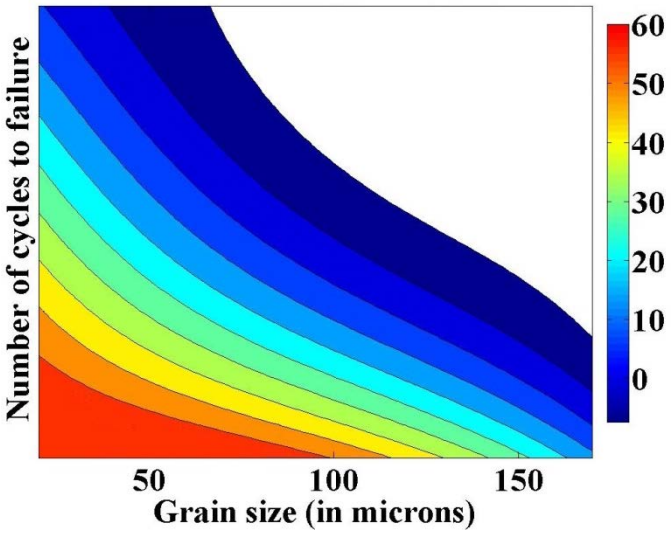

Figure 5.1. Influence of grain size on fatigue life. The colored contour region represents that it encompasses certain number of data points which can be inferred from the color bar.

The ordered γ' precipitates present in RR1000 provide a strengthening mechanism and stability at elevated temperatures. The size, distribution and volume fraction of γ' precipitates control mechanical properties [160-163], especially the yield stress at macroscopic scale or the CRSS at the slip system level [164]. It is noteworthy that an increase in volume fraction through increase in particle diameter could actually reduce the strength of the material after the γ' precipitates attain a critical size [163, 164], as Orowan looping process dominates the precipitate shearing mechanism (by paired

dislocations). Collins et al. [163] showed that for a target precipitate size range, the volume fraction of γ' precipitates can be optimized to attain an optimal CRSS. The fatigue model used in the current study only considers precipitate shearing as an active deformation mechanism, thereby assuming that a target precipitate size distribution is present in the material, at the temperature of interest during which the Orowan looping process in not dominant.

To understand the effect of γ' volume fraction on fatigue life, a single SEM was chosen and only the γ' volume fraction was changed keeping all other input parameters (like stress, strain etc.,) the same. Fatigue life was calculated for every grain cluster within the SEM chosen, for three different γ' volume fractions and a cumulative fatigue life distribution was constructed for each individual γ' volume fraction. From Fig. 5.2 it is clear that the fatigue model showed an increase in the fatigue life of the material with an increase in γ' volume fraction, which can be attributed to the strengthening mechanism imparted by the γ' phase. It must be noted that, in this case study, none of the crystal plasticity parameters (for instance, CRSS) were modified in order to take into account the change in γ' volume fraction.

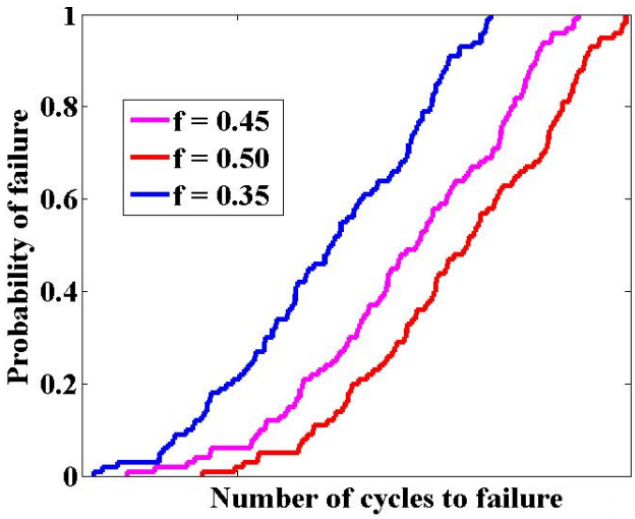

Figure 5.2. Variation in fatigue life due to variation in γ' volume fraction.

In addition to grain size and γ' volume fraction, the GB character also has a significant influence on fatigue life. Low energy stable GBs were observed to be more resistant to fatigue cracking compared to thermodynamically less stable high energy GBs [23,165,166]. Li et al. [167] observed that high energy GBs with large number of residual dislocations trapped in the GB, were more prone to fatigue cracking. Low energy GBs (such as TBs) provide strong barrier to dislocation transmission, hence accumulate less number of residual dislocations compared to other high energy GBs. Hence, the number of dislocations penetrating a GB, n_{ext-GB}^{dis}, (Eq. 3.19) has an inverse dependence on the static GB energy [23].

In order to observe the dependence of fatigue life on the GB energy, a single grain cluster (of size 8.38μm) was chosen with in an SEM, and the GB energy was varied from a lower limit of 60 mJ/m^2 (corresponding to a CSL ∑3 GB, which is a stable GB) to an upper limit of 932 mJ/m^2 (corresponding to CSL ∑9 GB, which is an unstable GB), keeping all the other parameters constant. It can be clearly observed from Fig. 5.3 that a

GB with higher energy (and hence an unstable GB) promotes quicker failure. The variation of fatigue life with GB energy was also plotted for a larger cluster (with size 19.4μm) and it was observed that for the same GB character, crack initiation is favored in the larger grain cluster. Figure 5.3 shows how the character of the GB with which the PSB intersects coupled with the size of the grain cluster controls the number of cycles taken for fatigue cracks to initiate.

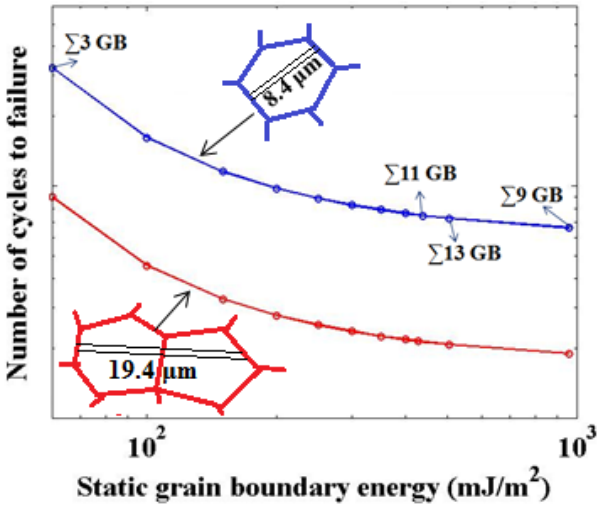

Figure 5.3. Influence of grain boundary energy on fatigue life.

5.2 Influence of Local Microstructural Response in Limiting Fatigue Life

Accumulation of irreversible slip during fatigue causes topological changes within the bulk (or at the surface) which in turn lead to stress concentrations which trigger crack initiation. During the process of dislocation transmission across a GB, based on the type of dislocation and the GB character, residual dislocations get trapped within the GB to form extrusions [117]. With repetitive cyclic loading, the residual dislocations increase in number and the extrusions grow in size [52]. This is schematically shown in

Fig. 5.4a for a selected grain in an SEM. The life prediction model used in the current study considers the formation and evolution of extrusions at the PSB-GB intersection (using Eq. 3.19). Fatigue lives and extrusion heights (at failure) were extracted for around 1500 grains in 10 different SEMs. From this data a contour plot (shown in Fig. 5.4b) is generated between extrusion height (at PSB-GB intersection) and fatigue life, with the contours encompassing various number of data points. It can be inferred from Fig. 5.4b that the fatigue life is inversely proportional to the height of extrusions (a type of cyclic slip irreversibility), which is also in agreement with the observations in the literature [57].

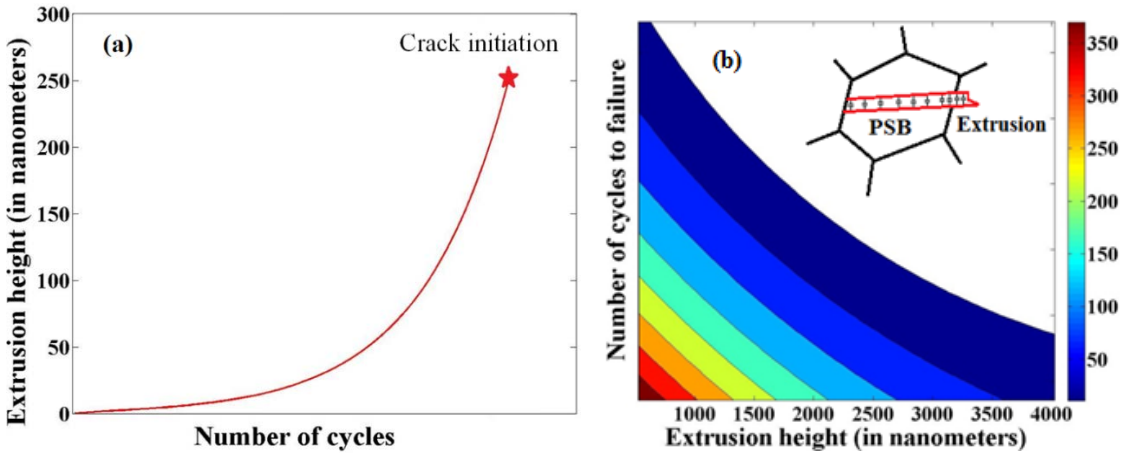

Figure 5.4. (a) Evolution of extrusion height with number of cycles, until crack initiation in a specific grain. (b) Influence of extrusion height on fatigue life. The colored contour region represents that it encompasses certain number of data points which can be inferred from the color bar.

Complex heterogeneities in the microstructure of polycrystalline materials are responsible for the highly heterogeneous stress and strain states developed within the bulk of material, and hence govern where cracks can potentially nucleate. As discussed in

Section 3.5, the elastic stress anisotropy (Λ_{eq}) and plastic strain accumulation (p) play a significant role in initiating fatigue cracks and thereby limiting the fatigue life of the material. It can be observed from Fig. 3.13a, d and g. that elastic stress anisotropy attains higher values at the GBs and is very close to zero with in the grain away from the GBs. This is due to an idealization assumed by assigning the same orientation to all the material points within the grain. The plastic strain accumulation (Fig. 3.13b, e and h) on the other hand, shows smooth variations throughout grains and attains higher values in the vicinity of GBs.

5.3 Discussion

Fatigue crack initiation in polycrystalline materials is a complex phenomenon driven by the complex interaction between local microstructural features and the defect level deformation mechanisms. Various factors acting in concert have been observed to play a major role in initiating fatigue cracks. In polycrystalline ferritic steel, the microstructure related quantities like the accumulated slip, slip rate, statistically stored and geometrically necessary dislocation density, when considered individually did not correlate well with the experimentally observed cycles to crack initiation [169]. But the rate of stored energy density (which is formulated by taking into account all the aforementioned parameters) correlated well with the number of cycles to crack initiation [169]. In polycrystalline nickel-base superalloys, accumulated slip was observed to correlate well with the location of crack initiation [88,170] and fatigue life [170,171]. Sangid et al. [23] showed that the grain size, Schmid factor and GB character played a significant role not only in triggering fatigue crack initiation, but also in influencing the

fatigue life of a nickel-base superalloy, U720. These observations and correlations clearly imply that multiple factors acting simultaneously lead to formation of fatigue cracks in polycrystalline materials.

In a nickel-base superalloy, RR1000, (which is the material of interest in the current study) fatigue cracks initiated due to formation of PSBs. The PSB model (discussed in Section 3.3) is used to assess the role played by various attributes in triggering fatigue crack initiation and hence, in influencing fatigue life of the material. Various factors like grain size, γ' volume fraction, GB energy, extrusion height, PSA and ESA were considered and their influence on fatigue life was evaluated. The model showed that all parameters except for γ' volume fraction correlated inversely with fatigue life, which is clearly in agreement with experimental observations [63-78,88,165-167,170,171]. This serves as a sanity check for the PSB model used in the current study. All the correlations that exist between these parameters and fatigue life are represented using a chord diagram (shown in Fig. 5.5). A chord connecting two parameters shows that a correlation (direct or inverse) exists between them, and the thickness of the chord shows the degree of correlation.

It is noteworthy to point out that the fatigue model clearly implies that a PSB formed in a large grain, intersecting an unstable GB and forming large extrusions, due to plastic high strain accumulation coupled with a high lattice incompatibility fails quickly compared to a less severe scenario. A wide spectrum of scenarios with varying degree of severity are possible with in bulk of the material due to the complex heterogeneous microstructure of the material and the stochastic nature of the defects interacting various

microstructural features, which in turn results in the scatter observed in the fatigue life of the material.

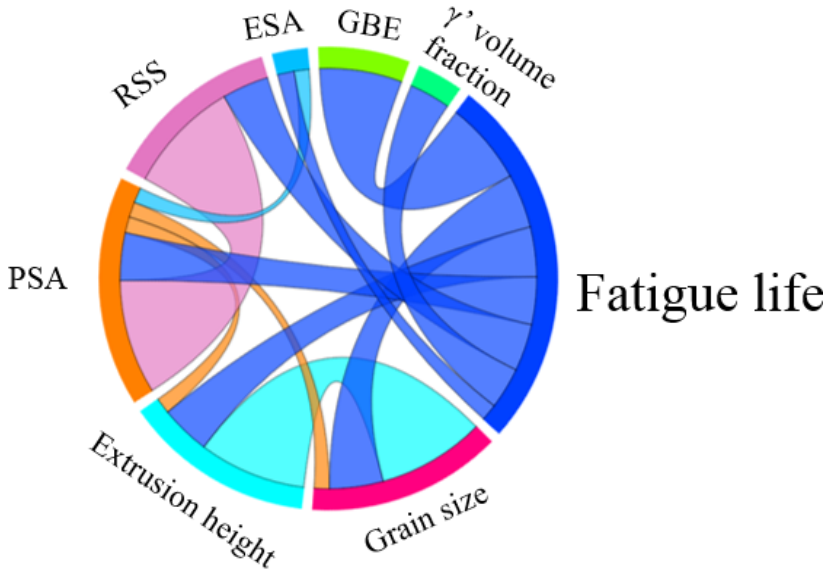

Figure 5.5. Chord diagram showing the influence of various microstructural attributes and local response on the fatigue life. GBE represents grain boundary energy, ESA represents elastic stress anisotropy, PSA represents plastic strain accumulation, RSS represents resolved shear stress. Chord diagram was created using D3 [172].

5.4 Summary

A microstructure based fatigue life prediction model is used to assess the role played by various microstructural attributes in initiating fatigue cracks and hence in influencing fatigue life of a polycrystalline nickel-base superalloy, RR1000. The fatigue model predicted correct trends in how various parameters (like the grain size, γ' volume fraction, GB character, extrusion height at PSB-GB intersection, plastic strain accumulation and elastic stress anisotropy at the GBs) influence the fatigue life of the material. Implications can be drawn from the current study that the scatter observed in

fatigue life can be attributed to the wide spectrum of complex interactions between heterogeneous microstructural attributes (grain size, GB character, γ' volume fraction) and stochastic defect level mechanisms (extrusions formed at PSB-GB intersection) in the presence of heterogeneous stress-strain state within the microstructure.

6. CONCLUSIONS AND FUTURE WORK

6.1 Conclusions

In chapter 3, we provide a detailed overview of our microstructure based fatigue life prediction framework. In summary, the framework comprises of three important modules.

i) First module simulates the variability in microstructure by generating 3D statistically equivalent microstructures (SEMs) that replicate the statistics of microstructural attributes (grain size, misorientation distribution, grain boundary character distribution) in a nickel-base superalloy, RR1000. In the current study, special emphasis is laid on studying why fatigue cracks tend to initiate at twin boundaries (TBs), and hence, twins are explicitly inserted into the SEMs generated.

ii) Second module is a rate dependent crystal plasticity finite element (CPFE) framework which is used to solve for heterogeneous stress and strain state with in the SEMs (generated in the first module), which are subjected to a one-cycle loading. State dependent variables (SDVs) (like resolved shear stress, back stress, accumulated shear strain, normal stress on slip system) are extracted for each grain, which are then used in the energy definition of a persistent slip band (PSB).

iii) Third module is the PSB energy based life prediction model. This PSB model assumes that a PSB exists in all the grains (along the slip system with maximum resolved shear stress), and calculates the cyclic evolution of the energy of the PSB. Apart from the SDVs output from CPFE, the energy definition of a PSB takes into account, GB energy barriers for dislocation transmission, accumulated strain on a slip system, slip system length on which PSB is assumed to form, anti-phase boundary energy and stacking fault energies (which are dependent on the normal strain acting on the PSB). The PSB model detects any existing low angle grain boundaries (LAGBs) with in the SEM, and assumes that the PSBs traverse through them, unhindered. Crack initiation occurs when the PSB becomes unstable. The model probes through all grains (or grain clusters joined by LAGBs) within all SEMs, and calculates fatigue life on a grain-by-grain basis. The fatigue life data obtained from multiple SEMs (for over thousands of grains) can be pooled together to generate fatigue life distributions, and this is the way the life prediction framework links variability in microstructure to scatter in fatigue life.

The fatigue framework predicts crack initiation to occur at a TB embedded in a large grain, which is in agreement with experimental evidence. A high concentration of elastic stress anisotropy and accumulated plastic strain was observed in the vicinity of the TBs where cracks were predicted to initiate. Further, normal stress was observed to dominate the maximum absolute resolved shear stress (within a PSB which happen to form inside a twin within a large grain), which suggests a significant role played by the normal stress in *unzipping* a PSB at the intersection of the TB to act as a mode I crack.

These observations from complex 3D stress states solved by crystal plasticity framework provides valuable insights on various factors that act in concert to favor fatigue crack initiation at TBs. In addition to the aforementioned insights, we have demonstrated that the fatigue framework was able to link the variability in microstructure to the scatter in fatigue life, which is one of the major contributions of the current research work.

Chapter 4 provides a detailed overview of the efforts that went into validating the PSB model. All uncertainties were identified within the model based on the ease of measurement. All uncertain parameters were assigned probability distribution functions based on the information available at hand (from literature or expert opinion). Global sensitivity analysis (GSA) was used to identify the set of most influential parameters, based on variance based sensitivity indices and global sensitivity plots. GB energy barrier for dislocation transmission, dislocation density, PSB width, an empirical parameter which is proportional to extrusion height at PSB-GB intersection were identified as the set of most influential parameters. It is important to note that all the aforementioned parameters relate to fatigue specific damage accumulation within the microstructure, and hence they play an influential role in fatigue crack initiation and hence fatigue life. Following GSA, Bayesian inference technique was used to quantify the uncertainties in the set of aforementioned parameters. Posterior distributions of the parameters were constructed using Markov chain Monte Carlo (MCMC) algorithm, which takes into account, the experimental fatigue life data and prior distributions of the parameters. Following uncertainty quantification, Monte Carlo simulations were used to propagate the uncertainties through the model, in order to obtain fatigue life predictions using multiple SEMs. The life predictions obtained using five different SEMs were compared

to the 95% confidence interval constructed using the experimental at hand, and an excellent agreement was observed between model predictions and experimental data, which served as a validation to the life prediction model.

In chapter 5, emphasis is laid on the influence of the microstructural attributes and local microstructural response on fatigue scatter observed in polycrystalline materials. The fatigue model predicted correct trends in how various parameters (like the grain size, γ' volume fraction, GB character, extrusion height at PSB-GB intersection, plastic strain accumulation and elastic stress anisotropy at the GBs) influence the fatigue life of the material, which also serves as a partial validation apart from fatigue life predictions. The PSB model clearly implies that a PSB formed in a large grain, intersecting an unstable GB and forming large extrusions, due to plastic high strain accumulation coupled with a high lattice incompatibility fails quickly compared to a less severe scenario. A wide spectrum of scenarios with varying degree of severity are possible with in bulk of the material due to the complex heterogeneous microstructure of the material and the stochastic nature of the defects interacting various microstructural features, which in turn results in the scatter observed in the fatigue life of the material. Implications can be drawn from the current study that the scatter observed in fatigue life can be attributed to the wide spectrum of complex interactions between heterogeneous microstructural attributes (grain size, GB character, γ' volume fraction) and stochastic defect level mechanisms (extrusions formed at PSB-GB intersection) in the presence of heterogeneous stress-strain state within the microstructure.

6.2 Future Work

The microstructure based life prediction framework developed in the current study is highly modularized. The robustness and hence the predictive capabilities of the framework can be enhanced by improving individual modules. This can be achieved by a combination of both experiments and physics based computational analyses. We propose the following as future work that can be done in order to enhance the robustness and the applicability regime of the framework.

1. Generating SEMs based on the statistics of microstructural attributes obtained from 2D EBSD scans leads to aleatory (or irreducible) uncertainties. Specifically, aleatory uncertainties arise from assumptions in obtaining grain size distributions, nearest neighbor distributions, grain shape distributions. Such uncertainties can be reduced to a considerable extent by extracting the 3D microstructure of the material either by using serial sectioning or high energy X-Ray diffraction techniques.
2. In the current workflow of generating SEMs, statistical equivalence of grain boundary character distribution was verified solely based on the percentage of TBs with respect to all CSL GBs present within the microstructure. This is more or less, a first order verification methodology, and a more exhaustive verification approach can be taken by considering various verification metrics like density of twins within a given volume of microstructure, length and thickness of the twins, percentage of coherent (and incoherent) twins among all TBs within the microstructure, and correlation between number of twins in

a parent grain and the size of a parent grain. Incorporating such a rigorous verification methodology will help produce SEMs with higher order accuracy with respect to capturing TBs.

3. The fitting parameters in flow and hardening rules in the rate dependent CPFE framework used in the current work are tuned to obtain a best fit macroscopic stress-strain response to closely match the experimental stress-strain curve. It is well known that several non-unique sets of parameters can reproduce a similar fit for the macroscopic response. This is not quite an accurate way to obtain the CPFE parameters. It is much more robust to obtain the parameters that can match the strains calculated (by CPFE simulations) on a microstructural region to that obtained from digital image correlation technique.
4. Incorporating residual stresses as initial stress state within the microstructure, using the CPFE framework to deterministically study the effect of complex residual stresses on fatigue scatter.
5. An inherent epistemic uncertainty exists in the PSB model due to the fact that the model does not account for the number of cycles required for PSBs to appear. This uncertainty can be reduced by experimentally quantifying the number of cycles required to form PSBs, for various strain amplitudes.
6. Experimental measurements of the height of extrusions formed at the PSB-GB intersections along with the PSB widths will help in reducing a few epistemic uncertainties in the model.

7. Using MD simulations, quantify the effect of GB normal stress on the energy barrier for dislocation transmission through the GB. This relation can be used to enhance the definition of the energy of a PSB.
8. Extend the applicability of the model to over a temperature regime. This can be done by adapting a CPFE framework which uses temperature dependent flow and hardening laws. Dependence of anti-phase boundary, stacking fault energies and GB energetics on the temperature can be calculated using MD simulations.
9. Apply the fatigue framework to a 3D microstructural volume (obtained using high energy X-Ray diffraction techniques) in which the locations of crack initiation sites are known. This helps in further validating the fatigue framework by comparing the hot-spots it predicts to the actual crack initiation sites within the microstructure.
10. At extreme temperatures fatigue cracks initiate due to inclusions. Inclusions can be explicitly incorporated into the CPFE framework through DREAM.3D. The energy based failure criterion can be modified for inclusion based fatigue cracking, and hence the whole framework can be extended to deterministically calculate the fatigue life due to inclusion cracking.

APPENDIX

APPENDIX

(Flowchart showing integration of CPFE with fatigue model)

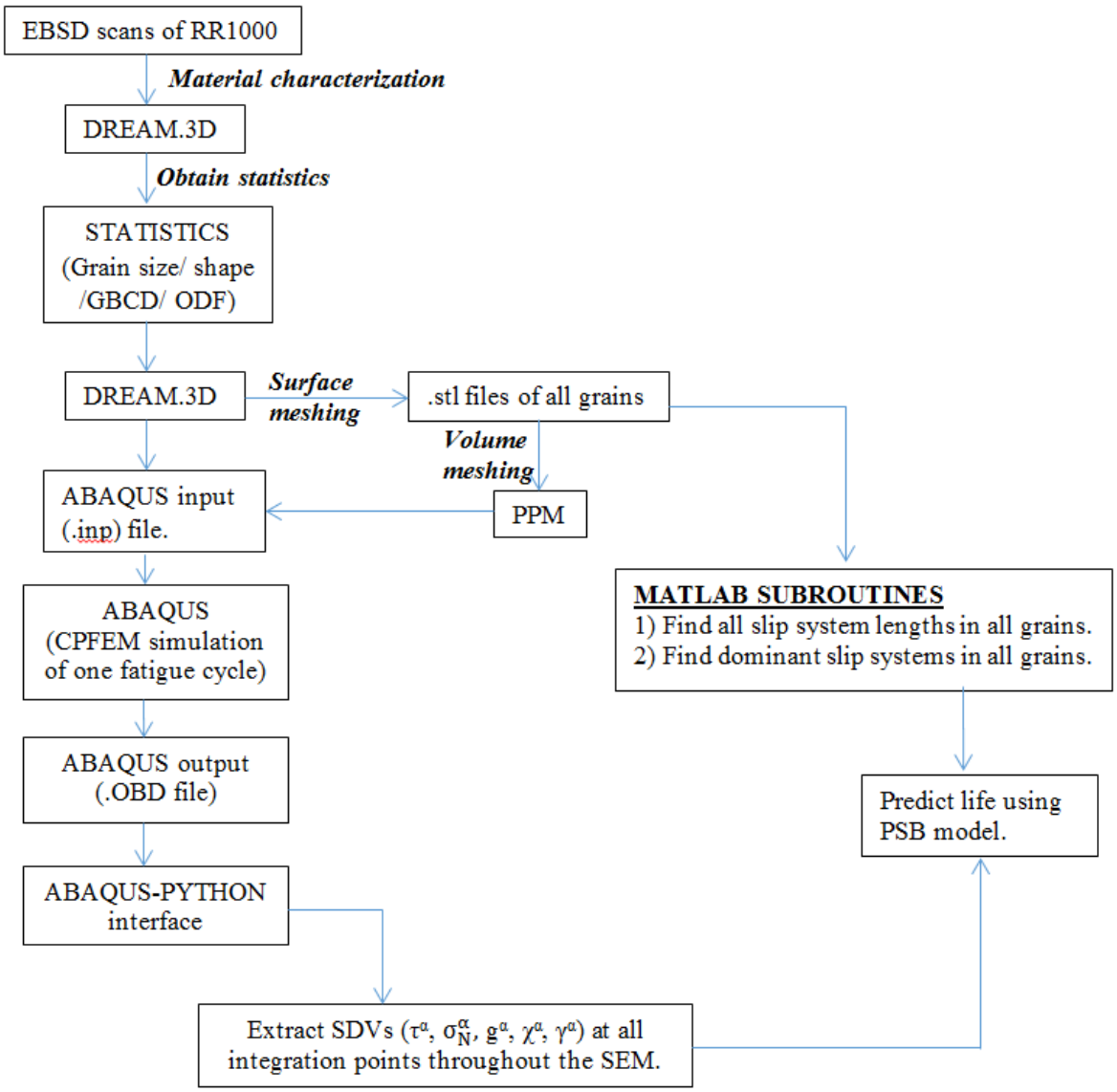

BIBLIOGRAPHY

BIBLIOGRAPHY

[1] S.J. Findlay, N.D. Harrison, Why Aircraft Fail, Materials Today, Nov. 2002.

[2] G. Redmond, From 'safe life' to fracture mechanics - F111 aircraft cold temperature proof testing at RAAF Amberley, in: Proceedings of the 10th Asia-Pacific Conference on Non-Destructive Testing, 17-21 September 2001, Brisbane, Australia.

[3] R.G. Eastin, A Critical Review of Strategies Used to Deal with Metal Fatigue, ICAF 22, 2003 - Fatigue of Aeronautical Structures as an Engineering Challenge, Proceedings of the 22nd Symposium of the International Committee on Aeronautical Fatigue, Lucern, Switzerland, 5-9 May 2003.

[4] A.F. Grandt Jr., Fundamentals of Structural Integrity – Damage Tolerant Design and Nondestructive Evaluation, John Wiley & Sons, 2004.

[5] L.F. Coffin, A study of the effects of cyclic thermal stresses on a ductile metal. Trans. Am. Soc. Mech. Eng., 76 (1954) 931-950.

[6] S.S. Manson, Behavior of materials under conditions of thermal stress. National Advisory Commission on Aeronautics: Report 1170. (1954) Cleveland: Lewis Flight Propulsion Laboratory.

[7] K.N. Smith, P. Watson, T.H. Topper, A stress-strain function for the fatigue of metals, J. Mater., 5 (1970) 767-778.

[8] Safety Recommendation A-06-060, National Transportation Safety Board, August 2006.

[9] Air safety investigation report 200205780, Australian Transport Safety Bureau, September 2004.

[10] Rolls-Royce plc Internal Report, Thomas Jackson, Fractography of Coarse Grain RR1000, 2015.

[11] O.M.D.M Messé, J. Lachambre, A. King, J.Y. Buffière, C.M.F. Rae, Investigation of fatigue crack propagation in nickel superalloy using diffraction contrast tomography and phase contrast tomography, Adv. Mater. Res. 891-892 (2014) 923-928.

[12] M.J. Caton, S.K. Jha, A.H. Rosenberger, J.M. Larson, In :K.A. Greeen, H. Harada, T.E. Howson, T.M. Pollock, R.C. Reed, J.J. Schirra, S. Walston S (Eds.). Superalloy 2004, Warrendale: The Minerals, Metals & Materials Society; 2004.

[13] K. Kobayashi, K. Yamaguchi, M. Hayakawa, M. Kimura, Grain size effect on high-temperature fatigue properties of alloy718. Materials Letters 2005; 59 (2-3): 383-386.

[14] A. Shyam, C.J. Torbet, S.K. Jha, J.M. Larsen, M.J. Caton, C.J. Szczepanski, T.M. Pollock, J.W. Jones. In: K.A. Greeen, H. Harada, T.E. Howson, T.M. Pollock, R.C. Reed, J.J. Schirra, S. Walston (Eds.). Superalloy 2004, Warrendale: The Minerals, Metals & Materials Society; 2004.

[15] M.L. Brogdon, A.H. Rosenberger, Evaluation of the influence of grain structure of the fatigue variability of Waspaloy, Superalloys 2008, Warrendale: The Minerals, Metals & Materials Society; 2008.

[16] U. Lienert, J. Almer, B. Jakobsen, W. Pantleon, H.F. Poulsen, D. Hennessy, C. Xiao, and R.M. Suter, 3-Dimensional Characterization of Polycrystalline Bulk Materials Using High-Energy Synchrotron Radiation, Materials Science Forum 539-543 (2007) 2353-2358.

[17] M.D. Uchic, M.A. Groeber, D.M. Dimiduk, J.P. Simmons, Scripta Mater. 55 (2006) 23–28.

[18] M.A. Groeber, M.A. Jackson**,** July 2015. <http://dream3d.bluequartz.net/>

[19] M.A. Groeber, M.A. Jackson**,** DREAM.3D: A Digital Representation Environment for the Analysis of Microstructure in 3D, Integr. Mater. Manuf. Innov. 3 (2014) 1-17.

[20] W.E. Lorensen, H.E. Cline, Marching cubes: A high resolution 3D surface construction algorithm. ACM Computer Graphics 21 (1987) 163–169.

[21] A. Cerrone, <http://www.cfg.cornell.edu/~arc247/PPM/Documentation.html>.

[22] K. Tanaka, T. Mura, A dislocation model for fatigue crack initiation, J. Appl. Mech. 48 (1981) 97-103.

[23] M.D. Sangid, H.J. Maier, H. Sehitoglu, A physically based fatigue model for prediction of crack initiation from persistent slip bands in polycrystals, Acta Mater. 59 (2011) 328-341.

[24] M.D. Sangid, H.J. Maier, H. Sehitoglu, The role of grain boundaries on fatigue crack initiation – an energy approach, Int. J. Plast.27 (2011) 801-821.

[25] S.R. Yeratapally, M.G. Glavicic, M. Hardy, M.D. Sangid, Microstructure based fatigue life prediction framework for polycrystalline nickel-base superalloys with emphasis on the role played by twin boundaries in crack initiation. Acta Mat. 2015. In review.

[26] A. Saltelli, M. Ratto, T. Andres, F. Campolongo, J. Cariboni, D. Gatelli, Global sensitivity analysis: the primer. Wiley Interscience; 2008.

[27] R.C. Smith, Uncertainty quantification: Theory, Implementation, and Applications. SIAM Computational Science & Engineering Series: Philadelphia, PA, USA, 2014.

[28] M.C. Kennedy, A. O'Hagan, Bayesian calibration of computer models, Journal of the Royal Statistical Society: Series B, 63 (2011) 425-464.

[29] P.E. Hadjidoukas, P. Angelikopoulos, D. Rossinelli, D. Alexeev, C. Papadimitriou, P. Koumoutsakos, Bayesian uncertainty quantification and propagation for discrete element simulations of granular materials. Comput. Methods Appl. Mech. Engrg. 282 (2014) 218–238.

[30] J.A. Ewing, J.C.W. Humfrey, The fracture of metals under repeated alternations of stress, Phil. Trans. R. Soc., 200 (1903) 241–250.

[31] C.E. Feltner, C. Laird, Cyclic stress-strain response of f.c.c metals and alloys-II. Dislocation structures and mechanisms, Acta Metall. 15 (1967) 1633-1653.

[32] D. Kuhlmann-Wilsdorf, Theory of plastic deformation: properties of low energy dislocation structures, Mater. Sci. Eng. A 113 (1989) 1-41.

[33] P. Neumann, Low energy dislocation configurations: a possible key to the understanding of fatigue, Mater. Sci. Eng. 81 (1986) 465-475.

[34] H. Mughrabi, F. Ackermann, K. Herz, Persistent slip bands in fatigued face-centered and body-centered cubic metals. Am. Soc. Test Mater., (1979) 69-105.

[35] U. Essmann, U. Gösele, H. Mughrabi, A model of extrusions and intrusions in fatigued metals. I. Point-defect production and the growth of extrusions, Philos. Mag. A 44 (1981) 405-426.

[36] K. Differt, U. Esmann, H. Mughrabi, A model of extrusions and intrusions in fatigued metals. II. Surface roughening by random irreversible slip, Philos. Mag. A 54 (1986) 237-258.

[37] H.J. Christ, H. Mughrabi, Cyclic stress-strain response and microstructure under variable amplitude loading, Fatigue Fracr. Engng Mater. Struct. 19 (1996) 335-348.

[38] J. Man, M. Petrenec, K. Orbitlik, J. Polak, AFM and TEM study of cyclic slip localization in fatigued ferritic X10CrAl24 stainless steel Acta Materialia 52 (2004) 5551–5561.

[39] R.E. Stoltz, A.G. Pineau, Dislocation-precipitate interaction and cyclic stress-strain behavior of a γ' strengthened superalloy, Mater. Sci. Eng. 34 (1978) 275-284.

[40] H.S. Ho, M. Risbet, X. Feaugas, On the unified view of the contribution of plastic strain to cyclic crack initiation: Impact of the progressive transformation of shear bands to persistent slip bands, Acta Mater. 85 (2015) 155–167.

[41] H.J. Christ, H. Mughrabi, Cyclic stress-strain response and microstructure under variable amplitude loading, Fatigue Fracr. Engng Mater. Struct. 19 (1996) 335-348.

[42] P. Lukas, L. Kunz, Cyclic slip localisation and fatigue crack initiation in fcc single crystals, Mat. Sci. Eng. A 314 (2001), 75–80.

[43] P. Lukas, L. Kunz, Role of persistent slip bands in fatigue, Phil. Mag. 21 (2004) 317-330.

[44] M. Petrenec, K. Orbitlik, J. Polak, J. Man, Dislocation structures in nickel based superalloy Inconel 792-5A fatigued at room temperature and 700C, Mat. Sci. Forum 567-568 (2008) 429-432.

[45] H. Mughrabi, Cyclic slip irreversibilities and the evolution of fatigue damage, Metal. Mater. Trans. A 40 (2009) 1257-1279.

[46] Z.S. Basinski, S.J. Basinski, Fundamental aspects of low amplitude cyclic deformation in face-centred cubic crystals, Prog. Mater. Sci. 36 (1992) 89-148.

[47] M.D. Sangid, The physics of fatigue crack initiation, Int. J. Fatigue 57 (2013) 58-72.

[48] S.D. Antolovich, R.W. Armstrong, Plastic strain localization in metals: origins and consequences, Prog. Mater. Sci. 59 (2014) 1-160.

[49] A. Weidner., R. Beyer R., Blochwitz C., Holste C., Schwab A. and Tirschler W. Slip activity of persistent slip bands in polycrystalline nickel. Mater. Sci. Eng. A, 435–436, (2006) 540-546.

[50] M. Risbet, X. Feaugas, C. Guillemer-Neel, M. Clavel, Use of atomic force microscopy to quantify slip irreversibility in a nickel-base superalloy. Scripta Mater., 49 (2003) 533-538.

[51] R.C. Boettner, A.J. McEvily, Y.C. Liu, On formation of fatigue cracks at twin boundaries, Philos. Mag. 10 (1964) 95-106.

[52] H. Mughrabi, R. Wang, K. Differt, U. Essmann, Fatigue crack initiation by cyclic slip irreversibilities in high-cycle fatigue. Am. Soc. Test Mater., (1983) 5-45.

[53] Z.F. Zhang, Z.G. Wang, Dependence of intergranular fatigue cracking on the interactions of persistent slip bands with grain boundaries, Acta Mater. 51 (2003) 347-364.

[54] W. Abuzaid, H. Sehitoglu, J. Lambros, Plastic strain localization and fatigue micro-crack formation in Hastelloy X, Mater. Sci. Eng. A 561 (2013) 507–519.

[55] K. Differt, U. Essmann, H. Mughrabi, A model of extrusions and intrusions in fatigued metals. Part II: Surface roughening by random irreversible slip. Phil. Mag. A, 54 (1986) 237-258.

[56] H. Mughrabi, Fatigue, an everlasting materials problem - still en vogue. Procedia Eng., 2 (2010) 3–26.

[57] H. Mughrabi, Cyclic slip irreversibility and fatigue life: A microstructure-based analysis. Acta Mater., 61 (2013) 1197-1203.

[58] H. Mughrabi, On the life-controlling microstructural fatigue mechanisms in ductile metals and alloys in the gigacycle regime, Fatigue Fracr. Engng Mater. Struct. 22 (1999) 633-41.

[59] M. Risbet, X. Feaugas, Some comments about fatigue crack initiation in relation to cyclic slip irreversibility. Eng. Fract. Mech., 75 (2008) 3511–19.

[60] J. Man, K. Obrtlík, C. Blochwitz, J. Polák, Atomic force microscopy of surface relief in individual grains of fatigued 316L austenitic stainless steel. Acta Mater., 50 (2002) 3767-80.

[61] A.W. Thompson, W.A. Backofen, The effect of grain size on fatigue. Acta Metall., 19 (1971) 597-606.

[62] P. Lukas, L. Kunz, Effect of grain size on the high cycle fatigue behaviour of polycrystalline copper. Mater. Sci. Eng., 85 (1987) 67-75.

[63] F. Alexandre, S. Deyber, A. Pineau, Modelling the optimum grain size on the low cycle fatigue life of a Ni based superalloy in the presence of two possible crack initiation sites. Scripta Mater., 50 (2004) 25–30.

[64] B. Pieraggi, J.F. Uginet, Fatigue and creep properties in relation with alloy 718 microstructure. Superalloys 718,625,706 and various derivatives, (1994) 535-544.

[65] N. Spath, V. Zerrouki, P. Poubanne, J.Y. Guedou, 718 superalloy forging simulation: A way to improve process and material potentials. Superalloys 718,625,706 and various derivatives, (2001) 173-183.

[66] K.O. Findley, A. Saxena, Low cycle fatigue in Rene 88DT at 650 ◦C: crack nucleation mechanisms and modeling. Metall. Mater. Trans. A, 37 (2006) 1469–75.

[67] M.D. Sangid, H.J. Maier, H. Sehitoglu, The role of grain boundaries on fatigue crack initiation – an energy approach. Int. J. Plast., 27 (2011) 801-821.

[68] D.L. Davidson, R.G. Tryon, M. Oja, R. Matthews, K.S.R. Chandran, Fatigue crack initiation in Waspaloy at 20 °C. Metall. Mater. Trans. A, 38 (2007) 2214-25.

[69] M.D. Sangid, H.J. Maier, H. Sehitoglu, An energy-based microstructure model to account for fatigue scatter in polycrystals. J. Mech. Phys. Solids, 59 (2011) 595-609.

[70] M. Oja, K.S. Ravi Chandran, R.G. Tryon, Orientation Imaging Microscopy of fatigue crack formation in Waspaloy: Crystallographic conditions for crack nucleation. Int. J. Fatigue, 32 (2010) 551–556.

[71] A. Weidner, R. Beyer, C. Blochwitz, C. Holste, A. Schwab, W. Tirschler, Slip activity of persistent slip bands in polycrystalline nickel. Mater. Sci. Eng. A, 435–436 (2006) 540-546.

[72] C. Buque, J. Bretschneider, A. Schwab, C. Holste, Effect of grain size and deformation temperature on the dislocation structure in cyclically deformed polycrystalline nickel. Mater. Sci. Eng. A, 319–321 (2001) 631-636.

[73] R. Keller, W. Zielinski, W.W. Gerberich, On the onset of low-energy dislocation substructures in fatigue: Grain size effects. Mater. Sci. Eng. A, 113 (1989) 267-280.

[74] J. Miao, T.M. Pollock, W.J. Jones, Crystallographic fatigue crack initiation in nickel-based superalloy Rene 88DT at elevated temperature. Acta Mater., 57 (2009) 5964-74.

[75] J. Miao, T.M. Pollock, W.J. Jones, Microstructural extremes and the transition from fatigue crack initiation to small crack growth in a polycrystalline nickel-base superalloy, Acta Mater. 60 (2012) 2840–2854.

[76] A. Shyam, C.J. Torbet, S.K. Jha, J.M. Larsen, M.J. Caton, C.J. Szczepanski, T.M. Pollock, W.J. Jones, Development of ultrasonic fatigue for rapid, high temperature fatigue studies in turbine engine materials. Superalloys, Minerals, Metals and Materials Society, (2004) 259–268.

[77] J.C. Healy, L. Grabowski, C.J. Beevers, Monitoring fatigue of a nickel-base superalloy at positive and negative stress ratios using an optical system. Fatigue & Fracture of Engrg. Mater. Struct. 15 (1991) 309-321.

[78] J.C. Healy, L. Grabowski, C.J. Beevers, Short-fatigue-crack growth in a nickel-based superalloy at room and elevated temperature. Int. J. Fatigue 13 (1991) 133-138.

[79] A.W. Thompson, The influence of grain and twin boundaries in fatigue cracking, Acta Metall. 20 (1972) 1085-1094.

[80] Z.J. Zhang, P. Zhang, L.L. Li, Z.F. Zhang, Fatigue cracking at twin boundaries: Effects of crystallographic orientation and stacking fault energy, Acta Mater. 60 (2012) 3113-3127.

[81] A. Heinz, P. Neumann, Crack initiation during high cycle fatigue of an austenitic steel, Acta Metall. Mater. 38 (1990) 1933-1940.

[82] C.A. Stein, A. Cerrone, T. Ozturk, S. Lee, P. Kenesei, H. Tucker, R. Pokharel, J. Lind, C. Hefferan, R.M. Suter, A.R. Ingraffea, A.D. Rollett, Fatigue crack initiation, slip localization and twin boundaries in a nickel-based superalloy, Curr. Opin. Solid State Mater. Sci. 18 (2014) 244-252.

[83] Z.R. Wang, H. Margolin, Mechanism for the formation of high cycle fatigue cracks at fcc annealing twin boundaries, Metall. Trans. A 16 (1985) 873-880.

[84] P. Peralta, L. Llanes, J. Bassani, C. Laird, Deformation from twin-boundary stresses and the role of texture: application to fatigue, Philos. Mag. A 70 (1994) 219-232.

[85] P. Neumann. Analytical solution for the incompatibility stresses at twin boundaries in cubic crystals. Proceedings of the seventh international fatigue congress, Beijing: 1999, p. 107-114.

[86] M.D. Sangid, T. Ezaz, H. Sehitoglu, I.M. Robertson, Energy of slip transmission and nucleation at grain boundaries, Acta Mater. 59 (2011) 283-296.

[87] G.M. Castelluccio, D.L. McDowell, Effect of annealing twins on crack initiation under high cycle fatigue conditions, J. Mater. Sci. 48 (2012) 2376-2387.

[88] A. Cerrone, C. Stein, R. Pokharel, C. Hefferan, J. Lind, H. Tucker, R. Suter, A. Rollett, A. Ingraffea, Implementation and verification of a microstructure-based capability for modeling microcrack nucleation in LSHR at room temperature, Modelling Simul. Mater. Sci. Eng. 23 (2015) 1-31.

[89] M.R. Lin, M.E. Fine, T. Mura, Fatigue crack initiation on slip bands: theory and experiment. Acta Metall. 1986;34:619.

[90] T. Mura, Y. Nakasone, A theory of fatigue crack initiation in solids. Transactions of the ASME. Journal of Applied Mechanics 1990;57:1.

[91] G. Venkataraman, Y.W. Chung, Y. Nakasone, T. Mura, Free energy formulation of fatigue crack initiation along persistent slip bands: calculation of S-N curves and crack depths. Acta Metall. Mater. 38 (1990) 31.

[92] S. Madireddy, B. Sista, K. Vemaganti, A Bayesian approach to selecting hyperelastic constitutive models of soft tissue Comput. Methods Appl. Mech. Engrg. 291 (2015) 102–122.

[93] S.H. Cheung, T.A. Oliver, E.E. Prudencio, S. Prudhomme, R.D. Moser, Bayesian uncertainty analysis with applications to turbulence modeling, Reliab. Eng. Syst. Saf. 96 (2011) 1137–1149.

[94] M. Koslowski, A. Strachan, Uncertainty propagation in a multiscale model of nanocrystalline plasticity. Reliab. Eng. Syst. Saf. 96, 1161 (2011).

[95] P. Angelikopoulos, C. Papadimitriou, P. Koumoutsakos, Bayesian uncertainty quantification and propagation in molecular dynamics simulations: A high performance computing framework, J. Chem. Phys., 137, 144103 (2012).

[96] R. Zhang, S. Mahadevan. Model uncertainty and Bayesian updating in reliability-based inspection. Struct. Saf., 22 (2000) 145–60.

[97] A. Makeev, Y. Nikishkov, E. Armanios, A concept for quantifying equivalent initial flaw size distributions in fracture mechanics based life prediction models. Int. J. Fatigue 29 (2007) 141–5.

[98] R. Cross, A. Makeev, E. Armanios, Simultaneous uncertainty quantification of fracture mechanics based life prediction model parameters. Int. J. Fatigue, 29 (2007) 1510–5.

[99] S. Sankararaman, Y. Ling, C. Shantz, S. Mahadevan, Uncertainty quantification in fatigue crack growth prognosis. Int. J. Prognostics Health Manage 2 (2011).

[100] M. Chiachío, J. Chiachío, G. Rus, J.J. Beck, Predicting fatigue damage in composites: a Bayesian framework. Struct. Saf. 51 (2014) 57–68.

[101] J. Chiachío, M. Chiachío, A. Saxena, S. Sankararaman, G. Rus, K. Goebel, Bayesian model selection and parameter estimation for fatigue damage progression models in composites. Int. J. Fatigue 70 (2015) 361-73.

[102] A. Rovinelli, R.A. Lebensohn, M.D. Sangid, Influence of microstructure variability on short crack behavior through postulated micromechanical short crack driving force metrics. Eng. Fract. Mech. 138 (2015) 265-88.

[103] J.H. Panchal, S.R. Kalidindi, D.L. McDowell, Key computational modeling issues in Integrated Computational Materials Engineering, Computer Aided Design 45 (2013) 4–25.

[104] R. Jiang, N. Karpasitis, N. Gao, P.A.S. Reed, Effects of microstructures on fatigue crack initiation and short crack propagation at room temperature in an advanced disc superalloy, Mater. Sci. Eng. A 641 (2015) 148–159.

[105] P. Feltham, Grain growth in metals, Acta Metall. 5 (1957) 97-105.

[106] M. Groeber. Development of an automated characterization-representation framework of polycrystalline materials in 3D (PhD thesis), Ohio State University, USA, 2007.

[107] L. Chan. Synthetic three-dimensional voxel-based microstructures that contain annealing twins (PhD thesis), Carnegie Mellon University, USA, 2010.

[108] MINITAB, October, 2015. < http://www.minitab.com/>.

[109] S. Plimpton, October 2015. Large-scale atomic/molecular massively parallel simulator (LAMMPS). <http://lammps.sandia.gov/>.

[110] O.M.D.M. Messé, S. Stekovic, M.C. Hardy, C.M.F. Rae, Characterization of Plastic Deformation Induced by Shot-Peening in a Ni-Base Superalloy, J. Mater. 66 (2014) 2502-2515.

[111] S.M. Foiles, J.J. Hoyt, Computation of grain boundary stiffness and mobility from boundary fluctuations, Acta Mater. 54 (2006) 3351-3357.

[112] Y. Mishin, Atomistic modeling of the γ and γ'-phases of the Ni–Al system, Acta Mater. 52 (2004) 1451-1467.

[113] A. Fatemi, D. F. Socie, A critical plane approach to multiaxial fatigue damage including out-of-phase loading, Fatigue Fract. Eng. Mater.Struct.11 (1988) 149-165.

[114] D.S. Xu, R.Yang, J. Li, J.P. Chang, H. Wang, D. Li, S. Yip, Atomistic simulation of the influence of pressure on dislocation nucleation in bcc Mo, Comput. Mater. Sci. 36 (2006) 60-64.

[115] M.A. Tschopp, D.L. McDowell, Influence of single crystal orientation on homogeneous dislocation nucleation under uniaxial loading, J. Mech. Phys. Solids 56 (2008) 1806-1830.

[116] Y. Sun, J.R. Rice, L. Truskinovsky, Dislocation nucleation versus cleavage in Ni_3Al and Ni., Materials Research Society; Pittsburgh: 1991, p. 243.

[117] T.C. Lee, I.M. Robertson, H.K. Birnbaum, TEM in situ deformation study of the interaction of lattice dislocations with grain boundaries in metals, Philos. Mag. A 62 (1990) 131-153.

[118] A.N. Stroh, A theory of the fracture of metals, Adv. Phys. 6 (1957) 418-465.

[119] H.J. Christ, On the orientation of cyclic-slip-induced intergranular fatigue cracks in face-centred cubic metals, Mater. Sci. Eng. A 117 (1989) L25-L29.

[120] R. Schouwenaars, M. Seefeldt, P. Van Houtte, The stress field of an array of parallel dislocation pile-ups: Implications for grain boundary hardening and excess dislocation distributions, Acta Mater. 58 (2010) 4344-4353.

[121] D.L. Olmsted, S.M. Foiles, E.A. Holm, Survey of computed grain boundary properties in face- centered cubic metals: I. Grain boundary energy, Acta Mater. 57 (2009) 3694-3703.

[122] T.A. Parthasarathy, S.I. Rao, D.M. Dimiduk,, A fast spreadsheet model for the yield strength of superalloys, Superalloys (2004) 887-896.

[123] R.J. Asaro, A. Needleman, Texture development and strain hardening in rate dependent polycrystals, Acta Metall. 23 (1984) 923-953.

[124] E.H. Lee, Elastic-plastic deformations at finite strains, J. Appl. Mech. 36 (1969) 1-6.

[125] J.P. Hirth, J. Lothe, Theory of Dislocations, second ed., Wiley, New York, 1982.

[126] J.D. Eshelby, Simple derivation of the elastic field of an edge dislocation, Br. J. Appl. Phys. 17 (1966) 1131-1135.

[127] G.I. Taylor, The mechanism of plastic deformation of crystals, Proc. Roy. Soc. 145 (1934) 362-387.

[128] H.A. Kuhn, H.G. Sockel, Contributions of the different phases of two nickel-base superalloys to the elastic behaviour in a wide temperature range, Phys. Stat. Sol. (A) 119 (1990) 93-105.

[129] M. Preuss, J.Q. Fonseca, B. Grant, E. Knoche, R. Moat, M. Daymond, The effect of γ' particle size on the deformation mechanism in an advanced polycrystalline nickel-base superalloy, Superalloys 2008.

[130] G.A. Alers, J.R. Neighbours, H. Sato, Temperature dependent magnetic contributions to the high field elastic constants of nickel and an Fe-Ni alloy, J. Phys. Chem. Solids 13 (1960) 40-55.

[131] S.V. Prikhodko, H.Yang, A.J. Ardell, J.D. Carnes, D.G. Isaak, Temperature and composition dependence of the elastic constants of Ni_3Al, Metall. Mater. Trans. A 30 (1999) 2403-2408.

[132] P.J. Armstrong, C.O. Frederick, A Mathematical representation of the multiaxial Bauschinger effect, Report RD/B/N, 731 (1966), Central Electricity Generating Board, Berkeley, UK.

[133] D.L. McDowell, S. Ghosh, S.R. Kalidindi, Representation and computational structure-property relations of random media, J. Mater. 63 (2011) 45-51.

[134] M.P. Echlin, W.C. Lenthe, T.M. Pollock, Three-dimensional sampling of material structure for property modeling and design, Integr.Mater.Manuf.Innov.3 (2014) 1-14.

[135] B. Lin, L.G. Zhao, J. Tong, H.J. Christ, Crystal plasticity modeling of cyclic deformation for a polycrystalline nickel-based superalloy at high temperature, Mater. Sci. Eng. A 527 (2010) 3581–3587.

[136] J.C. Tucker, L.H. Chan, G.S. Rohrer, M.A. Groeber, A.D. Rollett, Tail Departure of Log-Normal Grain Size Distributions in Synthetic Three-Dimensional Microstructures, Metal. Mater. Trans. A 43 (2011) 2810-2822.

[137] A. Acharya, A.J. Beaudoin, Grain-size effect in viscoplastic polycrystals at moderate strains, J. Mech. Phys. Solids 48 (2000) 2213-2230.

[138] C.A. Sweeney, W. Vorster, S.B. Leen, E. Sakurada, P.E. McHugh, F.P.E. Dunne, The role of elastic anisotropy, length scale and crystallographic slip in fatigue crack nucleation, J. Mech. Phys. Solids 61 (2013) 1224-1240.

[139] W.Z. Abuzaid, M.D. Sangid, J.D. Carroll, H. Sehitoglu, J. Lambros, Slip transfer and plastic strain accumulation across grain boundaries in Hastelloy X, J. Mech. Phy. Solids 60 (2012) 1201–1220.

[140] T. Ezaz, M.D. Sangid, H. Sehitoglu, Energy barriers associated with slip–twin interactions, Philos. Mag, 91 (10) (2011) 1464–1488.

[141] M.D. Sangid, T. Ezaz, H. Sehitoglu, Energetics of residual dislocations associated with slip-twin and slip-GBs interactions, Mat. Sci. Eng. A 542 (2012) 21-30.

[142] ASTM standard, E606/E606M-12, Standard test method for strain-controlled fatigue testing.

[143] P.D. Arendt, D.W. Apley, W. Chen, Quantification of model uncertainty: calibration, model discrepancy, and identifiability. J Mech Des 134 (2012a) 908.

[144] D.M. Collins, H.J. Stone, A modelling approach to yield strength optimisation in a nickel-base superalloy, International Journal of Plasticity 54 (2014) 96–112.

[145] H.Y. Li, J.F. Sun, M.C. Hardy, H.E. Evans, S.J. Williams, T.J.A. Doel, P. Bowen, Effects of microstructure on high temperature dwell fatigue crack growth in a coarse grain PM nickel based superalloy, Acta Mater. 90 (2015) 355–369.

[146] M.C. Hardy, B. Zirbel, G. Shen, R. Shankar, in: K.A. Green et al. (Eds.), Superalloys 2004, TMS (The Minerals, Metals & Materials Society), 2004, p. 83.

[147] E.W. Huang, R.I. Barabash, W. Yandong, Bj C, L Li, P.K. Liaw, G.E. Ice, R. Yang, C. Hahn, L.M. Pike, D.L. Klarstrom, Plastic behavior of a nickel-based alloy under monotonic tension and low-cycle-fatigue loading. Int. J. Plasticity 24 (2008) 1440.

[148] M. Huang, L. Zhao, J. Tong, Discrete dislocation dynamics modelling of mechanical deformation of nickel-based single crystal superalloys Int. J. Plasticity 28 (2012) 141–158.

[149] J. Jiang, J. Yang, T. Zhang, F.P.E. Dunne, T.B. Britton, On the mechanistic basis of fatigue crack nucleation in Ni superalloy containing inclusions using high resolution electron backscatter diffraction, Acta Mater. 97 (2015) 367–379.

[150] R. Bolado-Lavin, W. Castaings, S. Tarantola, Contribution to the sample mean plot for graphical and numerical sensitivity analysis. Reliability Engineering and System Safety 94 (2009) 1041–1049.

[151] S. Tarantola, V. Kopustinskas, R. Bolado-Lavin, A. Kaliatka, E. Uspuras, M. Vaisnoras, Sensitivity analysis using contribution to sample variance plot: Application to a water hammer model. Reliability Engineering and System Safety 99 (2012) 62–73.

[152] E. Plischke, An adaptive correlation ratio method using the cumulative sum of the reordered output, Reliability Engineering and System Safety 107 (2012) 149–156.

[153] N. Metropolis, A. Rosenbluth, M. Rosenbluth, A. Teller, E. Teller, Equation of state calculations by fast computing machines. J Chem Phys 21 (1953) 1087–92.

[154] W.K. Hastings WK. Monte Carlo sampling methods using Markov chains and their applications. Biometrika 57 (1970) 97–109.

[155] A. Gelman, J.B. Carlin, H.S. Stern, D.B. Rubin, Bayesian Data Analysis. New York: Chapman & Hall; 2004. 289–298.

[156] S.R. Niezgoda, D.M. Turner, D.T. Fullwood, S.R. Kalidindi, Optimized structure based representative volume element sets reflecting the ensemble-averaged 2-point statistics, Acta Mater. 58 (2010) 4432–4445.

[157] A. Miroshnikov, E.M. Conlon (2014) parallelMCMCcombine: An R Package for Bayesian Methods for Big Data and Analytics. PLoS ONE 9(9): e108425.

[158] W. Neiswanger, C. Wang, E.P. Xing, Asymptotically exact, embarrassingly parallel MCMC. In Proceedings of the International Conference on Uncertainty in Artificial Intelligence, 2014.

[159] H. Mughrabi, Microstructural fatigue mechanisms: Cyclic slip irreversibility, crack initiation, non-linear elastic damage analysis, Int. J. Fatigue, 57 (2013) 2-8.

[160] S. Babu, M. Miller, J. Vitek, S. David, Characterization of the microstructure evolution in a nickel base superalloy during continuous cooling conditions. Acta Mater., 49 (2001) 4149–60.

[161] P. Sarosi, B. Wang, J. Simmons, Y. Wang, M. Mills, Formation of multimodal size distributions of γ' in a nickel-base superalloy during interrupted continuous cooling. Scr. Mater., 57 (2007) 767–770.

[162] T.A. Parthasarathy, S.I. Rao, D.M. Dimiduk, A fast spreadsheet model for the yield strength of superalloys. TMS, (2004) 887–896.

[163] D.M. Collins, H.J. Stone, Modelling approach to yield strength optimisation in a nickel-base superalloy, Int. J. Plasticity, 54 (2014) 96–112.

[164] S. Schanzer, E. Nembach, The critical resolved shear stress of γ'-strengthened nickel-based superalloys with γ'-volume fractions between 0.07 and 0.47. Acta Metal. Mater., 40, (1992) 803-813.

[165] A.P. Sutton, R.W. Ballutti, On geometric criteria for low interfacial energy. Acta Metall. 35 (1987) 2177-2201.

[166] W. Liu, M. Bayerleini, H. Mughrabi, A. Day, P.N. Quested, Crystallographic features of intergranular crack initiation in fatigued copper polycrystals. Acta Metall Mater., 40 (1992) 1763-71.

[167] L.L. Li, P. Zhang, Z.J. Zhang, Z.F. Zhang, Effect of crystallographic orientation and grain boundary character on fatigue cracking behaviors of coaxial copper bicrystals. Acta Mater., 61 (2013) 425–438.

[168] S.R. Yeratapally, M.G. Glavicic, A. Christos, M.D. Sangid, Bayesian uncertainty quantification and propagation for validation of a microstructure sensitive model for prediction of fatigue crack initiation. Int. J. Fatigue. (2015) (submitted)

[169] V.V.C. Wan, D.W. MacLachlan, F.P.E. Dunne, A stored energy criterion for fatigue crack nucleation in polycrystals. Int. J. Fatigue, 68 (2014) 90-102.

[170] F.P.E. Dunne, A.J. Wilkinson, R. Allen, Experimental and computational studies of low cycle fatigue crack nucleation in a polycrystal. Int. J. Plasticity, 23 (2007) 273–295.

[171] A. Manonukul, F.P.E. Dunne, High and low-cycle fatigue crack initiation using polycrystal plasticity. Proc. R. Soc. Lond. A, 460 (2004) 1881–1903.

[172] <http://d3js.org/>, November 2015.

VITA

VITA

Saikumar Reddy Yeratapally was born in 1988 in a small village, Nellorepally, in the state of Andhra Pradesh, India. He attended primary and secondary school in Hyderabad, India. In 2005, he began his undergraduate education by majoring in mechanical engineering at the Birla institute of Technology and Science (BITS) in Goa, India. After earning his Bachelors in May 2009, he started his masters degree in mechanical engineering at Carnegie Mellon University (CMU), Pittsburgh, USA. After receiving his masters degree from CMU in December 2010, he started working towards his doctoral degree in the School of Aeronautics and Astronautics at Purdue University. During the course of his Ph.D., under the guidance of Dr. Michael D. Sangid, he worked in close collaboration with Rolls-Royce Corporation. He spent a total of nine months at NASA Langley Research Center (LaRC), as a visiting researcher. This led to a post-doc opportunity at NASA LaRC, where he hopes to conduct research in the field of fatigue failure and life assessment of polycrystalline materials.